SCUOLA DI DOTTORATO
UNIVERSITÀ DEGLI STUDI DI MILANO-BICOCCA

Dipartimento di
Scienza dei Materiali

Dottorato di Ricerca in Scienza e Nanotecnologia dei Materiali Ciclo XIX

Curriculum in Scienza dei Materiali

# Spin Properties of Germanium-based Heterostructures

Cognome De Cesari Nome Sebastiano

Matricola n° 787805

Tutore: Prof. Emanuele Grilli

Coordinatore: Prof. Gian Paolo Brivio

ANNO ACCADEMICO 2015/2016

# Contents

**Contents** **i**

**Introduction** **1**

**1 Bulk Germanium** **5**

1.1 Structural and Electronic Properties . . . . . . . . . . . . . . . 5

1.2 Photoluminescence . . . . . . . . . . . . . . . . . . . . . . . . . 6

1.3 Optical Orientation of Spins . . . . . . . . . . . . . . . . . . . . 10

1.4 Optical Investigation of Spin Properties . . . . . . . . . . . . . . 15

1.4.1 Direct-gap Polarized Emission:
Temperature Dependence . . . . . . . . . . . . . . . . . . 16

1.4.2 Direct-gap Polarized Emission:
An Additional Tool to Control Light Polarization . . . 22

**2 Ge/SiGe Multiple Quantum Wells** **28**

2.1 SiGe Alloys . . . . . . . . . . . . . . . . . . . . . . . . . . . . . 28

2.2 Heterostructures and Strain . . . . . . . . . . . . . . . . . . . . 29

2.3 Quantum Wells . . . . . . . . . . . . . . . . . . . . . . . . . . . 31

2.4 Band Alignment and Band Structure . . . . . . . . . . . . . . . 32

2.5 Optical Properties . . . . . . . . . . . . . . . . . . . . . . . . . 37

2.6 Decay Time . . . . . . . . . . . . . . . . . . . . . . . . . . . . . 39

**3 (001)-Ge/SiGe MQWs: Spin Properties** **44**

3.1 Spin Relaxation of L-Valley Electrons . . . . . . . . . . . . . . . 44

3.2 Low Temperature Spin Lifetime . . . . . . . . . . . . . . . . . . 48

3.3 Spin Lifetime Dependence on Temperature . . . . . . . . . . . 52
3.4 Conduction Electron $g$-factor . . . . . . . . . . . . . . . . . . . 53

**4 Ge/SiGe MQWs (111)-Oriented 59**
4.1 Electronic Structure and Optical Properties . . . . . . . . . . 59
4.2 Investigation of the Spin Properties . . . . . . . . . . . . . . . 66
4.3 Spin Relaxation Time . . . . . . . . . . . . . . . . . . . . . . . 72

**Conclusions 75**

**A Methods 77**
A.1 Continuous Wave PL . . . . . . . . . . . . . . . . . . . . . . . 77
A.1.1 Line A . . . . . . . . . . . . . . . . . . . . . . . . . . 79
A.1.2 Line B . . . . . . . . . . . . . . . . . . . . . . . . . . 79
A.2 Time Resolved PL . . . . . . . . . . . . . . . . . . . . . . . . 81
A.2.1 Bench A . . . . . . . . . . . . . . . . . . . . . . . . . 81
A.2.2 Bench B . . . . . . . . . . . . . . . . . . . . . . . . . 83

**B Stokes Analysis 86**

**C Spin Lifetime Dependence on Temperature 92**

**Bibliography 93**

**Acknowledgements 106**

# Introduction

Spintronics [1] and photonics [2] are two mainstream pathways that are separately explored to enrich the performances of existing microelectronic devices. The tremendous potential that would be triggered by their joint implementation would open the route to a novel technology, known as Spin-OptoElectronics (SOE) [3]. SOE aims to design and develop a new generation of devices by combining standard microelectronic properties with spin-dependent effects and light-matter interaction. The main goal of such an attempt is to encode digital data in the electron spin, eventually overcoming the limitations of conventional charge-based electronics in terms of power consumption and processing speed, while preserving the large-scale and cost-effective production offered by the microelectronics foundries [4].

In this context, group IV semiconductors, like Si and Ge, are prominent candidates. Indeed, they are low-cost and readily-available substances that dominate the CMOS market. In addition, they possess ideal features for a future use as solid-state hosts of spin-based information [5, 6]. Their centrosymmetric crystal structure prevents the Dyakonov-Perel spin relaxation mechanism [7], which is a well known limitation in III-V compounds. This results in long spin lifetimes and diffusion lengths. Moreover, isotopic refinement can reduce hyperfine interactions, thus lengthening the spin coherence time [8]. Finally, wafer-scale epitaxy on Si substrates opens up the opportunity to introduce confinement and strain effects as effective degrees of freedom for the simultaneous manipulation of the electronic and spin properties.

Despite Si photonics relies on commercially available devices, such as waveguides, modulators and detectors, its full exploitation has been jeopardized by the lack of efficient light emitters, which results from the indirect

band gap of group IV semiconductors [9]. Among all group IV compounds, Ge has been recognized as the most prominent candidate to overcome the aforementioned drawbacks. Indeed, differently from Si, its small energy difference ($\Delta$E $\sim$ 140 meV) between the indirect- and the direct-gap guarantees access to the direct-gap optical transition, thus ensuring high absorption and emission efficiencies. As a result, the pseudo-direct-gap behaviour of Ge offers the unique possibility to exploit the coupling between the angular momentum of circularly polarized photons and the electronic spin state. In this way, spin polarized carriers can be efficiently oriented by the absorption of circularly polarized light through the direct-gap transition, while the polarization of emitted luminescence can be used to gather information about the physical mechanisms governing nonequilibrium spin dynamics.

Even though several decades ago the seminal work by Lampel in Si [10] put forward optics as a viable technique to address the spin physics of group IV materials, very little improvement has been made until very recently, when a better understanding and exploitation of light-matter interaction has led to all-optical investigations of spin dependent phenomena [11, 12, 13]. These research efforts unfold the possibility to fruitfully couple the angular momentum of photons and the spin angular momentum of charge carriers even in Si-based architectures [13]. Although SOE is still at an infant stage, its readily available spin-photon interfaces are inherently capable of modulating the state of light polarization and have a substantial potential to inspire and drive innovation in a wide range of applications, embracing quantum information processing and reconfigurable optical interconnects.

Within this landscape, the present work is a fundamental study about spin properties of conduction band (CB) electrons in Ge heterostructures. In particular, we have employed polarization-resolved photoluminescence (PL) to investigate the spin physics of Ge-based systems. One of the main advantages of this all-optical technique is to avoid spin depolarization arising from interfaces between ferromagnetic and semiconductor materials, which affect electrical measurements thus masking the intrinsic spin lifetime [14].

In this thesis we will focus on the optical generation of spin polarized carriers and on the polarization of the PL of bulk Ge and Ge/$Si_{1-x}Ge_x$ Multiple

Quantum Wells (MQWs) grown along different crystallographic orientations.

The work is organized as follows: At first we will discuss the role of doping in determining the spin-polarized population suffering direct-gap recombination in bulk Ge at low temperatures. Then we will show the possibility to additionally control the spin polarized ensemble by tuning the excitation power density. Eventually, we will demonstrate how this phenomenon can be utilized to achieve a complete control over the polarization of the direct-gap PL. This represents one of the central issues in the SOE field. Indeed, currently available light sources are incapable of adjusting the helicity of the emitted photons without the use of any external magnetic field or optical delay modulators [15, 16, 17].

The second part of this work is devoted to a thorough investigation of Ge-based MQWs. These heterostructures have been demonstrated to be very promising, since they exhibit a type-I band alignment and they provide the possibility to tailor the optical transition energies by means of strain and composition [18, 19, 20]. In Chapter 2, we will provide details about the QWs, namely growth technique, band alignment and band structure, and we will also discuss their optical properties. The third Chapter focuses instead on the spin properties of $Ge/Si_{0.15}Ge_{0.85}$ MQWs heterostructures grown along the (001)-oriented crystallographic direction. In particular, continuous wave PL (CWPL) and polarization- and time-resolved PL will be exploited to experimentally evaluate the role of intravalley scattering of L-valley electrons. The latter has been theoretically predicted as the dominant spin relaxation channel in the low temperature regime [21, 22]. Moreover, we will investigate the spin relaxation time $\tau_S$ (spin lattice relaxation time $T_1$) as a function of the well thickness and of the temperature. The last part of Chapter 3 addresses the Landé $g$-factor of CB electrons and its dependence on the well width. The $g$-factor was measured by means of Quantum Beat Spectroscopy (QBS) [23]. This optical technique, although used in the case of III-V group semiconductors [24, 25, 26], has never been applied, to date, to group IV materials. Our QBS data unambiguously reveal that we are able to achieve a coherent spin dynamics within the Ge-based heterostructures. Experimental $g$-factor values obtained via QBS are then compared both with those obtained

by means of electron spin resonance (ESR) on very similar Ge/$Si_{1-x}Ge_x$ MQWs samples [27] and with those predicted by a $k \cdot p$ theoretical calculation [28].

In Chapter 4, we will focus on Ge/$Si_{1-x}Ge_x$ MQWs sample grown along the (111)-oriented surface. This investigation was inspired by the fact that in these heteroepitaxial systems the L-valley degeneracy is lifted. This phenomenon has been recently suggested to be a major spin relaxation channel for CB carriers in Ge [21, 22]. In particular, we will show that it is possible to achieve robust optical orientation of spins, revealing a clear proof of non-vanishing polarization at room temperature. For (111)-oriented QWs, we will demonstrate a $\tau_S$ lying in the hundreds of ns regime, while a $\tau_S$ of few tens of ns is found in similar Ge/$Si_{1-x}Ge_x$ MQWs heterostructure grown along the (001)-oriented crystallographic direction. Such a spin lifetime difference represents a direct proof that strain can be utilized to lengthen the spin lifetimes in Ge.

In the Conclusions, the main results reported in this thesis are summarized. In the Appendix, full Stokes analysis of light polarization and the experimental set-ups will be fully described.

# Chapter 1

# Bulk Germanium

This chapter addresses optical investigations of spins in bulk Ge. In the following, we will first provide a detailed overview about photoluminescence, the optical orientation process and the polarized emission in bulk Ge. Then we will report a study of the direct-gap PL polarization as a function of doping and temperature. Finally, we will show that by tuning the excitation power density, it is possible to achieve control over the luminescence polarization in properly doped bulk Ge samples.

## 1.1 Structural and Electronic Properties

Ge is a group IV semiconductor (SC) exhibiting the diamond crystalline structure, which consists of two interpenetrating face-centred cubic Bravais lattices displaced along the diagonal of the cubic cell by one quarter of the length of the same diagonal. At room temperature (RT), the lattice constant $a$, shown in Figure 1.1(a), is of 0.566 nm.

Ge is an indirect-gap semiconductor [Figure 1.1(b)]. The top of the valence band (VB), located at the $\Gamma$ point of the Brillouin zone ($\mathbf{k} = 0$), is twofold degenerate and consists of heavy holes (HH) and light holes (LH) states, while the split-off (SO) band is located 290 meV below the top of the VB. The absolute minimum of the conduction band (CB) is located at the L point of the Brillouin zone along the $\langle 111 \rangle$ crystallographic directions. It

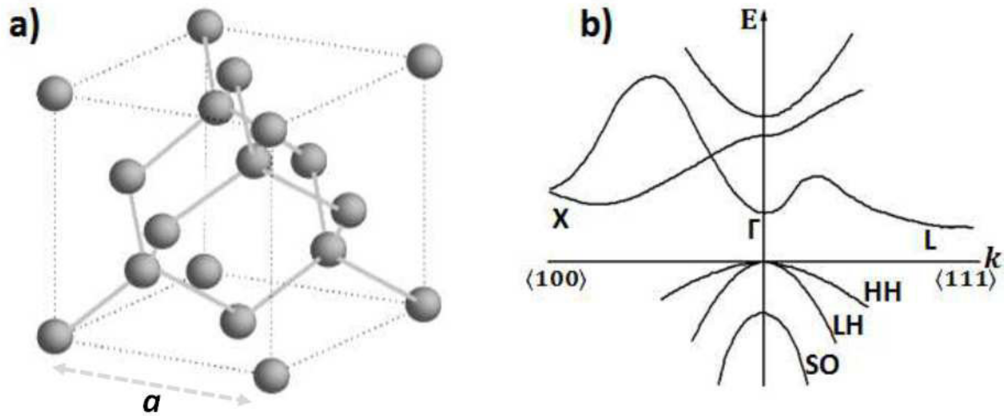


Figure 1.1: Cubic cell of the diamond lattice [30, 31] (a) and band structure of bulk Ge (b).

is four-fold degenerate and at RT it lies 0.66 meV above the top of the VB. Other Ge CB minima are then found at the Γ and X point, 140 meV and 200 meV above the absolute minimum, respectively.

Remarkably, due to the Γ-to-L proximity, Ge exhibits a quasidirect behaviour, which recently sparked interest also in its photonic properties [9, 29].

## 1.2 Photoluminescence

Photoluminescence (PL) is a non-destructive spectroscopic technique that provides access to the intrinsic and extrinsic electronic properties of SCs [32]. Upon optical excitation, a photon is absorbed by the crystal, thus creating an electron-hole pair which can then radiatively recombine, emitting another photon [33].

Assuming the excitation energy to be much larger than the energy difference between VB and CB at $\mathbf{k} = 0$ (i .e. $\hbar\omega \gg E_\Gamma$), electrons (holes) are photogenerated with a well-defined excess energy with respect to the CB minimum (VB maximum). After excitation, the whole process leading to PL signal consists of carriers thermalization, diffusion and radiative recombination.

Considering now a 100% internal quantum efficiency, so that one absorbed photon generates one electron-hole pair, immediately after absorption at normal incidence, the depth-dependent density of photogenerated carriers can be described by the *Beer's law*:

$$G(z) = [1 - R(\hbar\omega)] \cdot \alpha(\hbar\omega) \cdot I(0) \cdot exp[-\alpha(\hbar\omega) \cdot z], \tag{1.1}$$

where $z$ is the coordinate normal to the sample surface, $R(\hbar\omega)$ is the surface reflectivity of the sample, $I(0)$ is the incident photon density and $\alpha(\hbar\omega)$ is the absorption coefficient at the excitation energy.

If now we consider the case of infrared laser excitation, in Ge, the lifetime of electrons excited within the Γ valley is dominated by their ultrafast scattering towards satellite X and L valleys, lying in the regime of hundreds of femtoseconds [34, 35, 36]. The relaxation processes towards the bottom of Γ valley are slower than in III-V compounds, where phonon scattering is driven by the Fröhlich interaction allowing electrons to couple with longitudinal optic (LO) phonons with a high wave number. Such a mechanism is absent in Ge since the crystal bonds are purely covalent [37]. Moreover, the deformation potential interaction between long-wavelength optical phonons and CB electrons is weak in Ge due to the space inversion symmetry. Due to these mechanisms, the satellite valleys energy relaxation becomes the most efficient thermalization process [38]. Most of the electrons will thus suffer scattering towards the absolute minimum of the L-valley, where they exhibit a long lifetime: $\tau_L$ values are expected to be between ten and hundreds of $\mu$s at room temperature (RT) [33].

Simultaneously with the thermalization process, the concentration gradient causes carrier diffusion within the sample.

After thermalization and diffusion, electrons are distributed in the CB. A fraction of photoexcited carriers experiences radiative recombination, thus returning to the ground state (GS) via photon emission. Therefore it is possible to measure at the same time the direct- and indirect-gap transitions, that occur at different photon energies. The PL spectrum, which is due to the product between the joined density of states and the relative transition

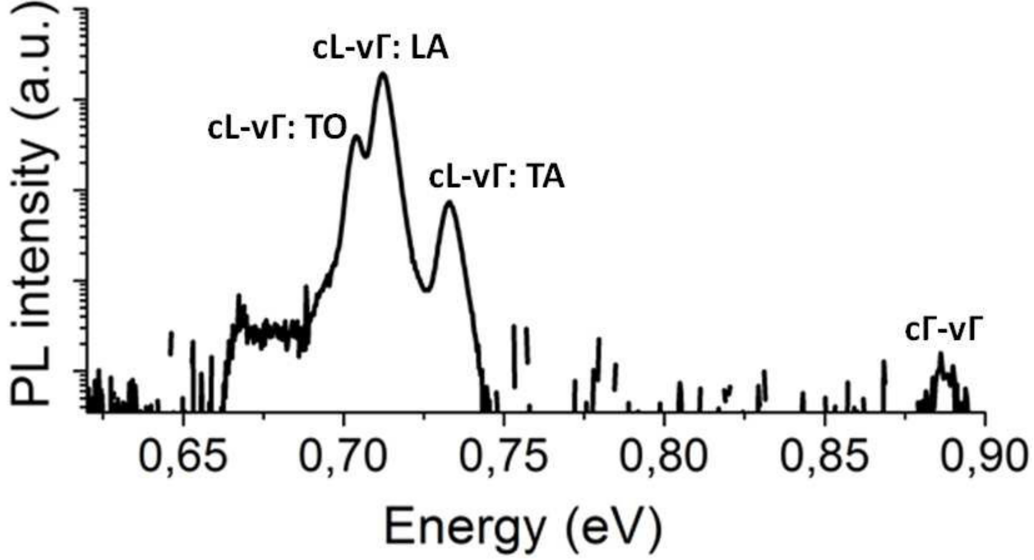


Figure 1.2: PL spectrum obtained from a nominally intrinsic Ge sample measured at T=4 K under 1.165 eV laser excitation with a power density of about 4.5 kW/cm$^2$. Phonon mediated indirect (cL - vΓ) and direct (cΓ-vΓ) transitions are shown. The PL was probed by means of a dispersive system followed by an InGaAs array photodiode working in the 0.55 - 1.55 eV range [39].

probability, represents the radiation intensity emitted by the sample as a function of the energy. In a typical PL spectrum of Ge, the emission due to the indirect cL$\longrightarrow$vΓ transition dominates over the emission due to the direct cΓ$\longrightarrow$ vΓ one (see Figure 1.2).

PL features related to indirect-gap emission are found in the low energy range of the PL spectrum, between 0.65 eV and 0.75 eV, and the main peaks are phonon replica of the cL - vΓ transition [40], labeled in Table 1.1. At about 0.66 eV, the PL spectrum shows a feature with much lower intensity with respect to other lines. Lieten *et. al* [40] attributed this structure to the radiative recombination assisted by two phonons: a (111) LA phonon and a TO phonon at the Γ point of the Brillouin zone.

A less intense PL peak related to the direct-gap emission is found at the high energy side of the spectrum, at about 0.88 meV. We now focus our attention on the cΓ-vΓ transition, which will be investigated in detail in the

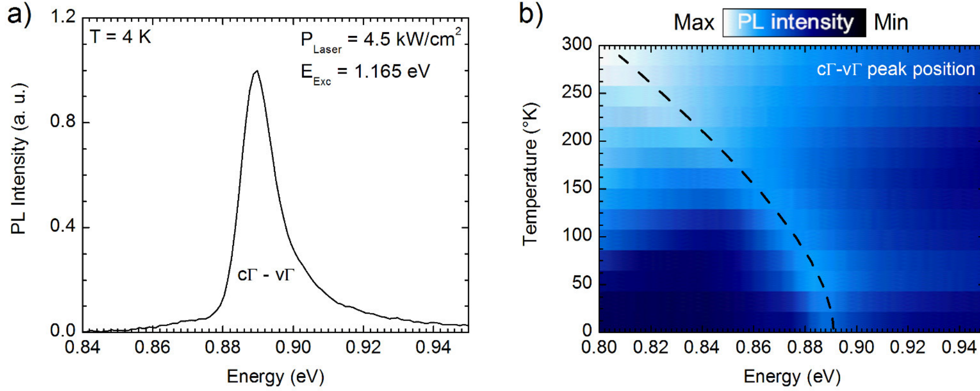


Figure 1.3: (a): Direct-gap PL spectrum obtained from the sample whose whole spectrum is shown in Figure 1.2. Here the PL signal is measured by means of a polichromator equipped with a thermoelectrically cooled InGaAs array detector with the cutoff energy at 0.75 eV, which guarantees an optimal spectral response in the direct-gap region emission. (b): Color-coded map of the PL intensity as a function of the temperature. Dashed line indicates the calculated energy position for the cΓ-vΓ PL feature [41].

Table 1.1: Energies of (111) phonons in bulk Ge at T=4 K and positions of the corresponding phonon replica of the indirect cL⟶vΓ transitions.

| *Phonon Label* | *Phonon Energy (meV)* | *Phonon Replica (meV)* |
|---|---|---|
| TA | 7.7 | 733 |
| LA | 27.4 | 712 |
| TO | 35.4 | 704 |

following.

The spectral asymmetry of the direct-gap PL can be observed in Figure 1.3 (a). The line shape is due to the joint density of states (JDOS) and the Maxwell-Boltzmann distribution of the photoexcited carriers. The latter describes the high energy tail of the PL peak via a negative exponential-like behaviour. Assuming parabolic bands for the direct band-to-band transitions, the PL spectrum intensity is given by:

$$I(\hbar\omega) = B \cdot \sqrt{\hbar\omega - E_\Gamma} \cdot exp(-\frac{\hbar\omega}{k_B T}), \tag{1.2}$$

where $B$ represents the radiative recombination probability for direct-gap

Table 1.2: Values of parameters in Equation 1.3 for indirect-gap and direct-gap transitions in Ge [42].

| *Type of Transition* | $E_\Gamma$ *(eV)* | $\alpha$ *(eV/K)* | $\beta$ *(K)* |
|---|---|---|---|
| Indirect | 0.7412 | 4.561 $\times 10^{-4}$ | 210 |
| Direct | 0.8893 | 6.842 $\times 10^{-4}$ | 398 |

transition. Therefore, the PL peak maximum intensity will not correspond to the energy difference between the VB maximum and the CB minimum at $\Gamma$ ($\mathrm{E}_\Gamma$), but it will be blue-shifted by an amount of $\frac{1}{2}\mathrm{k_B T}$ [32].

Figure 1.3 (b) shows the color-coded plot of the PL direct-gap emission of a nominally intrinsic Ge sample as a function of the temperature. The direct-gap PL peak position follows the behaviour described by the Varshni's law [42]:

$$E(T) = E(0) - \frac{\alpha T^2}{\beta + T}, \tag{1.3}$$

where values for $E(0)$, $\alpha$ and $\beta$ values for Ge are reported in Table 1.2. In particular, by increasing the temperature, the gap shifts to lower energies.

## 1.3 Optical Orientation of Spins

Optical orientation allows the generation of an unbalanced spin distribution within the semiconductor by means of circularly polarized light absorption [43], which owns angular momentum $L_z = \pm\hbar$ along the light propagation direction ($\hat{z}$). Photons possessing momentum $m_p = +1(-1)$ will be right(left) handed circularly polarized ($\sigma^{\pm}$). In a semiconductor, the photoexcited electrons and holes exist for a time $\tau_L$ before the recombination [7]. If a fraction of the carrier's initial orientation survives longer than the recombination time i. e. $\tau_S \sim \tau_L$, where $\tau_S$ is the spin relaxation time, then the PL will be partially polarized. In this case, the polarization degree can be used to gather information about the physical mechanisms governing the spin dynamics of non-equilibrium carriers in SCs, thus providing an unique tool for the investigation of useful quantities such as, for example, spin orientation, electron lifetime and spin relaxation time of injected carriers [44, 45].

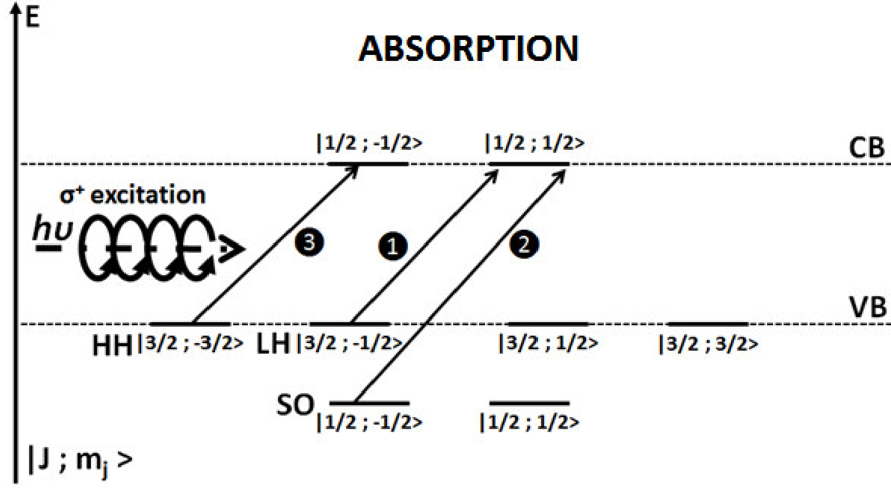


Figure 1.4: Γ-point states involved in the optical orientation process. States are labelled by the projection $m_j$ of the total angular momentum $J$ on the direction of light propagation $\hat{z}$. Arrows indicate the optical allowed transitions upon $\sigma^+$ laser excitation. The relative weight of the dipole matrix element is indicated in the circles.

The generation of a non-equilibrium distribution of spin-polarized carriers depends on the optical selection rules and the oscillator strength. It is worth noticing that at the centre of the Brillouin zone Ge behaves like a direct-gap III-V compound SCs [7]. The model used to describe the polarized absorption process is schematically described in Figure 1.4. From now on, we assume $\sigma^+$ for the helicity of the exciting light ($m_p = +1$). From the selection rules in the electric dipole approximation, we get $\Delta m = m_{jf} - m_{ji} = 1$, where $m_{ji}$ and $m_{jf}$ represent the initial and final projection of the total angular momentum ($J$) along the light propagation direction (z), respectively. Under these conditions, the allowed transitions ($|J, m_{ji}\rangle \longrightarrow |J, m_{jf}\rangle$) will thus be:

$$\begin{aligned} HH &: |+3/2, -3/2\rangle \longrightarrow |+1/2, -1/2\rangle \\ LH &: |+3/2, -1/2\rangle \longrightarrow |+1/2, +1/2\rangle \\ SO &: |+1/2, -1/2\rangle \longrightarrow |+1/2, +1/2\rangle. \end{aligned} \tag{1.4}$$

Therefore, immediately after the light absorption, both photoexcited holes

and electrons are spin polarized. The absorption of $\sigma^+$ ($\sigma^-$) polarized light corresponds to a difference of +1 (-1) between the $m_j$ values of the final and initial state. As a result, photoexcited electrons from the HH and LH states populate opposite spin levels in the CB (see Figure 1.4).

For $E_g \leq \hbar\omega \leq E_g + \Delta SO$, only LH and HH sub-bands provide contributions to the absorption process, resulting in a net spin polarization defined as:

$$P_n = \frac{n_+ - n_-}{n_+ + n_-}, \tag{1.5}$$

where $n_+$ ($n_-$) stands for the density of electrons co(counter) polarized with respect to the exciting photons. If now we consider an electric-dipole transition with $\Delta \mathrm{J} = -1$, the matrix element for $\sigma^+$ excitation condition is given by [46]:

$$|\langle J-1, m_j+1|\sigma^+|J, m_j\rangle|^2 = 1/2(J-m_j)(J-m_j-1). \tag{1.6}$$

Hence, performing the calculation, it results that the square of the matrix element for transitions involving HH states is three times larger than that for transitions involving LH states. Thus, under $\sigma^+$ excitation conditions, we have $n_+ : n_- = 1 : 3$, and from Eq. 1.5 it follows that $P_n = -1/2$. In this case, the overall spin is oriented oppositely with respect to the light propagation direction. It is worth noticing that, assuming $\sigma^-$ excitation, we would have $n_+ : n_- = 3 : 1$ and $P_n = +1/2$.

It is well known that the holes depolarization is very fast ($\tau_s^{holes}$ ~1 ps [47]), so that only the spin polarization of electrons will contribute to the PL signal, as shown in Figure 1.5. In this case, the PL circular polarization degree is defined by [46]:

$$\rho = \frac{I_{\sigma^+} - I_{\sigma^-}}{I_{\sigma^+} + I_{\sigma^-}}, \tag{1.7}$$

where $I_{\sigma^\pm}$ represents the intensity of $\sigma^\pm$ polarized light. Moreover, due to the complete depolarization of holes, spin states at the VB are equally occupied and $I_{\sigma^\pm}$ will only depend on the spin states within the CB and on the relative transition probability with $\sigma^\pm$ photon emission. Therefore, $I_{\sigma^\pm}$ is proportional to the sum of c$\Gamma$ -1/2 and c$\Gamma$ +1/2 contributions to the polarized

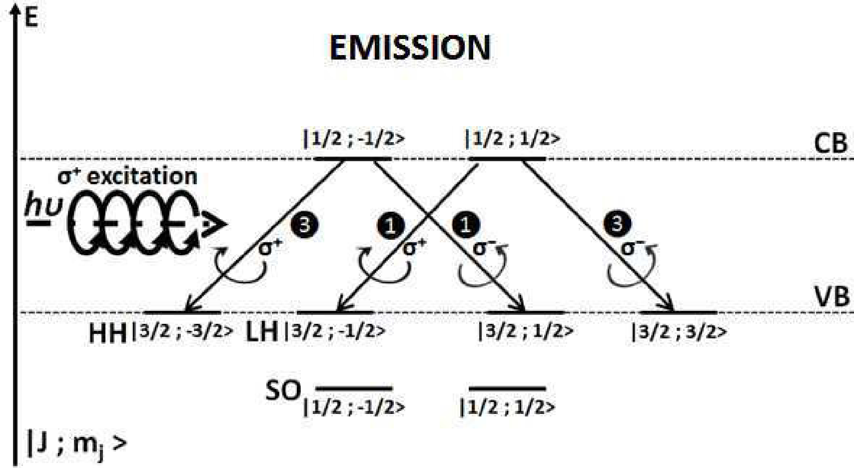


Figure 1.5: Γ-point states involved in the polarized emission process. States are labelled by the projection $m_j$ of the total angular momentum $J$ on the direction of light propagation $\hat{z}$. Arrows indicate the optical allowed transitions upon $\sigma^+$ laser excitation. The relative weight of the dipole matrix element are indicated in the circles.

emission. Thus, from Eq. 1.7, we get:

$$\rho_0 = \frac{(n_+ + 3n_-) - (3n_+ + n_-)}{(n_+ + 3n_-) + (3n_+ + n_-)} = \frac{1}{4}, \tag{1.8}$$

where $\rho_0$ indicates that we are neglecting spin depolarization mechanisms.

If we consider now excitation involving also transitions from the SO band (i. e. $\hbar\omega > E_g + \Delta SO$), it can be easily deduced that, after circularly polarized light absorption, we have $n_+ = n_-$, so the net spin polarization is null ($P_n = \rho = 0$). This underlines the importance of spin-orbit coupling in the optical spin orientation process. On the other hand, the VB spin states structure shown in Figures 1.4 and 1.5 clearly suggests that a removal of the $HH/LH$ degeneracy can substantially increase $P_n$ up to the limit of complete spin polarization [48].

While, as we will see, photoexcitation with circular polarized light creates spin-polarized electrons, the nonequilibrium spin polarization decays due both to carrier recombination and spin relaxation mechanisms [49, 50]. In continuous-wave PL (CWPL) experiments, the steady-state polarization

degree depends on the balance between spin excitation and decay. In a homogeneously doped SC, the balance between electron-hole recombination and optical pair creation can be written as:

$$r \cdot (n \cdot p - n_0 \cdot p_0) = G, \tag{1.9}$$

where $r$ is the recombination rate, $n$ and $p$ the electrons and holes densities, with the 0 subscript denotes the equilibrium values, and $G$ is the electron-hole photoexcitation rate. Similarly, the balance between spin relaxation and spin generation can be expressed by:

$$r \cdot s \cdot p + s/\tau_S = P_n(t = 0) \cdot G, \tag{1.10}$$

where $s = n_+ - n_-$ is the electron spin density and $P_n(t = 0)$ represents the spin polarization immediately after photoexcitation. Remembering that holes are considered unpolarized, the first term in Eq. 1.10 describes the spin density decay due to carrier recombination, while the second term describes intrinsic spin relaxation. Merging Eq. 1.9 and Eq. 1.10, we obtain the steady-state electron polarization [51]:

$$P_n = P_n(t = 0) \cdot \frac{1 - n_0 \cdot p_0/n \cdot p}{1 + 1/\tau_S \cdot r \cdot p}. \tag{1.11}$$

In a *p-doped* sample, $p \sim p_0$ and $n \gg n_0$, so that $n_0 \cdot p_0/n \cdot p \simeq 0$, and we can write:

$$P_n = \frac{P_n(t = 0)}{1 + \tau/\tau_S}, \tag{1.12}$$

where $\tau = 1/r \cdot p_0$ is the electron lifetime [32]. The steady-state polarization is thus lower than the initial polarization $P_n(t = 0)$ by an amount depending on the ratio $\tau/\tau_S$.

In an *n-doped* sample, on the other hand, $n \sim n_0$ and $p \gg p_0$, Eqs. 1.9 and 1.11 thus give [52]:

$$P_n = \frac{P_n(t = 0)}{1 + n_0/G \cdot \tau_S}. \tag{1.13}$$

Contrary to the previous case, the majority carrier (now holes) lifetime $\tau =$

$1/r \cdot n_0$ has no effect on $P_n$. However, $P_n$ depends on the photoexcitation intensity $G$ as expected for a pumping process.

In conclusion, the steady-state spin polarization $P_n$ under circularly polarized laser excitation depends on the electrons spin relaxation time. In particular, the longer $\tau_S$, the larger $P_n$. However even if $\tau_S$ is very long, $P_n$ is limited by its initial value, $P_n(t = 0)$. A detailed calculation of $P_n$ as a function of photon energy ($\hbar\omega$) can be found in Ref. [53].

It is worth noticing that the optical orientation process described above is valid at the zone centre, where the Ge mimics the behaviour of III-V compound SCs. In the latter all the photoexcited carriers suffer direct-gap recombination, whereas the multi-valley nature of Ge CB allow carriers to experience inter-valley scattering towards the X and L valleys, as discussed in Section 1.2. This property, together with the above mentioned pseudo-direct band structure of Ge, makes spin dynamics richer. In the following, we will show that it is possible to exploit these properties in order to address new interesting routes towards the study of spin physics properties.

## 1.4 Optical Investigation of Spin Properties

This section provides details about recent investigations of spin and energy relaxation processes in bulk Ge. All the data discussed in the following refer to polarization-resolved PL (PRPL) measurements carried out in backscattering geometry. A full discussion of the experimental set-up is given in Appendix A.1 (Line A). Samples were excited by a continuous-wave $\mathrm{Nd : YVO_4}$ laser operating at 1.165 eV (i. e. 1064 nm). Incident light was left-handed ($\sigma^-$) circularly polarized. The polarization state of emitted light was probed by means of a rotating quarter ($\lambda/4$) waveplate followed by a linear polarizer. In the following the retarder angle between the $\lambda/4$ and the linear polarizer will be termed analyser angle. The PL peak amplitude as a function of the analyser angle was measured by a spectrometer equipped with an InGaAs array multiple-channel detector with cutoff energy at 0.75 eV (Appendix A.1.1). PL spectra are measured at different orientation angles ($\theta$) between the fast axis of the analyzing $\lambda/4$ waveplate and the linear polarizer axis. The depen-

Table 1.3: Room temperature (RT) free carriers concentration and resistivity of investigated bulk Ge (001) samples. The *n-Ge* sample is 6° miscut.

| Sample name | Free carriers concentration ($cm^{-3}$) | RT Resistivity ($\Omega \cdot cm$) |
|---|---|---|
| *i-Ge* | $\sim 10^{13}$ | 47 |
| $p^{-}$*-Ge* | $1.4 \cdot 10^{15}$ | 2.39 |
| $p^{+}$*-Ge* | $3.6 \cdot 10^{18}$ | $4.6 \cdot 10^{-3}$ |
| *n-Ge* | $8.3 \cdot 10^{16}$ | $3.58 \cdot 10^{-1}$ |

dence of the PL peak intensity on $\theta$ allowed us to perform a Stokes analysis (Appendix B) of the data, thus providing information about the helicity and the circular polarization degree ($\rho$, Equation 1.7) of the emitted light.

In this section we will first report a study related to the direct-gap emission as a function of temperature and doping, in order to highlight the rich dynamics of CB electrons [38, 54]. The list of investigated samples is given in Table 1.3.

We will then demonstrate how these inherent properties of Ge can be utilized to achieve a complete control over the polarization state of the emitted light by simply modulating the excitation power density, without the need of any external magnetic fields (MF) or optical delay modulators.

### 1.4.1 Direct-gap Polarized Emission: Temperature Dependence

The low temperature PL peak related to the c$\Gamma$-v$\Gamma$ transition is found at $\sim$ 880 meV for all the samples (see Figure 1.6). In doped samples, the direct-gap emission lines are red shifted with respect to that of i-Ge (886 meV). This fact has to be ascribed to the band gap narrowing (BGN) effect, predicting a progressive gap shrinkage by increasing the impurity concentration [55, 56, 57]. The low energy feature of $p^{-}$-Ge at $\sim$ 0.87 eV may be attributed to recombination of shallow state carriers.

Under 1.165 eV excitation condition, luminescence has contributions from two types of spin polarized electrons [Figure 1.7 (a)]. The low temperature photogenerated electron population was evaluated in Ref. [59] by means

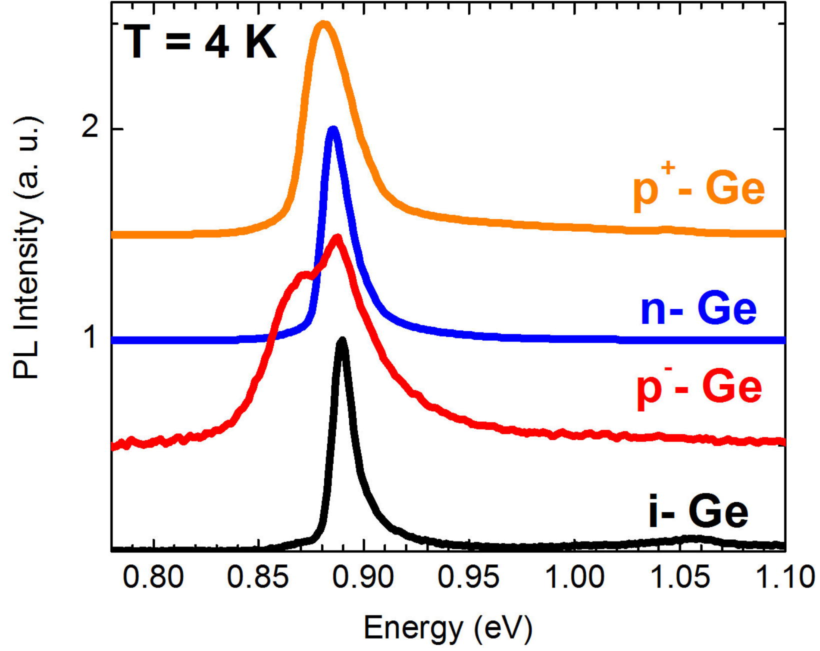


Figure 1.6: Normalized direct-gap PL features of the samples listed in Table 1.3. Spectra were obtained by means of 1.165 eV laser excitation with a power density of $\sim 4.5$ kW/cm$^2$.

of a first-neighbour tight-binding Hamiltonian[1] [Figure 1.7 (b)]. Though these calculations have been carried out for the case of Ge under a small tensile strain of about 0.2%, they fully capture the physics of spin-polarized carriers also in relaxed bulk materials. More precisely, transitions involving HH states produce CB electrons with excess energies, with respect to the Γ-valley bottom edge, of about 260 meV. Therefore, after absorption, they populate high energy Γ-valley states, and we will term them 'high energy' electrons. On the other hand, electrons promoted from the SO band have only a few $meV$ of kinetic energy, so that we will refer to them as 'low energy' electrons. It is worth emphasizing that, despite the low number of electrons excited from SO band, they are directly photoexcited to the Γ-valley bottom, thus providing relevant contribution to the direct-gap transition.

According to the selection rules (Section 1.3), under $\sigma^-$ excitation, the

[1] Simulation was carried out by Dr. Michele Virgilio at the University of Pisa.

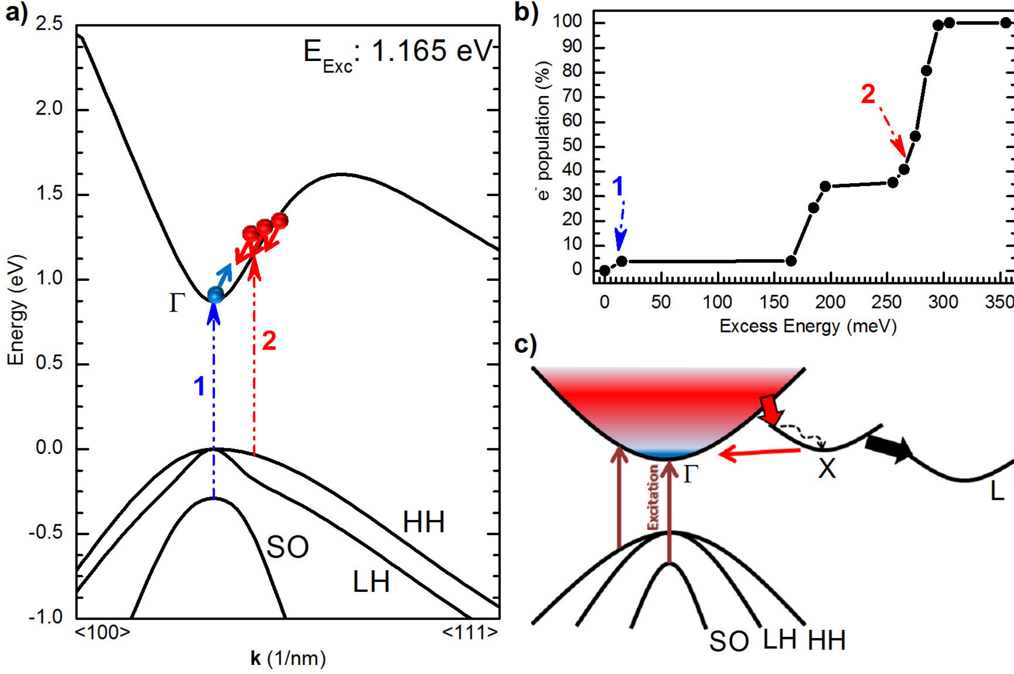


Figure 1.7: (a): Ge band structure calculated by using the 30 bands k · p calculation tool discussed in Ref. [58]. Arrows indicate $\sigma^-$, 1.165 $eV$ laser excitation. The possibility to create an unbalanced electron spin population within the Ge CB is shown. (b): Relative electron population as a function of the excess energy optically promoted by $\sigma^-$ excitation in a strained Ge/Si heterostructure [59]. Calculation was performed by means of a first-neighbour tight-binding Hamiltonian. (c): Sketch of the Ge band structure reporting the available relaxation pathways for the photoexcited carriers.

'high energy' electrons population provides a $\rho = -25\%$ for the c$\Gamma$ − v$\Gamma$ transition, while the contribution of the 'low energy' one is 50%. The PL polarization degree and type depends on the relative contribution of 'low energy' and 'high energy' electrons. Above all, the final degree of circular polarization will be dictated by relaxation mechanisms, as described below.

The colour-coded plot reporting the intensity modulation of to the direct-gap emission in the 4 K-180 K temperature regime for all the samples in Table 1.3 is shown in Figure 1.8 (a), while the temperature dependence of $\rho$ is shown in Figure 1.8 (b). Data are taken from Refs. [38, 54]. The laser power density was about 7.4 kW/cm$^2$. Attributing negative (positive) values

of $\rho$ to co (counter)-circular photon emission, we can identify three different temperature regimes:

- 4 K $\leq$ T $\leq$ 90 K. The sinusoidal modulation of the peak intensity reveals for all samples a non-vanishing optical orientation of CB electrons, as discussed in Section 1.3. The PL of $p^+$-Ge and n-Ge, is co-circular with respect to the excitation with $\rho \sim -8\%$ and $\rho \sim -11\%$, respectively. On the other hand, the other two samples exhibit a counter-polarized luminescence signal with $\rho \sim +30\%$ for i-Ge and $\rho \sim +5\%$ for $p^-$-Ge.

- 90 K $\leq$ T $\leq$ 170 K. The direct-gap PL is still circularly polarized. Remarkably the helicity of emitted photons in $p^+$-Ge and n-Ge is out of phase compared to the low temperature regime, so that the angular momentum of the direct-gap PL has the opposite direction of the one of the absorbed photons, reaching a positive maximum around T = 125 K for all the samples.

- 170 K $\leq$ T $\leq$ 300 K. The sinusoidal pattern for all the investigated sample is absent. In this temperature regime the emitted light is no more circularly polarized, demonstrating that electrons spins are no longer aligned before the recombination and $\rho$ approaches a null value.

From these experimental evidences [38], it is clear that the relative portion of 'high energy' and 'low energy' electrons taking part in the luminescence process strongly depends on the extrinsic carrier concentration and lattice temperature. A theoretical Monte Carlo simulation was performed in Ref. [38] to explain such non-trivial behaviour.

Due to the indirect-gap nature of Ge, the vast majority of optically-oriented electrons photoexcited into the $\Gamma$ valley suffer relaxation towards the absolute CB minimum, lying at the $L$ valley. However, here we focus our attention on the minor fraction of electrons experiencing direct-gap radiative recombination from the $\Gamma$ valley bottom. Indeed, information about the degree of circular polarization of this luminescence represents an useful tool to understand the relaxation mechanisms governing the dynamics of photoexcited electrons. As shown in Ref. [38], in Ge, the polarization state of the

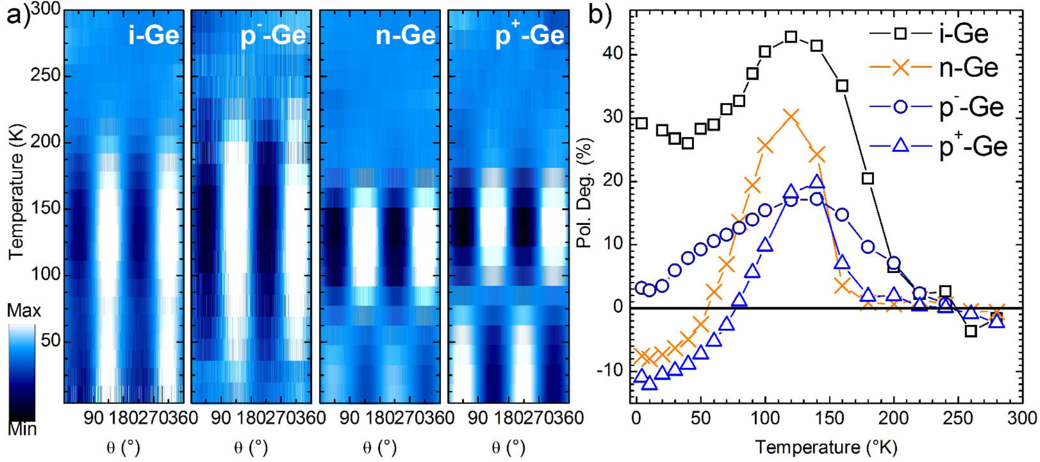


Figure 1.8: (a): Colour-coded maps reporting the temperature dependence of the intensity modulation of the direct-gap PL peak as a function of the analyser angle ($\theta$) for Ge samples listed in Table 1.3. (b): Temperature Dependent circular polarization degree. Data taken from Ref. [38].

direct-gap emission is governed by the kinetics of spin-polarized electrons, proving that scattering towards lateral X valleys plays an important role for the energy relaxation of electrons photoexcited from HH VB states.

Figure 1.9 shows results of Monte Carlo simulations [38], which fully recover experimental data reported in Figure 1.8 (b). The physical picture that we will describe in the following results from this theoretical calculation and the dynamics simulated by means of Monte Carlo. These calculations demonstrate that, 'high energy' electrons, are likely to suffer intervalley scattering towards the X valleys, demonstrating that the dynamics of these electrons within the X states depend on doping conditions. In the case of negligible free carrier concentration, electrons transfer towards the absolute L valley minimum through the efficient phonon-induced intervalley scattering. The net result is that the direct-gap emission is dominated by 'low energy' electrons, excited from SO VB states. This physics explains the counter-polarized emission of the intrinsic sample at low temperature, and its high circular polarization degree. On the other hand, in doped samples, energy relaxation of electrons is governed by collisions with extrinsic carriers (background carriers), being more effective in the X states rather than in the Γ

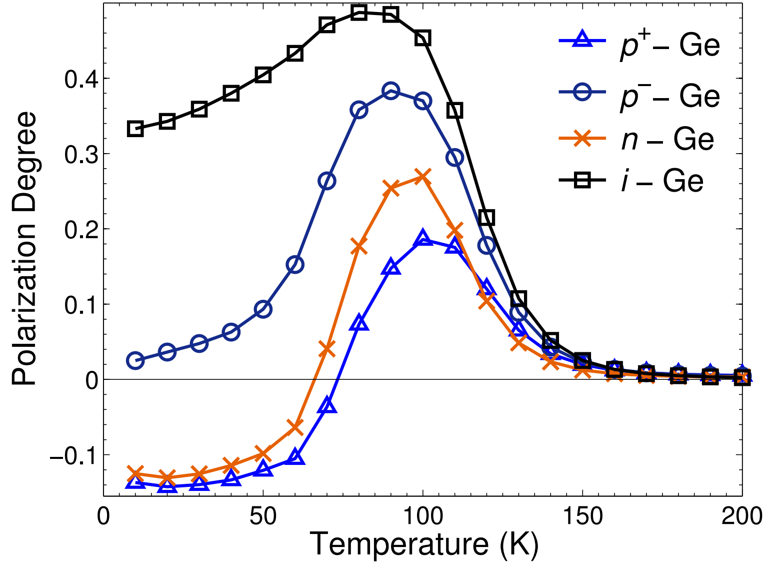


Figure 1.9: Monte Carlo calculation of the degree of circular polarization of the direct-gap recombination of bulk Ge under $\sigma^-$ laser excitation. Data taken from Ref. [38].

valley, due to the similarity of the electron mass to the one of background carriers. Following this picture, 'high energy' electrons reaching the bottom of the X valleys are mainly transferred towards the $L$ states, but a small fraction of them can experience backscattering towards Γ. Since $\Delta E_{X,\Gamma} \sim 40$ meV, they directly reach the valley bottom, providing a significant contribution to the direct-gap PL. As a result, we observe co-polarized emission in doped samples. Increasing the doping level led to an enhancement of 'high energy' electrons and, consequently, to a more negative value of $\rho$ (Figure 1.8 and Figure 1.9). Furthermore, it is worth noticing that n-Ge and $p^+ - Ge$ samples show similar $\rho$ behaviour, this means that extrinsic electrons and holes seem to affect the polarization in the same way.

Let us now focus on the high temperature regime. As the temperature increases, the band-gap shrinks, according to the Varshni's law (Equation 1.3). Hence, the relative weight of 'low energy' and 'high energy' electron populations changes, leading to a changes of $\rho$. Below T=50 K, the band gap shrinks only by $\sim 3$ meV, and experimental findings exhibit an almost constant $\rho$ behaviour. On the other hand, Figure 1.8 shows that above 50

K, $\rho$ increases in all the samples. In this case the band gap shrinkage causes a significant increase of the contribution of 'low energy' electrons to the polarized emission, which explains the behaviour of the circular polarization degree above T=50 K in all samples. Noteworthy, the $\rho \sim +50\%$ measured in i-Ge sample at T=120 K indicates that only electrons photoexcited from SO band provides a contribution to the direct-gap PL.

Above T=120 K, the thermal activation of spin depolarization mechanisms, shortening the spin relaxation time relative to the carriers lifetime (Eq. 1.12), reduces the degree of circular polarization, and above T=170 K the direct-gap emission from bulk Ge is no longer polarized in all samples.

The main depolarization source is the thermal activation of L-valley electrons. In particular, electrons lying in the L-valley bottom can visit the Γ valley. This process is characterized by a probability $\sim \exp(-\Delta E_{\Gamma,L}/k_B T)$, with $\Delta E_{\Gamma,L} \sim 140$ meV. At RT, the recombination lifetime of electrons in the L valley is longer than 1 $\mu$s, while the spin relaxation time was estimated to be of about 1 ns [22]. Consequently, the majority of L-valleys electrons ultrashort visits at Γ takes place when electrons are already unpolarized.

### 1.4.2 Direct-gap Polarized Emission: An Additional Tool to Control Light Polarization

The possibility to partially tailor the polarization type and degree of the cΓ-vΓ transition in Ge by means of doping was demonstrated in the previous section (Figure 1.8).

Here we will exploit the relaxation dynamics of 'high energy' electrons which, as it turns out, governs the polarization state of the emitted light. Indeed, we will demonstrate the capability of engineering the helicity of the emitted photons by simply tuning the density of photoinjected carriers, i. e. by changing the excitation power density. In particular, to address this issue, we found that among all the samples listed in Table 1.3, the intermediate doping concentration sample, named n-Ge ($Ge : As \sim 10^{16}$), could represent the best choice and hence we have studied it in detail.

Measurements reported here were taken under 1.165 $eV$, right-handed

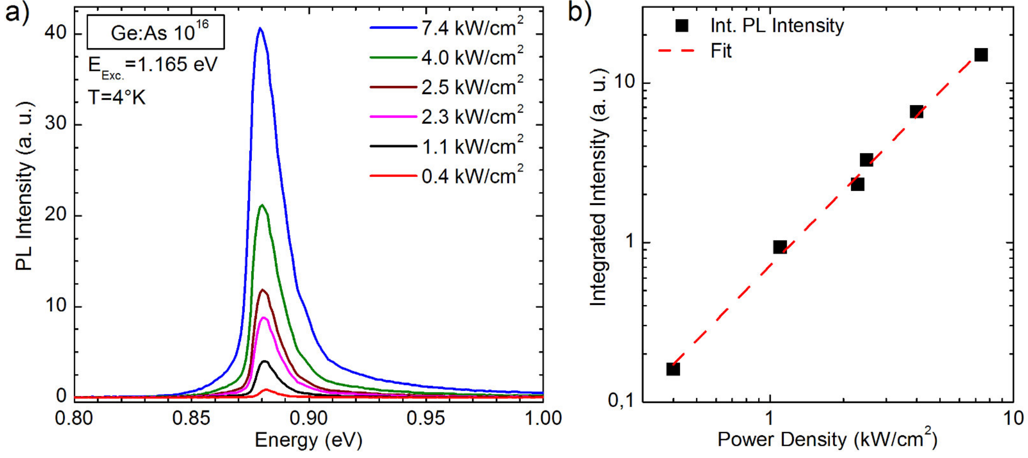


Figure 1.10: (a): Direct-gap PL emission of n-Ge as a function of the excitation power density. (b): Integrated PL intensity as a function of the excitation power density.

($\sigma^+$) circularly polarized laser excitation. In this case, we attribute positive(negative) values of $\rho$ to co(counter)-circular photon emission. The power density (P. D.) ranged from 0.4 kW/cm$^2$ to 7.4 kW/cm$^2$.

In this section, together with the PL peak intensity modulation, we will also report Poincaré spheres to represent the photon polarization (Appendix B). In this study, the Poincaré sphere is only used to show the polarized component of the luminescence, in order to facilitate the data interpretation. The relative degree of circular polarization can be deduced from the PL peak intensity modulation as a function of the rotating $\lambda/4$ waveplate (Appendix A.1). Since measurements reported in this section were taken using right-handed ($\sigma^+$) circularly polarized excitation, a point on the north(south) pole implies that emitted light is co(counter)-circular polarized with respect to laser helicity.

Figure 1.10 (a) shows the c$\Gamma$-v$\Gamma$ emission line obtained from the n-Ge sample as a function of the incident power density. As expected, the integrated PL peak intensity (plotted in Figure 1.10) strongly depends on the photoinjected carrier density. It is worth emphasizing that this dependence is superlinear, resulting in an exponent of $\sim 1.55$ (red-dashed line of Figure 1.10 (b)), in good agreement with literature data [60].

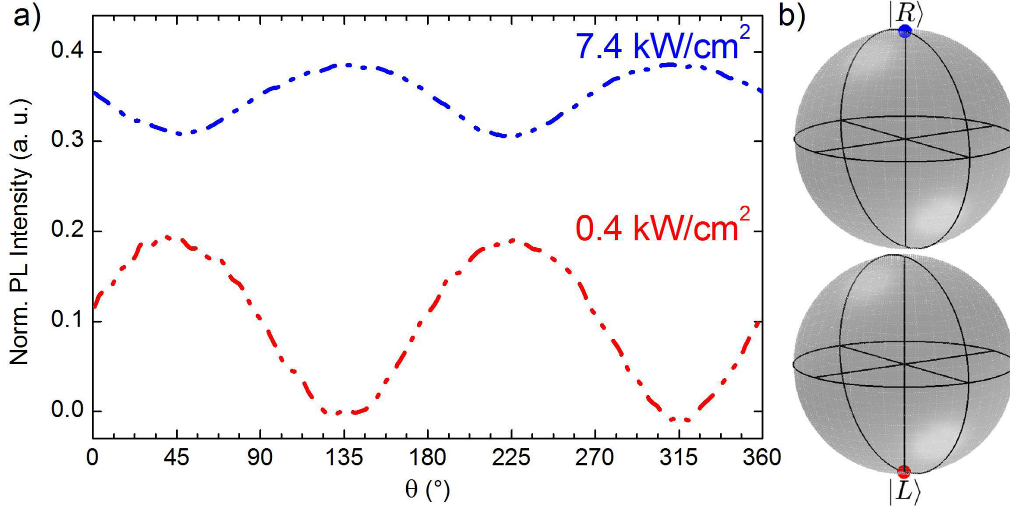


Figure 1.11: (a): Modulation of the direct-gap PL intensity of n-Ge sample at T=4 K for an excitation power density of 0.4 kW/cm$^2$ (blue dash-dotted line) and 7.4 kW/cm$^2$ (red dash-dotted line). (b): Poincaré sphere representing the polarized component of the PL signal.

Moreover, it is worth to underline the slight PL peak maximum red-shift which can be observed by increasing the excitation power density. Considering the two extrema P. D. values (0.4 kW/cm$^2$ and 7.4 kW/cm$^2$), we observe an overall shift of about 3 meV, which can be ascribed to a local lattice heating of $\sim$40 K.

Figure 1.11 (a) reports the direct-gap PL peak intensity modulation as a function of the $\lambda/4$ angle. Surprisingly, the measurements performed at P. D. = 0.4 kW/cm$^2$ (blue dash-dotted line) and P. D. = 7.4 kW/cm$^2$ (red dash-dotted line) clearly exhibit a 90° phase shift of the peak modulation, demonstrating the opposite helicity of the emitted photons. In particular, it is worth noticing that at a P. D. = 0.4 kW/cm$^2$, the peak modulation reveals maxima at $(\pi/4 + n\pi)$ and minima at $(3\pi/4 + n\pi)$. Under $\sigma^+$ polarized laser this corresponds to photon emission counter-polarized with respect to the excitation. On the other hand, when the incident laser power increases, the PL peak modulation exhibits maxima at $(3\pi/4 + n\pi)$ and minima at $(\pi/4 + n\pi)$, resulting in a photon emission co-polarized with respect to the excitation. The polarized component of the Poincaré spheres in Figure 1.11

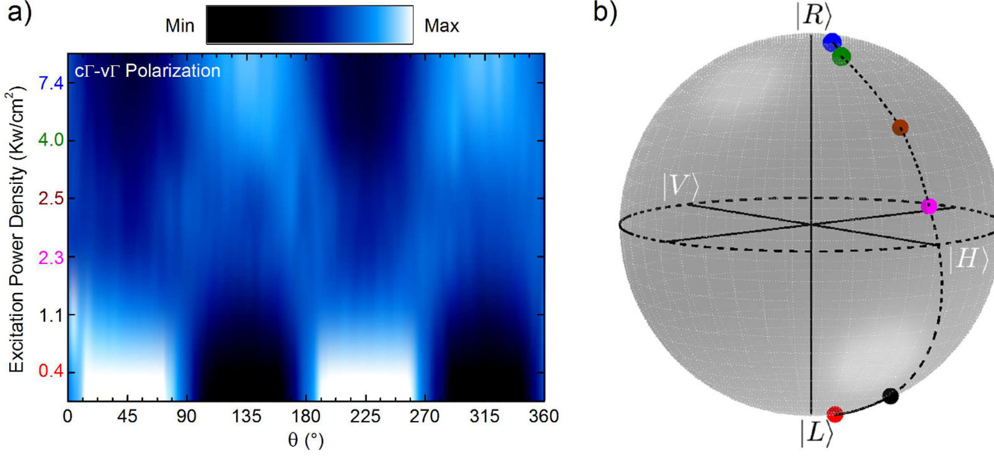


Figure 1.12: (a): Colour-coded map showing the direct-gap PL intensity as a function of the $\lambda/4$ analyser angle ($\theta$) measured by changing the excitation power density. (b): Polarized component of the Poincaré sphere representing the data of Figure 1.12 (a) .

(b), again shows that for the high(low) excitation power density, the cΓ-vΓ emission is co(counter)-polarized with respect to excitation.

Notably, Figure 1.12 (a) and (b) show that the photon helicity changes from $\sigma^+$ to *linear* to $\sigma^-$ simply by changing the number of photoinjected carriers, i. e. the excitation power density. The intermediate doping level of the n-Ge sample indeed allows us to achieve a complete control over the PL polarization.

The polarization switching can not be ascribed to the lattice heating due to laser power enhancement. We have shown (Figure 1.8) that for increasing temperature, the helicity of the emitted photons changes, moving from co-circular to counter-circular, in stark contrast with these findings. In Section 1.4.1 we underlined the crucial role played by the phonon-induced inter-valley scattering of 'high energy electrons' towards the satellite X and L valleys during the energy relaxation process. In this case, a plausible scenario is that, in the low P. D. regime, 'high energy' electrons suffer scattering towards satellite valleys, providing no contribution to the direct-gap recombination. In this case, the direct-gap PL signal is governed by 'low energy' electrons, thus resulting in a cΓ-vΓ luminescence emission counter-polarized with re-

spect to the excitation. On the other hand, when we increase the number of injected carriers (high P. D. excitation condition), 'high energy' electrons are more likely to thermalize towards the X valley bottom via Coulomb-induced collisions. Here, the phonon-induced inter-valley scattering causes a non-negligible probability for some of these electrons to be transferred back to the $\Gamma$ valley, where they can provide a sizeable contribution to the direct-gap recombination. In this case, the helicity of the emitted photons is co-polarized with respect to the excitation. It is worth emphasizing that the low power density excitation regime is characterized by a higher absolute value of the circular polarization degree ($\rho \sim |10\%|$) with respect to the high one ($\rho \sim |4\%|$). This is in line with the assumed physical picture, that is 'high energy' electrons contribute to the direct-gap luminescence in the former regime, while their contribution is reduced in the latter regime.

If, on one hand, modulation of the PL peak intensity reveals the polarization state of emitted light in the low and high excitation power density regimes, only little clarification is available in the intermediate regime from the data set of Figure 1.12. $\sigma^+$ and $\sigma^-$ PL spectra are shown in the upper panel of Figure 1.13 (a). The excitation power density was estimated to be around 2.8 kW/cm$^2$. In is worth noticing that, in this case, the degree of circular polarization exhibited by the PL peak maximum vanishes. However, this does not mean that the direct-gap PL emission is completely depolarized. Indeed, looking at the colour-coded map reported in the lower panel of Figure 1.13, it can be observed that there are four ninety-degrees phase shifted features. Thus, as explained in Appendix B, this P. D. regime is characterized by a photon helicity emission that is linearly polarized (along horizontal direction) with respect to the laser excitation. The linear character of the polarization state of the emitted light can also be appreciated from the green line (middle spectrum) of Figure 1.13 (b). Moreover, modulation intensities relative to the low (red line) and high (blue spectrum) energy tail of the $c\Gamma - v\Gamma$ transition are reported in Figure 1.13 (b), clearly showing a phase shift between maxima. These findings suggest that the low energy tail of the direct-gap luminescence is dominated by recombination of electrons excited from SO VB states, thus providing a counter-polarized photon emission. On

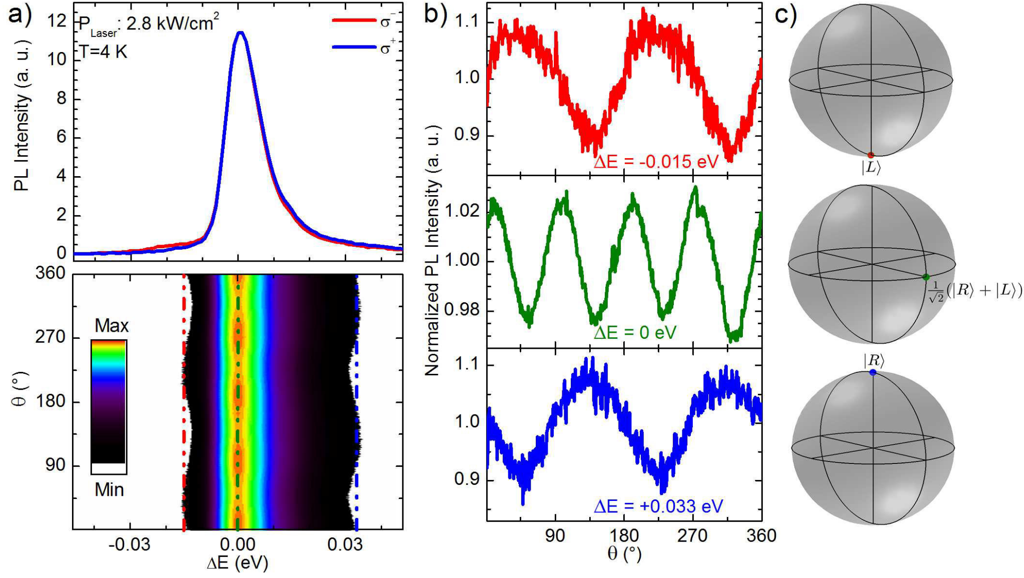


Figure 1.13: (a): $\sigma^+$ (blue line) and $\sigma^-$ (red line) resolved direct-gap PL spectra obtained from n-Ge sample. In the lower panel the colour-coded map shows the modulation of the PL peak intensity as a function of ΔE. ΔE is defined by setting the PL peak maximum as ΔE=0 eV. Excitation power density was 2.8 kW/cm$^2$. (b): Intensity modulation relative to the PL peak maximum, ΔE=0 eV (green line, central panel), to its low energy tail, ΔE=-0.015 eV (red line, upper panel) and high energy tail, ΔE=+0.033 eV (blue line, lower panel). Data are reported alongside the corresponding projection on the Poincaré sphere (c).

the contrary, electrons excited from the HH VB states dominate the high energy tail of the PL feature, so that this region is co-polarized with respect to the excitation. Such a behaviour strongly highlights that, for intermediate values of the excitation power density, coherent superposition of co-circular and counter-circular photon emission occurs, leading to a linear polarization state of the emitted light.

# Chapter 2

# Ge/SiGe Multiple Quantum Wells

This chapter provides an introduction to the Ge-based heterostructures whose spin properties will be investigated in details in Chapters 3 and 4, being the central topics of this thesis. In the first part of this chapter we will introduce structural and electronic properties of SiGe bulk alloys. Then we will devote particular attention to the effect of strain on the band structure. The last part of the chapter introduces Ge/$Si_{1-x}Ge_x$ MQWs featuring Ge-rich barriers. We will discuss low temperature band alignment as obtained through tight binding calculation and we will present low temperature PL measurements performed on three samples with different well thickness. Finally, the electron lifetime as a function of temperature will be derived for all investigated systems.

## 2.1 SiGe Alloys

Si and Ge are fully miscible. $Si_{1-x}Ge_x$ alloys exhibit a diamond crystalline structure in which the Ge fraction $x$ ranges from 0 to 1. The lattice constant $a$ of these solid solutions varies from the one of pure Si ($a_{Si} = 0.54nm$) to that of pure Ge ($a_{Ge} = 0.56nm$). The linear dependence of the alloy lattice constant is well described, to a first approximation, by the empirical Vegard's

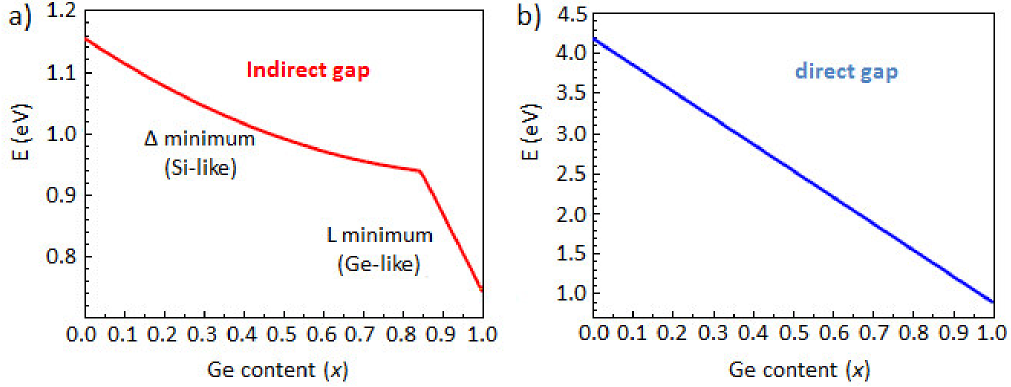


Figure 2.1: Indirect (a) and direct (b) bandgap of $Si_{1-x}Ge_x$ alloys as a function of Ge molar fraction (x) [62].

law [61]:

$$a_x = a_{Si}(1-x) + a_{Ge}x = a_{Si} + x\Delta a. \tag{2.1}$$

SiGe alloys (like Si and Ge) are indirect-gap semiconductors for all the Ge concentrations. As shown in Figure 2.1, for x lower than 85%, the CB absolute minimum lies in the Δ valley (Si-like), while for a larger Ge content it is at the L valley (Ge-like) [62].

## 2.2 Heterostructures and Strain

The samples investigated in this thesis consist of $Si_{1-x}Ge_x$ alloys (epilayers) pseudomorphically grown on a $Si_{1-y}Ge_y$/Si substrate. The epilayer rearranges its lattice constant and the crystallographic orientation to that of the substrate, in order to minimize its energy.

The lattice misfit ($f$) between the epilayer and the substrate can be written as:

$$f = \frac{a_s - a_0}{a_0}, \tag{2.2}$$

where $a_s$ and $a_0$ are the lattice constants of the epilayer and of the relaxed substrate, respectively.

When a $Si_{1-x}Ge_x$ layer is deposited on a $Si_{1-y}Ge_y$ substrate, it experiences a biaxial strain, which is compressive in the growth ($xy$) plane and tensile in

the growth ($z$) direction if x > y, while the opposite is true when x < y.

In general, strain can be well-described by a rank-3 tensor. For simplicity, let us call $\epsilon_{\|}$ the strain component in the plane parallel to the interface ($\epsilon_{\|} = \epsilon_{xx} = \epsilon_{yy} = f$), and $\epsilon_{\perp}$ the strain component along the growth direction. This description turns out to be very useful, since it allows us to resolve the total strain into two components. The uniaxial component is expressed by [63]:

$$\epsilon_t = \epsilon_{\perp} - \epsilon_{\|}, \tag{2.3}$$

and it is responsible for the splitting of degenerate levels such as, for example, HH and LH states at the VB top. Moreover the isotropic hydrostatic component given by the trace of the tensor $\epsilon$ can be written as:

$$\epsilon_h = Tr(\epsilon) = \epsilon_{xx} + \epsilon_{yy} + \epsilon_{zz}, \tag{2.4}$$

and it induces a shift of the conduction and valence band levels, yielding a variation of the energy gap. In particular, in the case of Ge, both the direct and the indirect bandgaps decrease as a tensile strain is applied [59, 64], while they increase in the compressive case. The effects of the two strain components on a $Si_{1-x}Ge_x$ layer with x > 85% for both the tensile (a) and the compressive (a) case are shown in Figure 2.2.

However, the pseudomorphic growth of an epilayer on a substrate with different lattice constant can not proceed indefinitely, since elastic energy is stored in the deformed layer. As a consequence, the system might relieve the strain by reducing its free energy through the introduction of structural defects, named dislocations [65]. The formation of dislocations requires itself some nucleation energy. As a result there is a film thickness, called *critical thickness*, beyond which the introduction of such defects becomes more favourable [66]. In general, dislocations lie along the lowest energy crystallographic directions and, in the case of SiGe heterostructures [67, 68]: *Misfit dislocations* (MD) run along $\langle 110 \rangle$ and $\langle \bar{1}10 \rangle$ directions, whilst *threading dislocations* (TD) pierce through the epilayer towards the free surfaces. A detailed discussion about dislocation formation and structure is provided in Ref. [69].

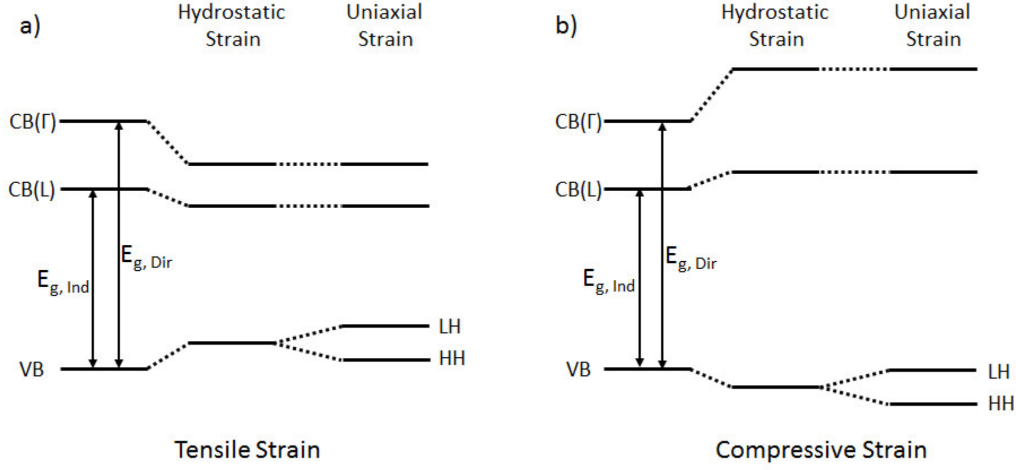


Figure 2.2: Effect of tensile (a) and compressive (b) strain on a $Si_{0.15}Ge_{0.85}$ alloy. Effects of the hydrostatic and uniaxial strain are shown separately.

Dislocations are defects that perturb the periodicity of the lattice. In particular, they introduce electronic levels within the band gap, thus affecting optical and electronic properties of the material. To limit dislocations formation, *graded virtual substrates* (GVS) have been introduced [70, 71, 72]. A GVS consists of a buffer layer (*graded layer*) whose composition, and thus, lattice constant, linearly varies from the substrate to the desired alloy composition. In SiGe alloys, GVS are films whose Ge content linearly increases from 0 (pure Si) to the final Ge molar fraction (x). As a consequence, the lattice misfit varies linearly in the graded layer, so that the dislocation interaction is strongly reduced and the density of TDs is lowered by $2-3$ orders of magnitude with respect to that of single heterostructures directly grown on Si. It has been demonstrated that the introduction of GVSs in microelectronic devices allows a significant increase (1 order of magnitude) of the electron mobility in SiGe quantum wells (QWs) [70].

## 2.3 Quantum Wells

We now focus on SiGe-based quantum wells (QWs) heterostructures, whose electronic structure, optical and spin properties will be investigated in detail

in the following chapters of this thesis. QWs systems have attracted a great interest in the scientific community during the last decade, since they offer the possibility to localize carriers and, thus, to increase the radiative transitions efficiency [73]. QWs are two-dimensional heterostructures in which electrons and holes are spatially confined in a region characterized by a thickness comparable with their de Broglie-wavelength. Carrier confinement is achieved by embedding a nanometric layer of a semiconductor (well) into a matrix of a semiconductor with an higher gap (barrier).

The way in which the top of the VB and the bottom of the CB align with respect to each other is crucial. In SiGe alloys, two types of band alignment are possible: the type I and the type II, as schematically shown in Figure 2.3 (a) and (b), respectively. In type I QWs, the VB top of the well is higher in energy than the VB top of the barrier, while the CB bottom is lower (Figure 2.3(a)). On the other hand, in type II QWs, the CB and VB bands of the well are below (above) the corresponding bands in the barriers. In a type I band alignment, both electrons and holes are confined within the same region, whilst in the type II, only electrons or holes are confined within the well region. For this reason, nanostructures with type I band alignment are more interesting from the point of view of optoelectronic applications, since a great overlap of the wavefunctions is caused by the spatial confinement of both types of carriers, thus exhibiting an increased absorption and recombination efficiency with respect to the type II [73].

## 2.4 Band Alignment and Band Structure

In this section we will introduce details about composition and band alignment of Ge/$Si_{1-x}Ge_x$ MQWs focusing on the case of Ge QWs embedded in SiGe barriers whose nominal Ge fraction is $x = 85\%$. Samples were grown by the group of Prof. G. Isella at the L-NESS centre of Como (Italy) via low-energy plasma-enhanced chemical vapor deposition (LEPCVD), an epitaxial growth technique based on a chemical deposition process, enhanced and activated via a high-intensity and low-energy plasma [74]. LEPCVD is characterized by a very high growth rate, that can reach 10 nm/s, and

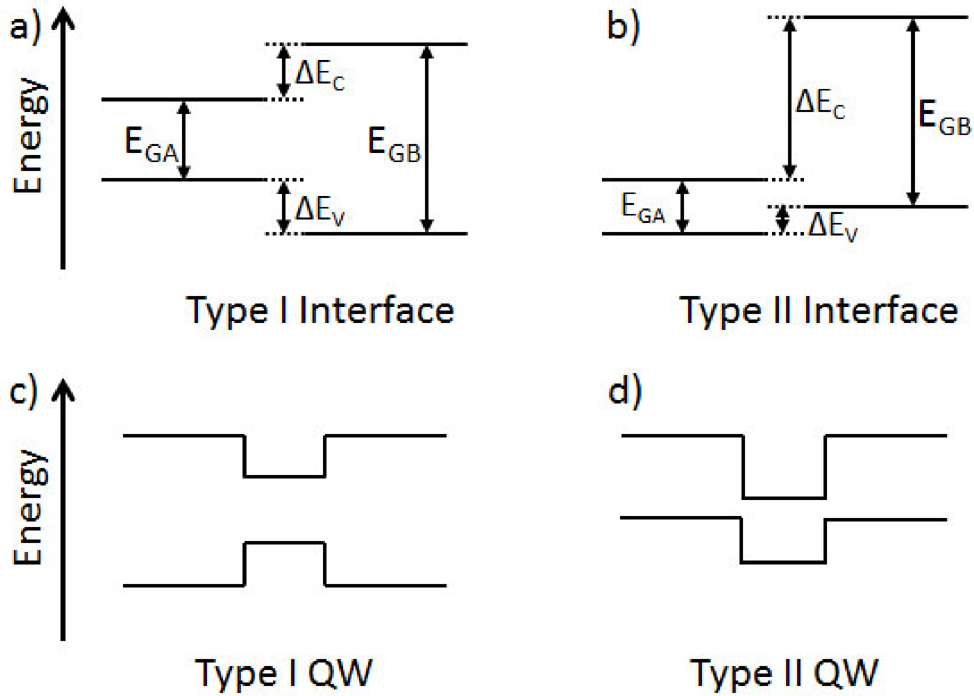


Figure 2.3: Sketch of type I (a) and type II (b) band alignment. Band structure of type I (c) and type II (d) quantum wells.

which can be exploited for the epitaxial growth of Ge-rich SiGe alloy buffer layers on Si. For a further reading about LEPCVD technique on Si see Refs. [74, 75, 76]. All the samples analysed in this and in the following chapters are characterized by the same general structure, which is schematically shown in Figure 2.4. A 13 $\mu$m thick GVS, whose Ge composition varies from 0% to 90%, is deposited on a (001)-oriented Si substrate. The GVS in then capped with a 2 $\mu$m thick $Si_{0.10}Ge_{0.90}$ relaxed layer. The total thickness of this buffer layer is of about 15 $\mu$m and it constitutes the relaxed substrate upon which strained-compensated quantum wells and barrier are grown. The active part of the structure consists of 200 Ge QWs separated by $Si_{0.15}Ge_{0.85}$ barriers deposited on the fully relaxed VS. Finally, for a 40 nm $Si_{0.10}Ge_{0.90}$ layer and a $\sim$ 10 nm Si cap are grown on the top of the system.

Due to the dependence of SiGe lattice parameters on composition, the thickness of the layers was designed to balance the compressive strain in the

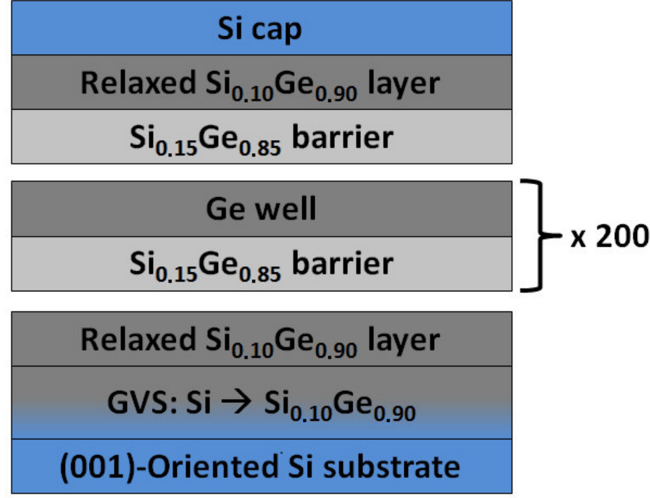


Figure 2.4: Sketch of the structure of the Ge/$Si_{1-x}Ge_x$ Multiple Quantum Wells samples investigated in this thesis.

well region and the tensile strain in the barrier region. For this reason the average lattice constant of the well and barrier layers is chosen equal to that of the relaxed $Si_{0.10}Ge_{0.90}$ layer at the top of the GVS. The composition and the thickness of wells and barriers, respectively, satisfy the following relation:

$$a_S = \frac{d_W \cdot a_W + d_B \cdot a_B}{d_W + d_B}, \tag{2.5}$$

where $d$ is the layer thickness, $a$ is the lattice constant, while $W$, $B$ and $S$ refer to well, barrier and substrate, respectively.

Due to the inhomogeneities in the plasma intensity within the LEPECVD reactor, the growth rate is non-uniform across the Si wafer surface. As a consequence, samples with different barrier and well thickness, but equal alloy composition, are available from a single wafer. In this thesis, samples with a well thickness ($L_Z$) ranging from 3.8 nm to 22.6 nm have been investigated. The list of Ge/$Si_{1-x}Ge_x$ MQWs samples is provided in Table 2.1. The thickness of wells and barriers were obtained by means of X-Ray diffraction measurements, performed at L-NESS centre of Como by Dr. Danny Chrastina.

The low temperature band alignment of Ge/$Si_{0.15}Ge_{0.85}$ QWs grown on

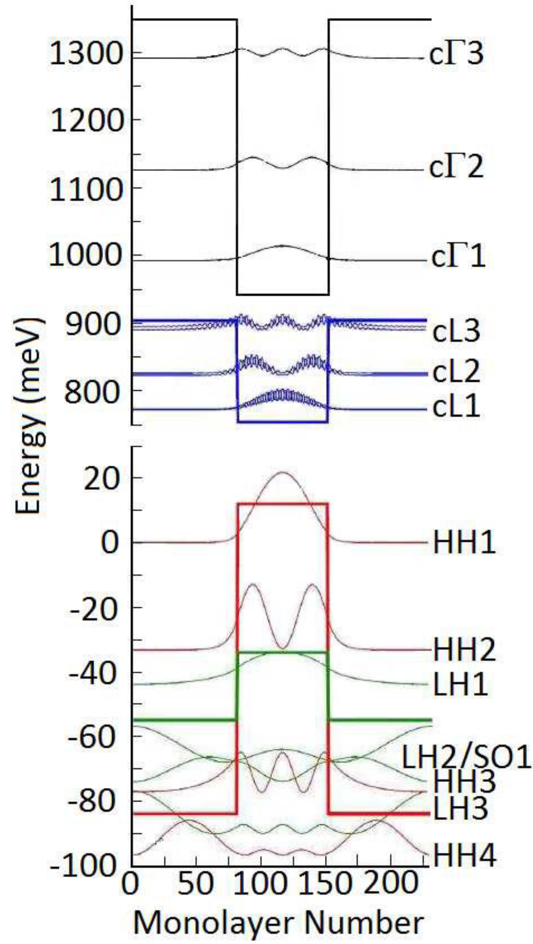


Figure 2.5: Calculated band offsets and square modulus of the wavefunctions of electron and hole confined states in a (001)-oriented Ge/$Si_{0.15}Ge_{0.85}$ QW having a 10 nm thickness [19].

$Si_{0.10}Ge_{0.90}$ VS has been obtained by M. Virgilio and G. Grosso through tight binding calculation in Ref. [19], who predicted a type I band alignment for both the fundamental indirect- and the direct-gaps. A schematic representation of the energetic levels and the square modulus of the wavefunctions, obtained from the tight binding calculation for a 10 nm thick Ge QW with 23 nm thick $Si_{0.15}Ge_{0.85}$ barriers, are reported in Figure 2.5.

The band offset for the L minimum is about 150 meV, while for the Γ valley conduction minimum it is about 400 meV. L and Γ conduction levels are labeled by 'cLn' and 'cΓn', respectively, while 'HHn', 'LHn' and 'SOn'

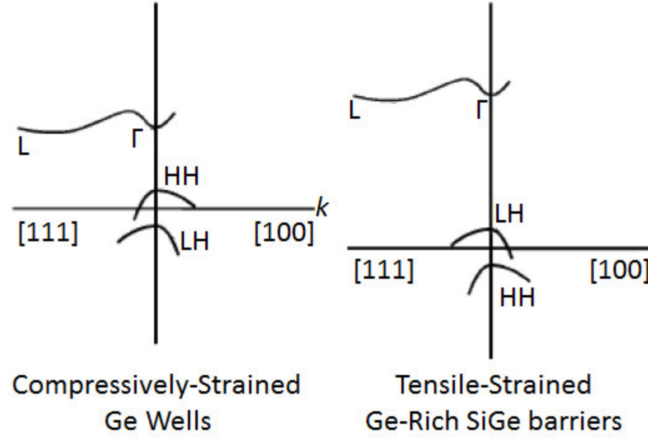


Figure 2.6: Sketch of the band structure of (001)-oriented compressivley-strained Ge wells (a) and tensile-strained barriers (b) [77].

Table 2.1: Characteristics of analysed samples.

| Sample | Well thickness (nm) | Barrier thickness (nm) | Dep. rate (nm/s) |
|---|---|---|---|
| 7864-1 | $3.8 \pm 0.5$ | 7.7 | 0.3 |
| 7864-6 | $10 \pm 1$ | 18.6 | 0.3 |
| 7909-11 | $22.6 \pm 1$ | 27.3 | $4 - 6$ |

indicate heavy holes, light holes and split-off confined states. It is worth noticing that since the Ge well layer experiences a compressive strain, while $Si_{0.15}Ge_{0.85}$ barriers are slightly under a tensile strain, the HH and LH levels in the well and in the barrier layers are not degenerate and there is a character inversion between the top of the VB in well and barrier regions (Figure 2.6). The band offset for the HH states (red line of Figure 2.5) is $\sim 100$ meV and for the LH states (green line of Figure 2.5) it is of $\sim 20$ meV. Finally, it should be noted that the $n = 1$ states wavefunctions are almost completely confined within the well region while, as $n$ increases, also the wafefunction penetration within the barrier region is larger, so that carriers confinement decreases.

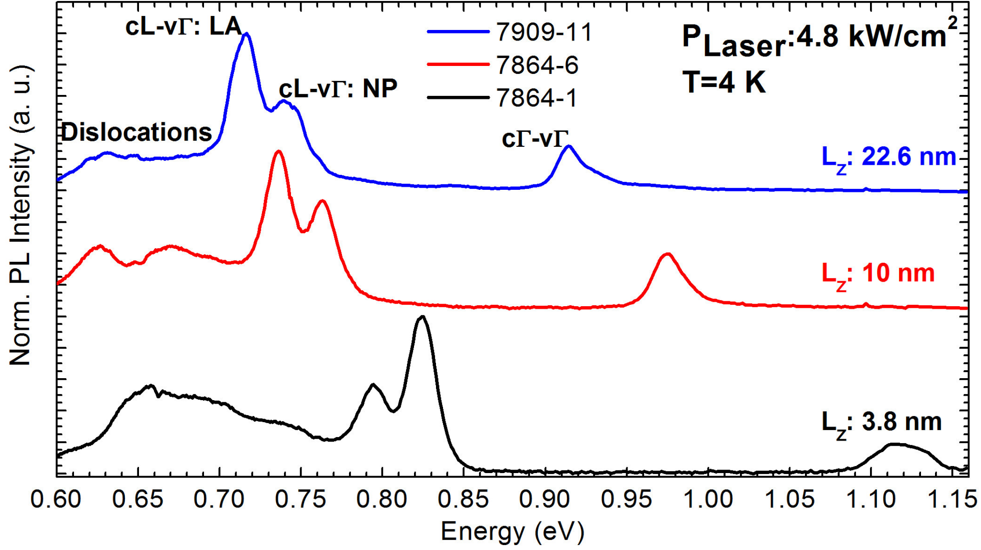


Figure 2.7: Low temperature CWPL spectra obtained from $Ge/Si_{1-x}Ge_x$ MQWs samples reported in Table 2.1 under 1.165 eV laser excitation.

Table 2.2: PL peak positions relatives to excitonic transitions of analysed samples (see Figure 2.7).

| $L_Z$ | $cL - v\Gamma : LA$ (eV) | $cL - v\Gamma : NP$ (eV) | $c\Gamma - v\Gamma$ (eV) |
|---|---|---|---|
| 3.8 | 0.795 | 0.825 | 1.097 |
| 10 | 0.737 | 0.763 | 0.976 |
| 22.6 | 0.716 | 0.739 | 0.914 |

## 2.5 Optical Properties

In this section we will discuss the optical properties of the $Ge/Si_{1-x}Ge_x$ MQWs heterostructures grown on (001)-oriented Si substrate (see Table 2.1). The T = 4 K PL spectra of the samples are shown in Figure 2.7. Samples were excited by means of a $Nd:YVO_4$ laser, characterized by a 1.165 eV emission energy and operating at a power density of 4.8 $kW/cm^2$ (for complete information about the experimental set-up see Appendix A.1, Line B). The PL spectra can be divided into three main regions [19].

The broad PL bands in the 0.6-0.75 eV energy range can be attributed to transitions related to defects, mainly dislocations (see Section 2.2).

At higher energies, all the samples exhibit two distinguishable features. The one at lower energy has to be ascribed to the longitudinal acoustic (LA) phonon-assisted transition ($cL - v\Gamma$ : LA), while the one at higher energies is attributed to the zero-phonon line of the indirect cL1-HH1 transition between the first confined CB state at L (cL1) and the HH1 VB state ($cL - v\Gamma$ : NP). The observation of the NP line in $Ge/Si_{1-x}Ge_x$ QWs is attributed to the roughness of the interface between the QWs and the barriers. Indeed, irregularities of the interfaces can act as scattering centres for excitons, providing to the electrons in the L states the required momentum to recombine with holes at $\Gamma$ [62, 78]. Moreover, excitons can be confined in lower potential regions due to the QW width fluctuations, thus providing a delocalization of electrons and holes in the $k$-space [79], which results in a non-zero probability to observe the no-phonon line emission [80].

Finally, the PL peaks at highest energies stem from the direct-gap emission ($c\Gamma - v\Gamma$). The $c\Gamma - v\Gamma$ line emission of samples with $L_z$ equal to 10 nm and 22.6 nm (red and blue lines of Figure 2.7) have the characteristics of the Ge direct-gap emission, whose asymmetrical shape has been fully explained in Section 1.2. On the other hand, the broad feature that can be appreciated in the PL spectrum of the sample with $L_z = 3.8$ nm (black line in Figure 2.7) suggests that, besides the direct-gap emission, other transitions provide contributions to the PL in the 1.08-1.15 eV range. Low temperature PL measurements performed by changing the excitation energy (not shown in this thesis), reveal that at 1.165 eV and at T=4 K, the direct-gap PL peak is superimposed to the electronic Raman scattering (ERS) feature [81], which has already been reported both in bulk Ge [38, 82, 83, 84] and in very similar $Ge/Si_{1-x}Ge_x$ MQWs heterostrucures [85]. The energy position of the direct-gap emission for 7864-1 sample reported in table 2.7 was found considering a measurement with 1.233 eV excitation energy.

Looking at Figure 2.7 it is worth to emphasize that both direct and indirect transitions are clearly distinguishable in the same PL spectra, differently from the bulk Ge case (Figure 1.2). This is due to the following reasons. First of all, in a type I band alignment, both electrons and holes lie within the well region. Moreover, the higher recombination rate for the direct-gap allows us

to well resolve the $c\Gamma - v\Gamma$ transition even if the carriers dynamics favors the population of L-type states. Finally, it is well known that the electron lifetime within the $\Gamma$-valley CB is limited by the intervalley scattering mechanism, thus lying in the hundreds of fs regime [34, 35, 36], while nonradiative recombination processes have a characteristic lifetime lying in the tens of ns regime [86]. For this reason, in Ge-based systems, the dislocations affect the indirect-gap recombination, whose lifetime is expected to lie in the $\mu$s regime [39], while they do not play any role in the direct-gap transition.

The energy peak positions of all features observed in Figure 2.7 are reported in Table 2.2. It is worth emphasizing that, as the QW thickness decreases, the energy distance between the $cL - v\Gamma$ and the $c\Gamma - v\Gamma$ transitions increases, since L states are less sensitive to the changes in the QW width with respect to the $\Gamma$ states [19]. Moreover, the indirect-gap PL redshifts by about 80 meV as the well thickness increases from 3.8 nm to 22.6 nm, approaching the peak position of bulk Ge (as an example, see Figure 1.2 in Chapter 1). This fact is due to the decreasing quantum confinement of the photoexcited carriers. A detailed discussion about these observations can be found in Ref. [19].

## 2.6 Decay Time

In this section we will discuss the electron lifetime ($\tau_{\mathrm{L}}$) dependence on the well thickness and on temperature for all the samples described in Table 2.1.

The decay curves reported in this section were probed by means of time-resolved PL (TRPL) measurements. Excitation was performed using an optical parametric oscillator pumped by a tunable mode-locked Ti:Sa laser with a pulse duration of about 1 ps, resulting in a peak power density[1] of about 30 kW/cm$^2$. The excitation energy was set equal to 1.165 eV. The PL was filtered through long pass (LP) and band pass (BP) filters, whose spectral window was chosen according to the specific emission of the sample. The PL was probed by a fiber-coupled superconducting nanowire single photon de-

[1]In the following, all power densities values of pulsed lasers will refer to the peak power density. For more details see Appendix A.2.2.

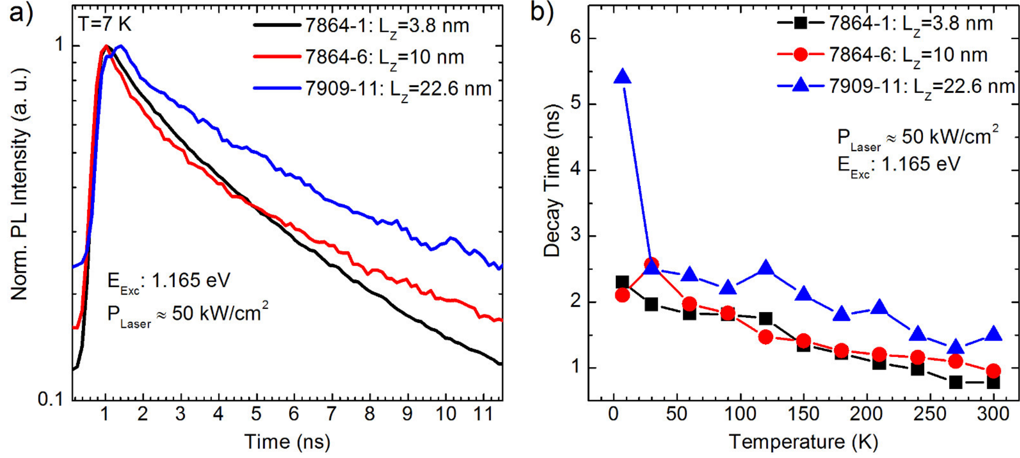


Figure 2.8: (a): Low temperature decay curves obtained from the $Ge/Si_{1-x}Ge_x$ MQWs samples reported in Table 2.1. (b): Electron lifetimes values in the 7-300 K temperature regime obtained via stretched exponential decay fits of the temperature dependent PL decay time.

tector. A full description of the experimental set-up is provided in Appendix A.2.1.

The decay curves obtained from the samples with $L_Z$ = 3.8 nm (black curve), $L_Z$ = 10 nm (red curve) and $L_Z$ = 22.6 nm (blue curve) are shown in Figure 2.8 (a). It is worth noticing that the PL decays do not exhibit a single exponential-like decay, thus suggesting a distribution of recombination lifetimes. A similar behaviour was already found in literature in disordered systems such as porous and glassy Ge quantum dots [87, 88, 89, 90]. This behaviour was considered as a consequence of the dispersive diffusion of photoexcited carriers, and it has been modeled by a "stretched-exponential" law:

$$I_t = I_0 \cdot exp[-(t/\tau)^{\beta}], \tag{2.6}$$

where $\tau$ is a mean lifetime and $\beta$ a non-exponential factor taking into account the broad lifetime distribution. In our case, fits performed using equation 2.6 (not shown) revealed a mean $\tau_L$ some ns lower than that found in Ref. [80], in which a single-exponential decay behavior was found on the same $Ge/Si_{1-x}Ge_x$ MQWs samples. This difference is however not completely surprising and it can be ascribed to the fact that the measurements reported

in Ref. [80] were carried out using an experimental set-up very similar to that described in Appendix A.2.2, characterized by a laser pulse duration of about 15 ns at a repetition rate of 10 KHz, and, thus, by a resolution of about 8 ns. On the other hand, the experimental set-up used here can be used to investigate the dynamics of photoexcited carriers on a timescale shorter than that used in measurements reported in Ref. [80]. In this time range, our findings seem to suggest that the carrier dynamics is strongly affected by small local fluctuations of the nanostructure size, which was suggested to cause a broad distribution of the recombination lifetime [87] and which finally leads to a mean $\tau_L$ reduction.

Looking at the decay curves obtained at T=7 K (Figure 2.8 (a)), it is evident that it is not possible to find a clear relationship between the decay time and the well thickness. However, looking at the electron lifetime dependence on temperature obtained by means of stretched-exponential curve fits in Figure 2.8 (b), a common trend is observed for all the samples. In particular, $\tau_L$ monotonously decreases as the temperature increases. This behavior has already been observed on these heterostructures, and it has been explained as the consequence of various intrinsic and extrinsic effects (Ref. [80]). First of all the enhancement of non radiative recombination channels, reducing the electron lifetime in the high temperature regime, has to be considered. Moreover, increasing the lattice temperature, the phonon population is enhanced. Therefore phonon-assisted recombinations become more likely and a $\tau_L$ reduction occurs. Furthermore, also the exciton mobility has to be taken into account. Indeed, it is expected to be enhanced due to the increase of the exciton thermal energy so that it becomes more likely for the exciton to recombine at defects. As a consequence, the exciton lifetimes are expected to decrease [80]. Such an effect has already been described for GaAs/AlGaAs QWs [91]. It is finally worth underlining that also the thermally activated exciton escape into the barriers region was proposed in literature to explain the decay time reduction in GaAs/AlGaAs and in InGaAs/GaAs QWs as T rises [92, 93]. However, in both cases, the band offset of a few meV is easily overcomed thanks to the thermal energy. However in our $Ge/Si_{1-x}Ge_x$ MQWs this phenomenon can be excluded since the offset values are higher,

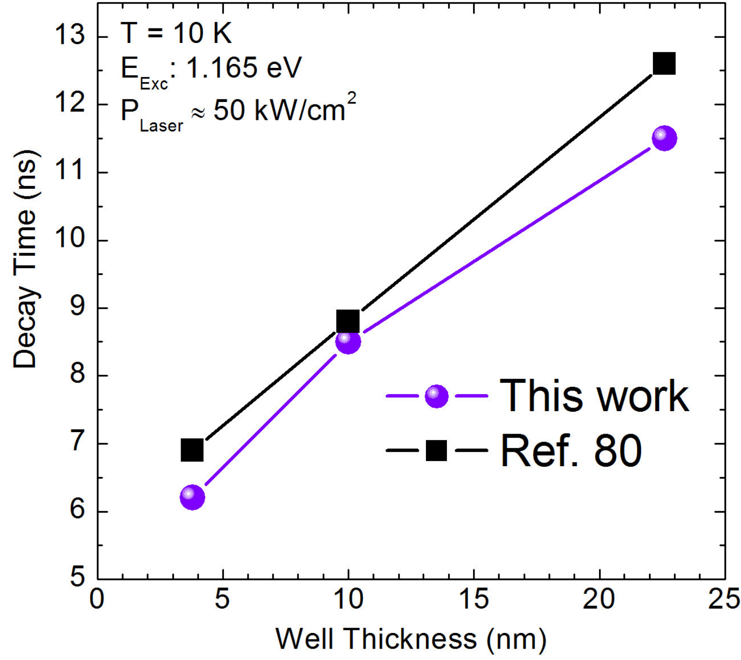


Figure 2.9: (a): Low temperature values of the electron lifetime as a function of the well thickness. Violet circles refer to experimental data of this thesis work and were obtained by decreasing mono-exponential fits performed on the long tail of the decay curves reported in Figure 2.8. Black squares values were evaluated from data of Ref. [80].

as elucidated in Figure 2.5.

In order to provide additional details about the electron lifetime dependence on the well thickness, in the following we will consider the second part of the decay curves, which is well described by a mono-exponential curve and which allow us to compare our data with those of Ref. [80].

Electron lifetimes obtained by fitting the long time tail of the decay curves in Figure 2.8(a) by means of single exponential decay curves are shown in Figure 2.9 (violet full dots) together with $\tau_{\mathrm{L}}$ values obtained from TRPL data extracted from Ref. [80] (black empty squares). It is worth noticing that, on this time scale, data are in very good agreement, and a clear electron lifetime dependence on the well thickness is exhibited.

In particular, Figure 2.9 points out that the $\tau_{\mathrm{L}}$ increases as the QWs thickness increases. Such a behavior has already been reported for both III-

V compounds [73, 91, 94] and SiGe/Si QWs [79], and it was attributed to the dependence of the exciton binding energy on QW thickness. Indeed, the exciton binding energy increases as the QW thickness is reduced [95], thus enhancing the transition probability and giving rise to an electron lifetime reduction [73, 80, 91, 94].

Also the interface roughness has to be taken into account, because it has been shown to play an important role in the no-phonon line emission (Section 2.5). As $L_Z$ decreases, the role of interface roughness becomes more relevant [96] and, thus, the no-phonon emission favored by exciton scattering [78] and exciton localization at the minima of the spatially fluctuating potential becomes more probable, and the electron lifetime is expected to decrease.

Finally, also the overlap of the electron and hole wavefunctions depends on the the well thickness ($L_Z$), thus contributing to the decay time dependence on $L_Z$. It has been shown [79] that, when $L_Z$ is lower than a critical value, the wavefunction overlap is expected to decrease, due to the wavefunction penetration into the barrier region, and thus the decay time is expected to rise. In Ref. [79] a critical value of $L_Z = 4$ nm was found in Si/GeSi MQWs. In our $Ge/Si_{1-x}Ge_x$ MQWs, however, no increase of the decay time is observed at that value of $L_Z$. This is probably due to the fact that the critical value of our systems is lower than the minimum $L_Z$ considered (i. e. 3.8 nm). This finding is compatible with the offset of these heterostructures, which are higher than those of SiGe/Si QWs systems (Figure 2.5).

In conclusion, the results discussed in this section are in good agreement with those reported by Giorgioni *et al.* in Ref. [80]. Considering the different accessible time scale we have shown that, as concerns the long tail of the decay curve, our $\tau_L$ values do not differ appreciably with respect to those reported in that work, thus confirming the good reproducibility of the TRPL data [80].

# Chapter 3

# (001)-Ge/SiGe MQWs: Spin Properties

This chapter is devoted to the spin properties of the (001)-oriented Ge/$Si_{1-x}Ge_x$ MQWs heterostructures. At first, we will discuss the importance of the energy relaxation of L-valley electrons in determining the spin relaxation time, then we will focus on the $\tau_S$ dependence both on the well thickness and on temperature. Finally, we will show the first experimental $g$-factor investigation on CB electrons obtained via quantum beat spectroscopy in group-IV semiconductors.

## 3.1 Spin Relaxation of L-Valley Electrons

In recent years, the spin relaxation of conduction electrons in Ge [97, 98], has been widely discussed from the theoretical point of view [22, 21]. These works demonstrate that both intervalley and intravalley electron scattering provide an important contribution to the spin relaxation in the multivalley CB of Ge. In particular, the theory shows that spin relaxation is governed by the intervalley electron-phonon scattering in a wide temperature range ($T>30$ K) [21], while at $T<20$ K the population of the X point phonon modes is negligible and, thus, the intravalley spin relaxation rate exceeds the intervalley one [22].

The role of intervalley spin relaxation of conduction electrons, together with the possibility to suppress this spin relaxation channel by applying strain along a proper direction, will be discussed in detail in Chapter 4. Here we provide experimental evidence for the importance of energy relaxation of L-valley CB electrons. To address this issue we will show PL measurements of the indirect-gap transition performed by varying the excitation energy (PLE) and polarization resolved TRPL measurement, which allow us to directly measure the spin relaxation time ($\tau_{\mathrm{S}}$). All the experimental data reported in the following refer to a (001)-oriented Ge/$\mathrm{Si_{1-x}Ge_x}$ MQWs sample with a well thickness of 3.8 nm, named 7864-1 (see Table 2.1).

The T=7 K polarization degree ($\rho$) obtained from the NP transition in the 0.972-1.240 eV excitation energy range is shown in Figure 3.1(a). PLE measurements were carried out by using an experimental set-up very similar to that described in Appendix A.1, Section "Line A". However, in this case, an optical parametric oscillator pumped by a mode-locked Ti:Sa laser working at a repetition rate of 80 MHz was used to tune the laser excitation energy, while a dispersive monochromator equipped with an InGaAs array characterized by an energy cut-off at 0.785 eV was used to measure the PL. The laser excitation was right-handed ($\sigma^{+}$) circularly polarized, so that co(counter)-circular PL emission will be indicated by a positive (negative) value of $\rho$. Looking at the spectrum, it is worth noticing that the $\mathrm{cL-v\Gamma}$ emission is co-polarized with respect to the excitation for all the excitation energies. A co-polarized indirect-gap feature at 1.165 eV energy excitation was similarly reported in the literature for similar Ge/$\mathrm{Si_{1-x}Ge_x}$ MQWs heterostructures [13].

The data reported in Figure 3.1(a), clearly point out a non-zero circular polarization, thus suggesting the successful optical spin orientation of L-valley electrons. Moreover, $\rho$ is non-constant over the investigated energy range. In particular, starting from low excitation energy values, we can see that the degree of circular polarization monotonously increases up to $\sim 23\%$, for an excitation energy ($\mathrm{E_{Exc.}}$) of 1.116 eV. Then, when the excitation energy exceeds this value, it starts decreasing until $E_{Exc} = 1.158$ eV ($\rho \sim 7\%$), from where it remains constant. The comprehension of the $\rho$ behaviour as a

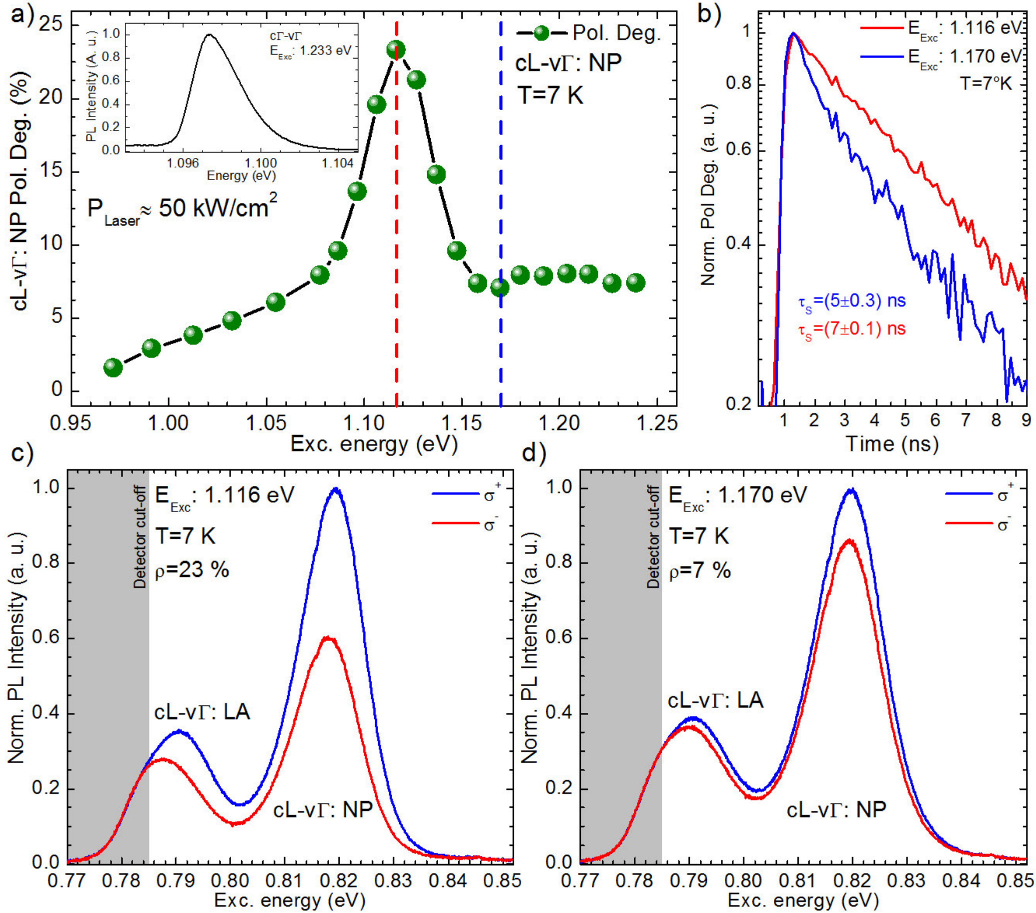


Figure 3.1: Upper panel. (a): Polarization degree obtained from the indirect $\mathrm{cL}-\mathrm{v}\Gamma$: NP transition of the 7864-1 sample (Table 2.1) at T=7 K in the 0.972-1.240 eV excitation energy range. The excitation energy of 1.117(1.170) eV is labelled by the red(blue) dashed line. In the inset the direct-gap PL spectrum of the same sample is reported. (b): Low temperature decays of the degree of circular polarization of sample 7864-1 obtained under 1.117 eV (red line) and 1.165 eV (blue line) laser excitation. Corresponding spin relaxation lifetimes values are indicated in the graph. Lower panel. Low temperature polarization-resolved PL spectra obtained at excitation at 1.116 eV (c) and 1.170 eV (d), respectively. Grey boxes indicate the cut-off energies of the detector.

function of $E_{Exc}$ is still under scrutiny, and we hope that our experimental findings can possibly stimulate further theoretical investigations of the physical mechanisms regulating $\Gamma - L$ spin transfer and the subsequent dynamics of L-valley electrons.

In this work, we focus mainly on the 1.116 eV and 1.170 eV laser excitation energies (blue and red dashed lines in Figure 3.1(a)). In the case of the excitation energy at 1.116 eV, the circular polarization degree of the indirect-gap NP[1] transition is about 3 times higher ($\rho = 23\%$) than that obtained by exciting at 1.170 eV as elucidated by the lower panel of Figure 3.1. To understand this behaviour we have to refer to the PL spectrum reported in the inset of Figure 3.1(a), which shows the direct-gap PL spectrum obtained at $E_{Exc} = 1.233$ eV[2]. If we consider that the PL peak is affected by a Stokes shift of about 11 meV[3], as already found on very similar $Ge/Si_{1-x}Ge_x$ MQWs heterostructures [19], the excitation energy at which we obtain the maximum value of $\rho$ is very close to the direct-gap absorption edge. Thus, in this case, photoexcitation promotes electrons directly to the edge of the $\Gamma$ minimum. These electrons reach the L-valley absolute minimum after having suffered the $\Gamma - \text{to} - L$ transfer. Notably they have to relax less excess energy than carriers excited by the laser at 1.170 eV. Under such condition, the PL emission exhibits a higher polarization. This finding seems to confirm the important role played by the thermalization process in determining the spin relaxation of L-valley electrons.

We also performed polarization-resolved TRPL measurements, which allows us to directly gather information about the spin relaxation time. By measuring the $\sigma^+$ and $\sigma^-$ polarized PL decay, it is possible to derive the decay curve related to the degree of circular polarization. This provides direct access to $\tau_S$. Polarization-resolved TRPL measurement were performed by exciting the sample with a Ti:Sa laser coupled to an optical parametric oscil-

[1] LA transition energy falls near the detector cut-off, thus no conclusive results can be drawn.

[2] This excitation energy was suitably chosen in order to avoid the superposition between the direct-gap transition and the ERS, as in the case of $\lambda_{Exc} = 1.165$ eV (see Figure 2.7).

[3] The Stokes shift is the energy difference between the absorption peak and the PL peak, and it is mainly attributed to QW width fluctuation [99].

lator, characterized by a pulse with a temporal width of about 1 ps. The PL signal was measured by means of a fiber coupled superconducting nanowire single photon detector (SNSPD) working in the 800-2000 nm range. The experimental set-up is described in detail in Appendix A.2.1.

The T=7 K decays of the circular polarization obtained from the polarization - resolved TRPL measurements of the 7864-1 sample are reported in Figure 3.1(b). The red curve refers to an excitation energy of 1.117 eV, while the blue curve refers to an excitation energy of 1.165 eV. In both cases, the non-zero value of $\rho$ demonstrates a net circular polarization of the PL emission. Exponential fits performed on both decay curves provide a $\tau_S$ of about 7 ns in the former case, while a $\tau_S$ of about 5 ns is measured in the latter. In light of the signal-to-noise ratio, the measured $\tau_S$ difference is small but significant. These findings are in very good agreement with the physical picture we suggested above. Indeed, in both cases, carriers are photoexcited within the $\Gamma$ valley CB but, for an excitation energy of 1.117 eV, they possess less excess energy with respect to the valley bottom than for 1.165 eV and, thus, they are 50 meV closer to the L-valley edge. The difference between the measured spin relaxation times once again reveals that the thermalization process represents a spin relaxation source, as suggested by PLE measurements shown in the first part of this section.

## 3.2 Low Temperature Spin Lifetime

In the previous section we discussed the excitation energy dependence of $\tau_S$ and the role played by the $\Gamma$-L spin transfer. In this section, we will discuss the dependence of the spin relaxation time on the well thickness. Polarization-resolved TRPL measurements were performed at cryogenic temperature on the three samples reported in table 2.1, named 7864-1, 7864-6 and 7909-11, which are characterized by a well thickness of 3.8 nm, 10 nm and 22.6 nm, respectively. The experimental set-up used here is identical to that described in Section 3.1, and it is fully described in Appendix A.2.2. In

this case, the excitation energy was kept fixed at 1.165 eV[4].

The low temperature polarization-resolved TRPL decay curves of the three samples are shown in the upper panels of Figure 3.2. The different intensities of the two helicity-resolved PL components reveal a non-zero circular polarization of the emission as already found in the previous Section.

Figure 3.2(d) shows the normalized decay curves obtained for the sample with 3.8 nm (black curves), 10 nm (red curve) and 22.6 nm (blue curve) well thickness. The derived electron spin lifetime as a function of the well width is reported in Figure 3.2(e). These measurements allowed us to reveal that the spin lifetime is in the 5-20 ns range and no clear $\tau_S$ dependence on the QW thickness.

Spin relaxation times obtained in this thesis on (001)-oriented $Ge/Si_{1-x}Ge_x$ MQWs heterostructures are about an order of magnitude shorter than those reported in previous experimental works dealing with bulk Ge [39, 100]. It is worth noticing that, in these works, the role of the spin flipping caused by the electron-hole exchange interaction, suggested to cause a strong $\tau_S$ suppression in quantum confined systems [101, 102, 27], is neglected. Indeed, in a recent work, Giorgioni *et al.* [27] demonstrated a monotonic dependence of $\tau_S$ on the excitation power density in Ge-based QWs, revealing that, by increasing the pump power density, $\tau_S$ is shortened. Such finding manifests the crucial role played by the electron-hole exchange interaction in the determination of the spin lifetime.

Figure 3.3 reports the dependence of the spin lifetime as a function of the inverse pulse excitation power density. Data of Ref [27] (blue squares) for a 20 nm thick QW are reported together with those obtained in this work for the 7909-11 sample (red circle). In both cases, the experimental $\tau_S$ values were obtained by means polarization- and time-resolved PL measurements at 1.165 eV on $Ge/Si_{0.15}Ge_{0.85}$ MQWs heterostructures with very similar composition and a well width of about 20 nm. Giorgioni *et al.* [27] carried out measurements by using the experimental set-up described in Appendix

[4]Indeed, since experimental limits did not allow us to excite 7864-6 and 7909-11 samples in resonance with their direct-gap absorption, we prefer to measure all the heterostructures under the same experimental conditions.

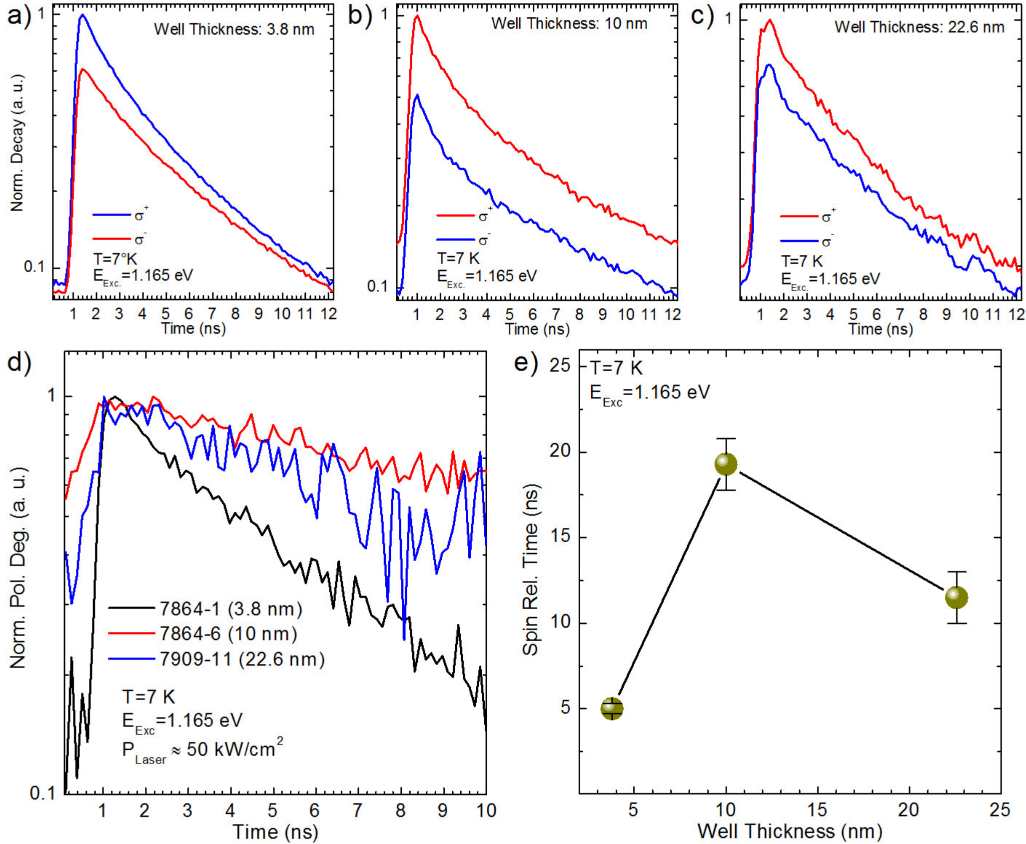


Figure 3.2: Upper panel: $\sigma^+$ (blue lines) $\sigma^-$ (red lines) resolved TRPL decay curves obtained from the 7864-1 (a), 7864-6 (b) and 7909-11 (c) at T = 4 K under 1.165 eV excitation energy. The power of the laser was kept constant during all the measurements at P=50 kW/cm$^2$. Lower panel: (d) Normalized decay curve of the circular polarization degree obtained from the 7864-1 (black line), 7864-6 (red line) and 7909-11 (blue line). (e): Spin relaxation time as a function of the QW thickness. $\tau_S$ values were obtained by means of decreasing exponential fits. Where not visible, the error bar is below the dimension of the full dot.

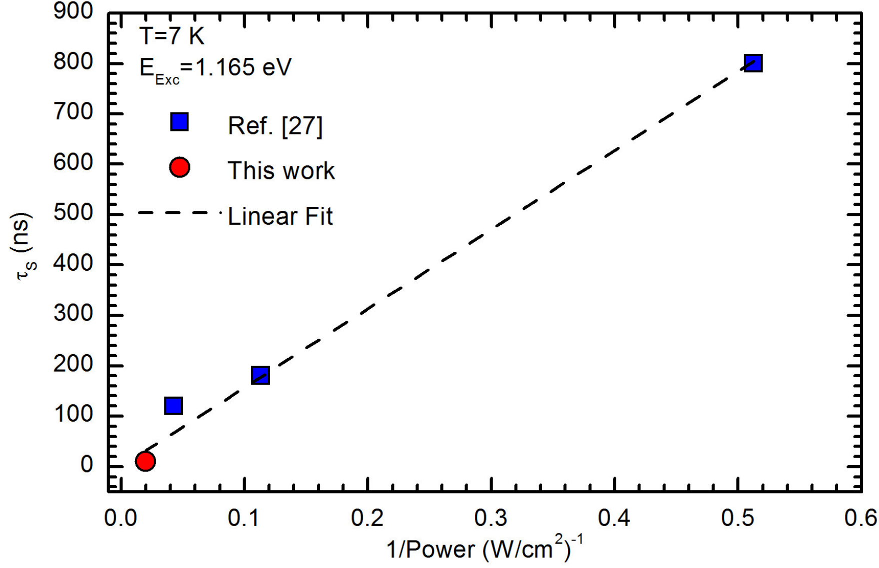


Figure 3.3: Low temperature $\tau_S$ as a function of the inverse power density. Blue squares refer to data of Ref. [27], while the red circle refers to the 7909-11 sample of this work. The black dashed line stems from a linear fit of the data.

A.2.2, thus achieving pulse power densities values ranging from 160 to 23 kW/cm$^2$, while in this work, the very small size of the focused laser spot (see Appendix A.2.1) results in a pulse power density of about 50 kW/cm$^2$.[5]

It is worth noticing that, even comparing experimental findings obtained under very different conditions, a linear fit (black line) performed on all the data shows a very good linear dependence of the spin lifetime on the inverse excitation power, thus confirming the pivotal role of the electron-hole exchange interaction. Such a result can possibly explain the reduced lifetime observed in our samples, in comparison with the exceedingly long spin relaxation times pointed out by theoretical works on thermal electrons [21, 22].

[5]The pulse excitation power density is considered instead of the averaged one, since the electron-hole exchange interaction depends on the density of optically injected excited carriers [27].

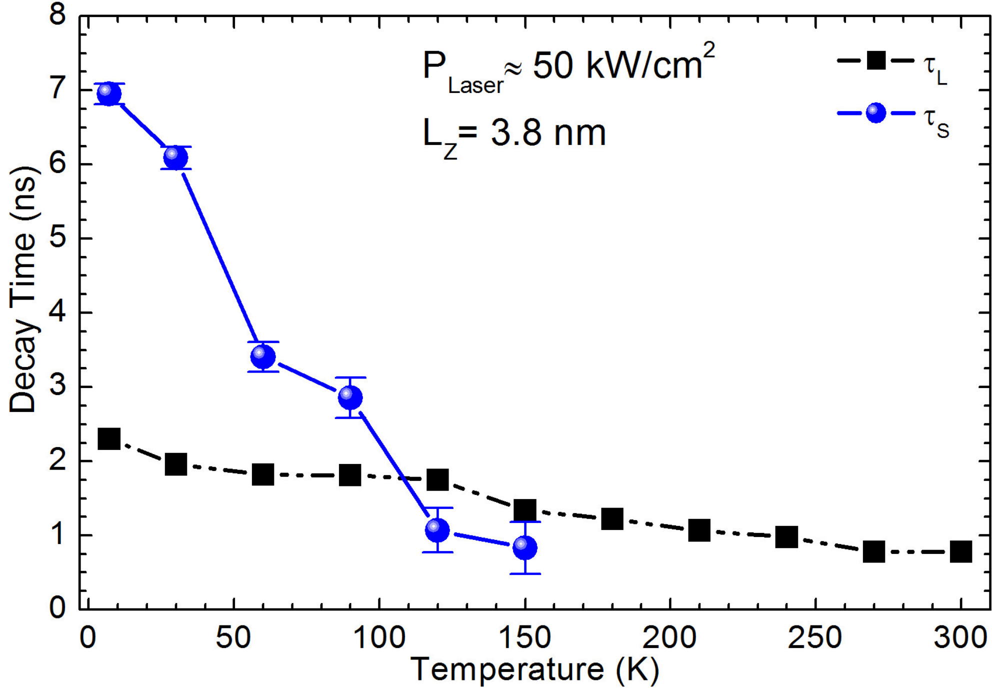


Figure 3.4: Blue dots: temperature dependence of the spin relaxation time ($\tau_S$). Black squares: temperature dependence of the electron lifetime ($\tau_L$).

## 3.3 Spin Lifetime Dependence on Temperature

In this section we will discuss the spin relaxation time dependence on the lattice temperature. This was addressed by means of polarization-and-time resolved PL measurements technique. The measurements were performed using an experimental set-up identical to that described in the previous section (Appendix A.2.1) but, in this case, the energy of the laser was tuned in order to always match the direct-gap absorption. Therefore the excitation energy was adjusted according to the Varshni's law [42] (Eq. 1.3).

The $\tau_S$ as a function of temperature for the sample with a 3.8 nm well thickness (7864-1, see Table 2.1) is reported in Figure 3.4 (blue dots) together with the measured electron lifetime (black dash-dotted line). The latter has been fully discussed in Section 2.6. A monotonic decrease of $\tau_S$ is demonstrated as the lattice temperature increases. A similar behaviour was

found both on the sample with $L_Z = 10$ nm and on that with $L_Z = 22.6$ nm, see Appendix C. Such a $\tau_S$ relaxation can be attributed to the Elliot-Yafet mechanism via intervalley electron scattering by shortwave phonon modes [97]. In Ge, this mechanism is expected to provide a strong contribution in the high temperature regime, due to the increasing presence of phonons [22]. On the other hand, when T<20 K, the population of these phonon modes is negligible, so that spin relaxation is governed by the intravalley processes, whose effect on spin information has been found to be less important with respect to that of the intervalley scattering [21, 22].

Experimental data shown in Figure 3.4 reveal that it is no more possible to measure the spin lifetime when the temperature exceeds 150 K, as it approaches the time resolution of the apparatus.

## 3.4 Conduction Electron *g*-factor

So far we have discussed the spin properties of $Ge/Si_{1-x}Ge_x$ MQWs heterostructures grown on a (001)-oriented Si substrate, showing the spin relaxation time dependence on the excitation power density and on the temperature. In the following, we extend our results by carrying out a PL-based experimental investigation of the Landé *g*-factor as a function of the well thickness.

Spin-orbit interaction leads to a deviation from the *g*-factor value ($g_e$ =2.0023) of free electrons [103]. In the particular case of Ge, ellipsoidal constant energy surfaces at the L points of the Brillouin zone yield a highly anisotropic *g*-factor [104, 105], which can be characterized by the two components $g_{||}$, along the main axis of the ellipsoid, and $g_{\perp}$, along the directions perpendicular to the axis of the L-valley ellipsoid.

The control of the electron Landé *g*-factor in solid state systems is considered as an important tool to enable the manipulation of spins by external fields. Investigations of Ge-on-Si heterostructures have been so far focused on the spin physics of holes (see, e. g. Ref. [106]). Only very recently the conduction electron *g*-factor of $Ge/Si_{1-x}Ge_x$ MQWs samples was experimentally measured by means of electron spin resonance (ESR) technique [27].

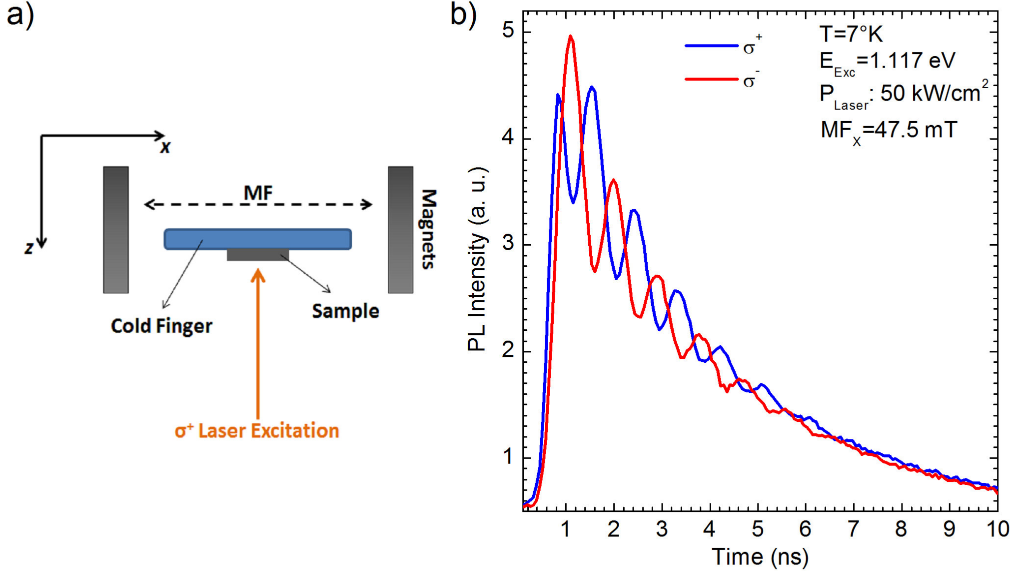


Figure 3.5: (a): Scheme of the experimental geometry used for quantum beat spectroscopy measurements. (b): $\sigma^+$ (blue line) and $\sigma^-$ (red line) polarization components of TRPL measurements performed on 7864-1 sample. Measurements were performed at T=7 K under a 47.5 mT magnetic field oriented along the $x$ axis. It is worth noticing the phase difference.

In this thesis we will provide the first experimental estimation of the Landé $g$-factor of conduction electrons on Ge-based heterostructures by applying quantum beat spectroscopy (QBS). This technique has been widely used to determine the Landé $g$-factor of III-V compound semiconductors [24, 25]. However, to date, it has never been utilized to experimentally investigate the anisotropic $g$-factor of group IV semiconductors. QBS relies on polarization-resolved TRPL measurements under an external magnetic field (MF). This technique allows one to infer the $g$-factor from the measurement of the Larmor precession frequency of the electrons spins.

To briefly explain the method, let us consider a magnetic field perpendicular to the propagation direction of the circularly polarized light [Figure 3.5(a)], which leads to a Larmor precession of CB electrons spins around the axis of the MF [23]. Under these conditions, the TRPL polarization components, $\sigma^+$ and $\sigma^-$, measured separately, will exhibit strong intensity oscillations with a phase difference of $\pi$ with respect to each other at a frequency

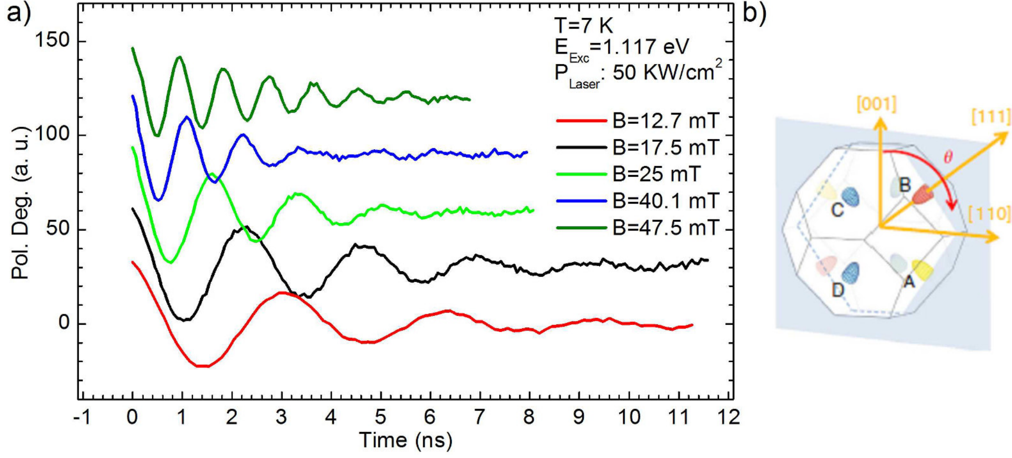


Figure 3.6: (a): Experimental time evolution of the PL polarization degree for five values of applied MF obtained from the 7864-1 sample ($L_Z$=3.8 nm) (b): Brillouin zone of bulk Ge. $\theta$ is defined as the angle between the (001) crystallographic direction and the MF (B). In our geometry $\theta = 90°$. The ellipsoidal isoenergetic surfaces of the CB at the L-point are also shown. Figure (b) is taken from Ref. [27].

equal to the Larmor frequency ($\omega_L$). Oscillations are called spin quantum beats, since they are interpreted as beatings between spin split ($\Delta E = \hbar\omega_L$) electron levels with the spin quantization axis parallel to the MF [26]. See for instance Figure 3.5(b), in which the sample with 3.8 nm well thickness (7864-1) was measured at T=7 K in a x-oriented MF of 47.5 mT. This figure demonstrates that a coherent spin dynamic of L-valleys CB electrons was achieved. The Larmor frequency can be obtained from the beatings of the circular polarization degree and, thus, the $g$-factor can be calculated using the following relationship:

$$\omega_L = \frac{g \cdot \mu_B \cdot B}{\hbar}, \tag{3.1}$$

where $\mu_B$ is the Bohr's magneton and B is the magnetic field.

The quantum beats obtained from the (001)-oriented Ge/$Si_{1-x}Ge_x$ MQWs heterostructure with a well thickness of 3.8 nm (7864-1) at T=7 K and for different values of the applied MF are shown in Figure 3.6(a). In our experimental configuration (Voigt configuration), the MF is applied in a plane

perpendicular to that of the growth axis direction. Since our study deals with $Ge/Si_{1-x}Ge_x$ MQWs heterostructures grown on (001)-oriented Si substrate, it means that, in this case, the MF is applied along the [110] crystallographic direction ($\Theta = 90°$), as pointed out in Figure 3.6(b). Apart from the applied MF, the experimental set-up used to carry out QBS was identical to that described in the previous section (fully described in Appendix A.2.1). We also employed a 1.117 eV excitation energy in the case of the sample with $L_Z = 3.8$ nm, while a 1.165 eV excitation was used to excite both the sample with $L_Z = 10$ nm and the sample with $L_Z = 22.6$ nm. Here, the time resolution was set at 64 ps in order to more accurately sample the electrons spin precession. Furthermore, it should be noted that, differently from the literature work by Giorgioni *et al.*, in which the $g$-factor was measured by means of the ESR technique [27], here a single Larmor frequency is observed, so that it is not possible to resolve the $g$ anisotropy caused by the four equivalents L-valleys of the Ge CB. Thus, in this case, we measure an averaged Landé $g$-factor, which we will label as $g_{eff}$. Beatings of the circular polarization degree were also obtained measuring the (001)-oriented $Ge/Si_{1-x}Ge_x$ MQWs samples with well thickness of 10 nm and 22.6 nm (not shown), named 7864-10 and 7909-11, respectively (see Table 2.1).

Figure 3.6(a) reveals that the Larmor frequency depends on the strength of the applied MF. In particular, the dependence of $\omega_L$ versus B is linear, as expected [24, 25, 26], for all the samples. According to equation 3.1, the slope of the straight line provides the Landé $g$-factor.

Our findings demonstrate that the $g_{eff}$ depends on the well width. In particular, a $g$-factor of $1.59 \pm 0.01$ is obtained from the sample with $L_Z = 3.8$ nm, while the same $g$-factor of $1.25 \pm 0.01$ is obtained for the sample with $L_Z = 10$ nm and from the sample with $L_Z = 22.6$ nm, as shown in upper panels of Figure 3.7.

Figure 3.7(d) summarizes the $g_{eff}$ as a function of the well thickness (violet circles) obtained from the QBS measurements. A similar behaviour is in line with the theoretical prediction by Baron *et al.*, and compares well with recent ESR data [27]. The comparison between our experimental data and the theoretical prediction provided by Ref. [28] can be appreciated in Figure

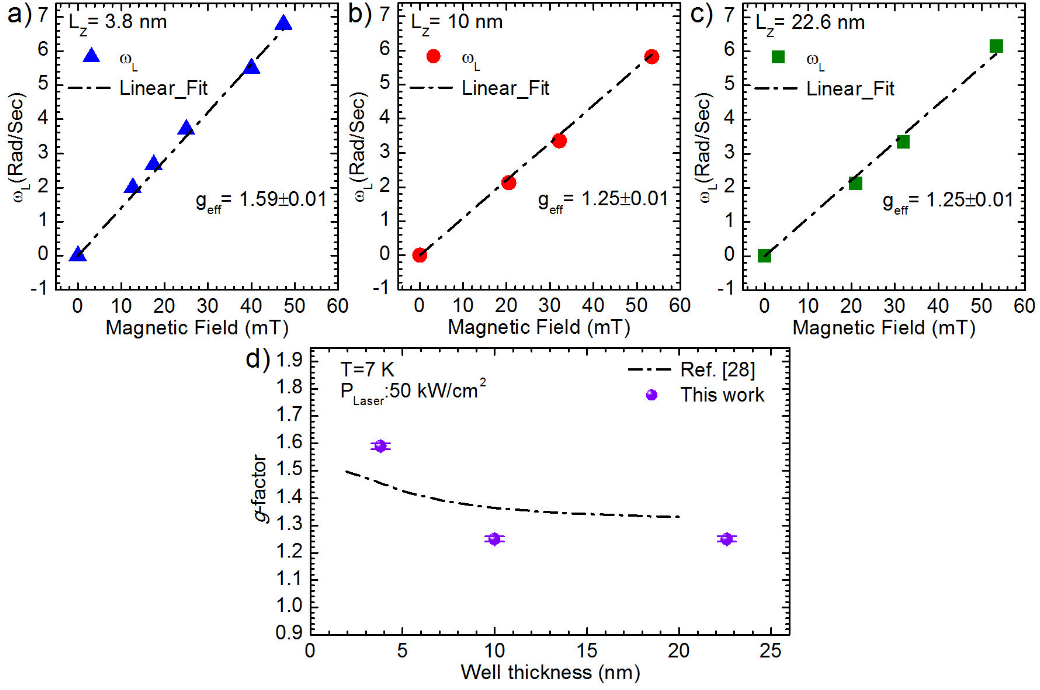


Figure 3.7: Upper panel: Dependence of the electron spin Larmor pulsation ($\omega_L$) on the magnetic field strength for $L_Z$=3.8 nm (blue triangles), 10 nm (red circles) and 22.6 nm (green squares). Black dash-dotted lines are linear fits. Lower panel: Landé $g$-factor dependence of L electrons on the QW thickness obtained through the linear fits shown in the lower panel (violet dots). The black dash-dotted line was obtained through digitization of data from Figure 2(a) of Ref [28] in the case of x=1.

3.7(d). To get a meaningful comparison, we considered the predicted in-plane component of the electron $g$-factor in the case of pure Ge QWs (x=1, see Figure 2(a) of Ref. [28]) for (001)-oriented systems.

This measured dependence can be explained according to the following physical picture. For sufficiently thick QWs, the $g_{eff}$ approaches the bulk value of a strained homogeneous material. On the other hand, when the QWs thickness is reduced down to $\sim$ 4 nm, the quantum confinement effects lead to an increase of the effective $g$-factor. According to theory, when the $L_Z$ value is further reduced below the $\sim$ 4 nm limit, the electron wavefunction is expected to gradually penetrate into the SiGe barrier layer, which provides a non-vanishing contribution to the resulting $g_{eff}$ of the system [28]. To avoid

the latter phenomenon, our study does not deal with ultrathin QWs.

Finally we notice that, even though the $g$-factor dependence on the well thickness agrees with the theory, a non-negligible difference can be still appreciated. We attribute this to the following reasons. First of all, Baron *et al.* [28], considered a non-symmetrical $Si_{0.3}Ge_{0.7}/Ge/Si_{0.2}Ge_{0.8}$ QW system, while we studied a symmetric Ge/ $Si_{0.15}Ge_{0.85}$ QWs heterostructures, which could present a different strain level. Moreover, it should be noted that the $k \cdot p$ calculation does not take into account the energy distribution of L-valleys electrons, which is known to lead to non-negligible corrections to the band edge effective $g$-factor value [23].

# Chapter 4

# Ge/SiGe MQWs (111)-Oriented

In this chapter we investigate electronic structure, optical and spin properties of a Ge/$Si_{1-x}Ge_x$ Multiple Quantum Wells (MQWs) sample grown on a (111)-Si substrate. At first we will show the results of a $k \cdot p$ calculation, providing information on the quantum confined energy levels of the heterostructure. Afterwards, the optical properties are studied through PL. In particular, the spin dynamics and the energy relaxation processes of the spin-oriented photoexcited carriers will be investigated via the PRPL technique. Time-resolved photoluminescence will provide us the electron lifetime ($\tau_L$) and the spin relaxation time ($\tau_S$) of CB electrons. Finally, a first comparison between nominally identical Ge/$Si_{1-x}Ge_x$ MQWs structure grown along the (111)- and (001)-oriented substrates will be presented.

## 4.1 Electronic Structure and Optical Properties

The growth of Ge/$Si_{1-x}Ge_x$ QWs on high index Si substrate, such the (111) crystallographic orientation, combined with a proper strain control, opens up the possibility to tailor the band structure and the spin properties of Ge [107]. Moreover, (111)-oriented Ge-based materials are characterized by a higher

carrier mobility with respect to the (001)-oriented ones [108]. In addition, the dislocation dynamics strongly depends on the substrate orientation. It has been demonstrated that the possibility to grow epitaxial SiGe layers under tensile strain in the (111) plane inhibits stacking fault defects generation [109] (see Section 2.2) which, on the other hand, is favored in (001)-oriented systems [110]. For these reasons, the growth on a (111)-oriented surface is considered a suitable route to improve the quality of the crystal.

Furthermore, although according to former works the scattering among equivalent L valley is forbidden by symmetry [111], recent theoretical works suggest the intervalley scattering within the four-fold degenerate L-valleys of Ge as one of the main spin relaxation channels [21, 22]. In this context, since heteroepitaxial structures deposited on (111) crystallographic direction exhibit compressive biaxial strain, the $L$ valley degeneracy is broken, so that they are expected to be excellent candidates for achieving exceptionally long spin relaxation times and higher carriers mobility in Ge.

Tang *et al.* [21] report a tight binding model to calculate the intrinsic spin relaxation of conduction electrons in Ge as a function of the energy splitting between the lower conduction valley and the others. In particular, they disentangle intervalley and the intravalley scattering contributions to the electron spin lifetime, showing that a [111] strain can yield just a single nondegenerate valley at the CB edge, thus inhibiting the intervalley scattering process and leading to a substantial spin lifetime lengthening. In a different paper, Li *et al.* [22] employ group theory to obtain the intervalley spin flipping matrix elements for electron scattering between different energy-minima points in Ge. In this work they show that, due to the uniaxial compressive strain along [111] crystallographic direction, the L-valley degeneracy is completely removed, thus resulting in a single low-energy valley oriented along the strain axis. In this case, if the strain level is large enough, the energy splitting is sufficient to quench the intervalley spin relaxation mechanism [21]. These is suggested as the optimal condition to achieve exceptionally long electron spin lifetime in Ge, since they demonstrate that, under [111] uniaxial strain, the intervalley spin relaxation rate ($1/\tau_{\mathrm{S,inter}}$, Eq. 10 of Ref.) drops to zero. Moreover, they also discuss the case of compressive biaxial strain along the

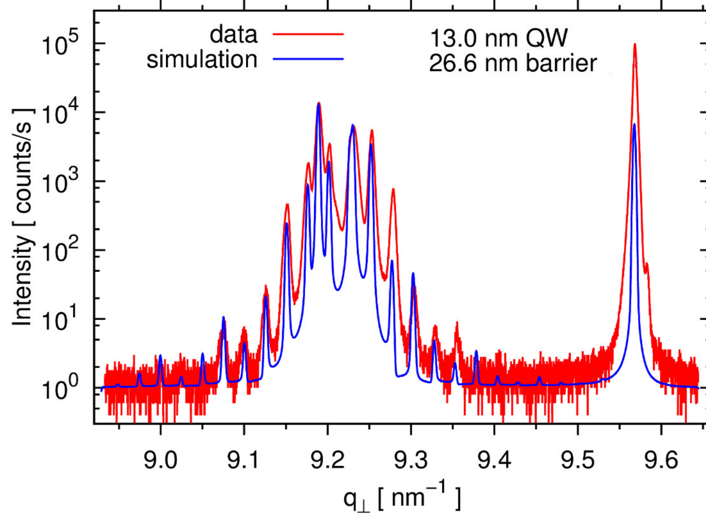


Figure 4.1: X-ray diffraction spectrum of the Ge/$Si_{1-x}Ge_x$ MQWs sample grown on (111)-oriented Si substrate (red line) and simulation (blue line) allowing the QW and barrier thickness determination. The subscript $\perp$ indicates the growth direction.

[111] direction, in which three of the valleys shift down in energy and one shifts up. This is the case of (111)-oriented Ge/$Si_{1-x}Ge_x$ QWs. Although it does not represent the optimal strain configuration, but the achievable partial removal of the L-valley degeneracy is suggested to be sufficient to observe a spin lifetime lengthening with respect to that characteristic of (001)-oriented Ge.

It is worth noticing however, that the integration of Ge QWs on Si(111) substrate is challenging. Indeed, in this case, it is not possible to utilize the conventional graded virtual substrate (GVS) commonly used to grow epitaxial Ge-based heterostructures on (001)-oriented Si substrate (see Section 2.2 and e. g. Refs. [112, 113, 114]). In order to obtain Ge-rich layers with a structural quality comparable to that of GVS on (001) Si substrate, a composition grading of about 1% per $\mu$m would be needed, resulting in a markedly thicker GVSs [112]. For this reason, an alternative viable approach for the deposition of Ge-rich SiGe layers on (111)-oriented Si was proposed by Gatti *et. al.* [115]. It consists in a *reverse*, *double-step* virtual substrate. The sample investigated in this chapter, named 9056-E9, was grown by LEPECVD

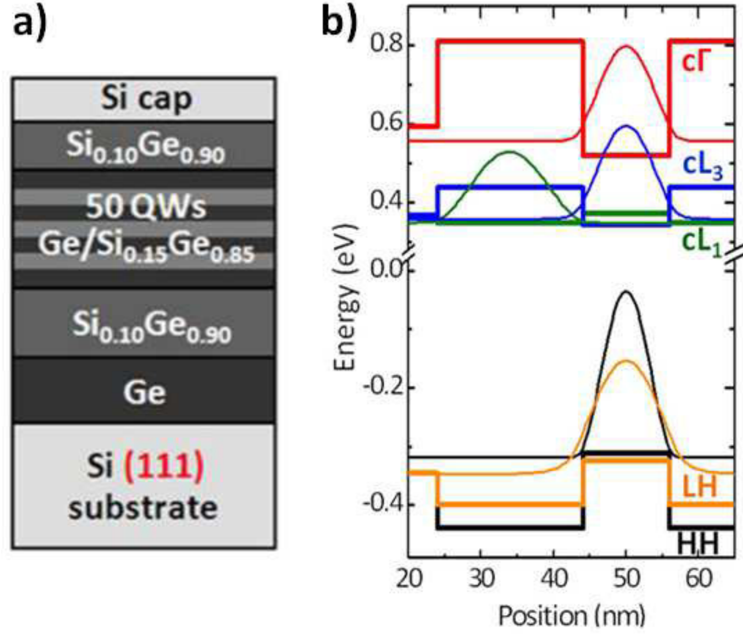


Figure 4.2: (a): Schematic of the analysed sample. (b): Band alignment of 9056-E9 sample. The square modulus of the wavefunction of the first confined level is shown for each band. Figures are taken from Ref. [115].

(see Section 2.4) using the recipe of Ref. [115]. The sample is based on a 2 $\mu$m thick Ge layer deposited on a 3.5° miscut Si(111) substrate at 500° C, with a growth rate of 4.2 nm/s. The Ge layer experiences *in-situ* 6 annealing cycles (600° − 780° C) at a pressure of $\sim 5 \cdot 10^{-7}$ mbar, which allows the reuction of the density of defects. The growth then proceeds by depositing a 1 $\mu$m thick $Si_{0.10}Ge_{0.90}$ layer at 475° C with a growth rate of 5 nm/s. Finally, 50 Ge/$Si_{0.15}Ge_{0.85}$ QWs periods are grown at 475° C with a rate of 4.2 nm/s. The well and barrier thickness, determined by high resolution X-ray diffraction (Figure 4.1), are $\sim$ 13 nm and $\sim$ 27 nm, respectively[1]. A schematic design of the investigated sample is shown in Figure 4.2 (a).

The band alignment and square modulus of the wavefunction of the first confined levels of each band obtained by an 8 bands $\mathrm{k} \cdot \mathrm{p}$ calculation are shown in Figure 4.2 (b) [115]. Strain and confinement effects were evaluated

[1]Sample was grown by Prof. G. Isella and Dr. F. Isa, while X-ray characterization was performed by Dr. D. Chrastina, at the L-NESS Centre of Como (Italy)

by means of an 8 band $k \cdot p$ calculation, while band alignment and confined states have been calculated using the set of deformation potentials reported in Ref. [116] and the Nextnano software package [117]. Figure 4.2 (b) clearly points out the type I band alignment of the direct band gap. Moreover, there is a character inversion between the top of the VB in well and barrier regions (see Figure 2.6). This fact has to be ascribed to the different nature of the strain, which is tensile in the barriers and compressive in the wells and it leads to a higher offset for HH VB states, as already observed also in $Ge/Si_{1-x}Ge_x$ QWs grown on (001)-oriented Si substrate and explained in Section 2.4 [19]. It is worth noticing that the L valleys are split. Indeed, due to the compressive strain along (111) plane, the degeneracy is partially removed, thus giving rise to a state, $cL_1$, along the [111] direction, and three degenerate minima, $cL_3$, along the [-111], [1-11] and [11-1] directions. Due to the compressive strain, $cL_3$ states are the lowest CB levels in the well. Moreover, while a type-I band alignment is predicted for $cL_3$, $cL_1$ is are characterized by a type-II band alignment. In the latter case, electrons are confined in the barrier region, so that these states are not expected to provide a significant contribution to the optical properties of the system.

The low temperature, CWPL spectrum of 9056-E9 sample is shown in Figure 4.3. CWPL measurements were performed by using a $\mathrm{Nd:YVO_4}$ laser operating at 1.165 eV, while the PL signal was probed through a dispersive system equipped with a single channel InGaAs photodiode working in the $0.516 - 1.127$ eV range (a detailed description of the experimental set-up is provided in Appendix A.1, Line B). In the low energy range, as expected, the PL spectrum it is dominated by transitions involving electrons recombining from the L valley ($cL_3 1 - HH1$). In particular, we ascribe the prominent feature at 0.732 eV to the longitudinal acoustic (LA) phonon-assisted transition, while the feature at 0.757 eV arises from the no-phonon (NP) emission across the indirect-gap [19]. A weaker PL peak related to the direct-gap emission is found at the high energy side of the spectrum, in the $0.900 - 1.120$ eV range. In particular, as underlined in the inset of Figure 4.3 (a), the direct-gap emission has two components. The one at about 0.945 eV is attributed to the direct $c\Gamma 1 - HH1$ emission, while the weaker band at

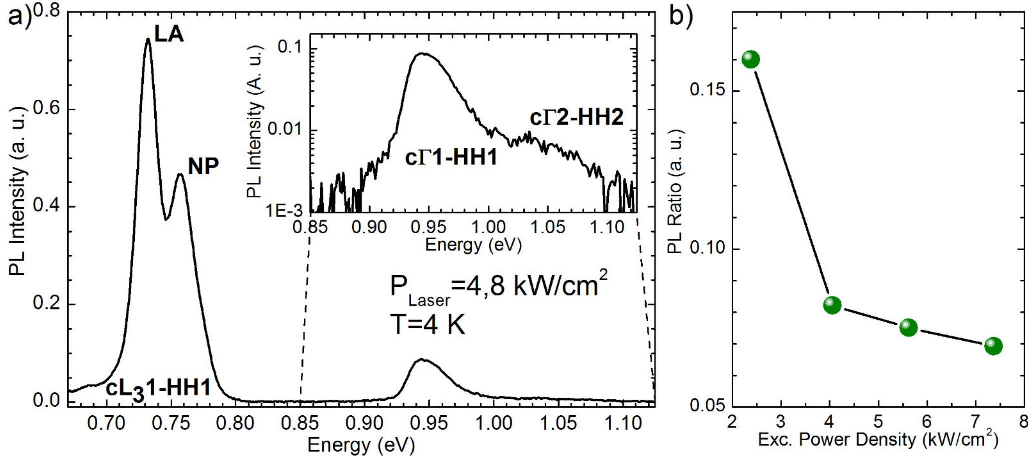


Figure 4.3: (a): Low temperature CWPL spectrum obtained from the (111)-oriented $Ge/Si_{1-x}Ge_x$ MQWs sample under 1.165 eV laser excitation. Phonon mediated indirect transitions are labelled, while the direct-gap transition magnification is reported in the inset. (b): Direct-to-Indirect PL intensity ratio obtained from the $cL_3 1 - HH1 : NP$ transition as a function of excitation power density

higher energy stems from the $c\Gamma 2 - HH2$ recombination.

Furthermore, from the direct-to-indirect PL intensity ratio as a function of excitation power density (PD) reported in Figure 4.3 (b), two different regimes can be distinguished. The first one, when $PD \geq 4$ kW/cm$^2$, is characterized by a PL ratio decreasing by increasing the PD. On the other hand, the measurement performed at $PD = 2.5$ kW/cm$^2$ clearly reveals an increase of the direct-to-indirect ratio, which in this regime seems to be characterized by a strong slope enhancement with respect to the one observed in the high PD regime. Since it is well known that the ultrafast direct-gap transition is not affected by non-radiative recombination channels, this behaviour is likely to be caused by the presence of defects states, which act as the main drain source for carriers residing in the L-valley.

The low temperature decay curves obtained from the indirect-gap emission of the 9056-E9 sample by means of time-resolved (TR) PL measurements as a function of excitation power density are shown in Figure 4.4. TRPL measurements were carried out by using a $Nd : YVO_4$ Q-switched laser operating at 1.165 eV and at a frequency of 10 kHz with a temporal width of about

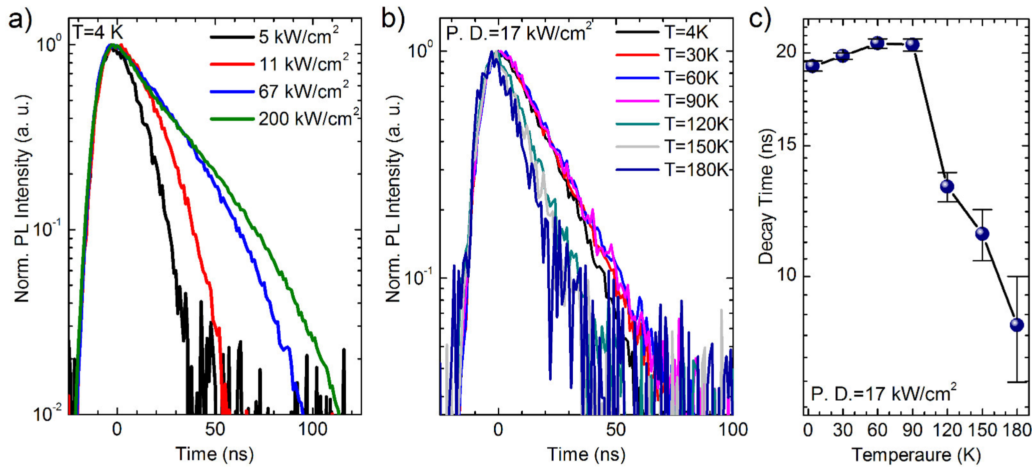


Figure 4.4: Low temperature decay curves obtained from the $cL_1 - HH1 : NP$ line as a function of excitation power density (a) and as a function of temperature (b). (c): Electron lifetime values in the $4° - 180°$ K temperature regime.

7 ns. The PL decay time was probed through a photomultiplier tube with a cut-of at 0.775 eV coupled with a monochromator (see Appendix A.2.2 for a detailed description of the experimental set-up). These measurements further corroborate the above-mentioned picture. Indeed, the low temperature decay curves shown in Figure 4.4 (a), demonstrate that the electron lifetime grows as the excitation P. D. increases. A typical scenario is that in the low P. D. regime, non-radiative recombination mechanisms dominate the PL decay curve, thus resulting in a reduction of the electron lifetime. When the excitation P. D. increases, the higher concentration of photoexcited carriers seems to lead to a saturation of defect states. Under this condition, the weight of radiative recombination events becomes increasingly important and, as a consequence, the carrier lifetime gradually increases.

The PL decay of the indirect $cL_1 - HH1 : NP$ transition has also been measured as a function of temperature between 4 K and 180 K at PD $\sim 17$ kW/cm$^2$ (Figure 4.4 (b)). In this case, the PD value was suitably chosen in order, on one hand, to avoid an Auger contribution to the PL decay and, on the other hand, to minimize the non-radiative recombination mechanisms effects playing an important role in the low P. D. regime, as already explained

above. Non-radiative Auger contribution is expected to affect the carrier lifetime at an early stage of the recombination dynamics under pulsed excitation because of the initial high density of photoexcited carriers [39] and, for this reason, it is expected to increase as the excitation power density increases. From the curves reported in Figure 4.4 (b), a slight increase ($\sim$ 2 ns) of the $\tau_{\mathrm{L}}$ value can be appreciated in the 4-90 K temperature range. This behavior, summarized in Figure 4.4 (c), was never observed on similar (001)-oriented Ge-based heterostructures [80]. At T = 4 K again it corroborates the picture according to which non-radiative channels provided by defect states affect the photoexcited carriers recombination, thus resulting in an overall reduction of the electron lifetime. The contribution of these non-radiative channels loses importance as the lattice temperature of the sample increases, so that the $\tau_{\mathrm{L}}$ slightly increases between 30 K and 90 K. By further increasing the temperature, the $\tau_{\mathrm{L}}$ monotonously decreases. Indeed, a higher temperature can cause thermal energy activation [118], which leads to an higher exciton mobility. Under these conditions it is more likely for photoexcited electrons to recombine on defect states, thus leading to a $\tau_{\mathrm{L}}$ reduction, as already observed in similar Ge/$\mathrm{Si_{1-x}Ge_x}$ MQWs heterostructures grown on (001)-oriented Si substrates [80]. The decreasing signal-to-noise ratio, besides the fact that the electron lifetime is shorter than the laser pulse duration, did not allow us to carry out TRPL measurements at temperature higher than 180 K.

## 4.2 Investigation of the Spin Properties

In this section we will show a detailed study of the spin properties of the (111)-oriented Ge/$\mathrm{Si_{1-x}Ge_x}$ MQWs heterostructures. Both indirect-gap and direct-gap emission will be investigated through PRPL measurements. All the data discussed in the following were taken under 1.165 eV, right-handed ($\sigma^+$) circularly polarized laser excitation. Thus, in this case, we attribute positive(negative) values of $\rho$ to co(counter)-circular polarized PL with respect to the excitation. In this case, we measured the co-circular ($I_{\sigma^+}$) and the counter-circular ($I_{\sigma^-}$) component of the PL signal. The circular polarization degree was calculated using Equation 1.7. The PL signal of the indirect-gap

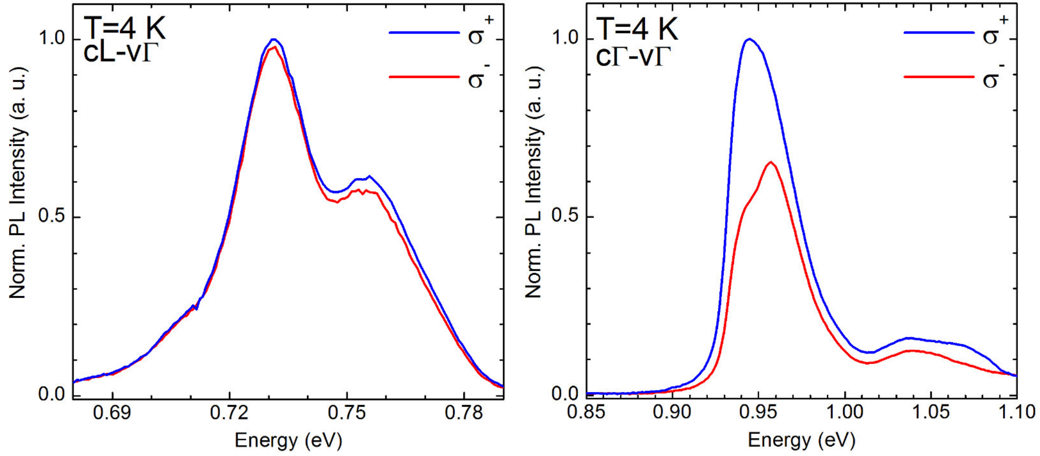


Figure 4.5: Low temperature polarization-resolved PL spectra related to indirect-gap (a) and direct-gap (b) emission of the 9056-E9 sample. The blue (red) spectrum stems from PL emission co(counter)-polarized with respect to the laser excitation.

emission was probed by means of a single channel InGaAs photodiode with a cut-off at 0.516 eV (Appendix A.1, Line B), while an InGaAs array detector with a cut-off at 0.75 eV was used to investigate the direct-gap PL signal (Appendix A.1, Line A). The latter guarantees an excellent signal-to-noise ratio at photon energies corresponding to the direct-gap PL emission, while the former allows us to gather access to indirect-gap transitions.

PRPL spectra obtained from the Ge/$Si_{1-x}Ge_x$ MQWs sample grown on (111)-oriented Si substrate at T=4 K are shown in Figure 4.5. Blue (red) curves refer to PL emission co(counter)-polarized with respect to the excitation.

The polarization analysis related to the direct-gap recombination (Figure 4.5 (b)) reveals a robust optical orientation of spins within the Γ valley at T=4 K. Under $\sigma^+$ laser excitation, it has already been shown (Section 1.3) that electrons are injected into $|J; m_j\rangle = |1/2; -1/2\rangle$ CB states starting from $|3/2; -3/2\rangle$ HH states as well as to $|1/2; 1/2\rangle$ CB states starting from $|3/2; -1/2\rangle$ LH states (Figure 1.4)[2]. Since the excitation energy is 1.165 eV,

[2]Note that the sketch of Figure 1.4 represents the bulk case. Here the compressive biaxial strain in the wells leds to the removal of the VB degeneracy (see Figure 4.2 (b)).

carriers are photoexcited away from the first confined HH and LH states. As pointed out in the literature for (001)-oriented Ge/$Si_{1-x}Ge_x$ MQWs [13], according to tight-binding calculations [119] and to data of III-V group SCs [120], just after excitation the electron spin polarization is expected to be $P_0 \sim 28\% - 34\%$. Now, assuming complete heavy holes depolarization after thermalization towards the $\Gamma$ valley bottom, electrons can recombine with $|3/2; -3/2\rangle$ and with $|3/2; 3/2\rangle$ emitting $\sigma^+$ and $\sigma^-$ circularly polarized light, respectively. Since on this time scale we can neglect electrons spin depolarization, the degree of circular polarization expected from the $c\Gamma 1 - HH1$ transition is $P \sim 0.96 P_0$. This value is in very good agreement with our experimental finding of $\rho = (30\% \pm 1\%)$ which can be appreciated at 944 meV.

Moreover, looking at the $\sigma^-$ spectrum (red line) of Figure 4.5, the presence of a not-well-resolved, counter-polarized feature at 957 meV is seen, which can be ascribed to the $c\Gamma 1 - LH1$ direct-gap transition.

The polarization-resolved spectra in the indirect band-gap ($cL - v\Gamma$) region are shown in Figure 4.5 (a). It is worth noticing that, under 1.165 eV excitation condition, spin polarized carriers are injected in the $\Gamma$ valley CB state. Photoexcited electrons are then scattered towards the L valley absolute minimum on a subpicosecond time scale [118, 11], possibly preserving their spin orientation. In this case, the small but non-vanishing circular polarization degree of Figure 4.5 (b) reveals that a non-zero electron spin polarization was achieved within the L valley[3]. This represents a first experimental proof that the spin relaxation time is at least comparable with the recombination time ($\tau_S \sim \tau_L$) which, at low temperature, lies in the tens of ns regime (Figure 4.4). The NP feature reveals a circular polarization degree of $3\% \pm 0.5\%$, while $\rho = (1.3\% \pm 0.4\%)$ is calculated for the LA peak. Both the transitions are co-polarized with respect to the excitation. A similar behavior was already observed by F. Pezzoli *et. al.* on Ge/$Si_{1-x}Ge_x$ MQWs grown on (001)-oriented Si substrate [13]. Employing a group theory analysis similar to that of Ref. [121], the authors attribute the slight difference in the measured

[3]Holes depolarize very quickly. Only spin polarization of electrons provides a polarized contribution to the PL signal, as pointed out in Section 1.3

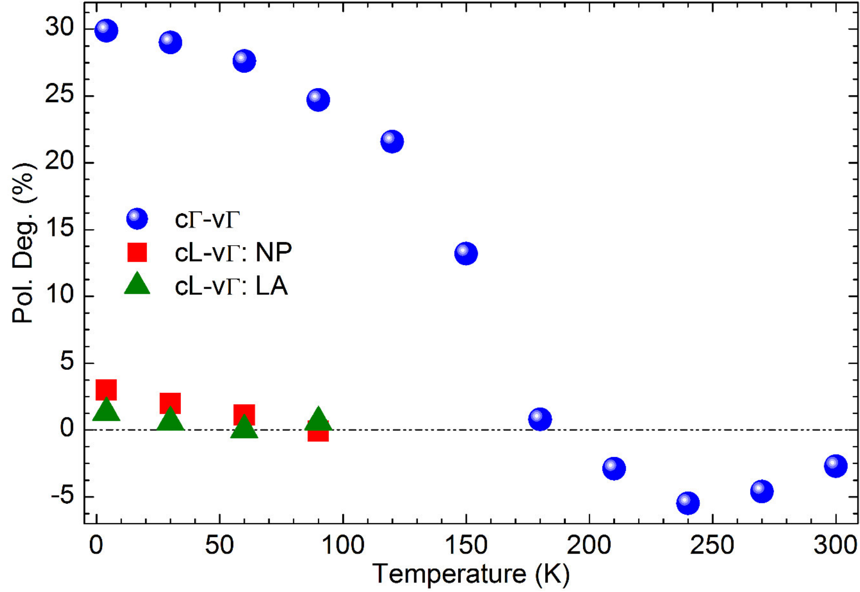


Figure 4.6: Temperature dependence of $\rho$ for the direct-gap (blue circles), the $\mathrm{cL}-\mathrm{v}\Gamma:\mathrm{NP}$ (red squares) and the $\mathrm{cL}-\mathrm{v}\Gamma:\mathrm{LA}$ (green triangles) transitions.

polarizations of the NP and LA replica to their proximity to the TA and TO transitions, respectively. On one hand, a phonon assisted LA transition contribution to the polarized emission is expected to be $I_{\sigma^+} : I_{\sigma^-} = 3 : 1$. On the other hand, regarding TO and TA, the ratios are $1 : 3$ and $1 : 0$, respectively [13]. Furthermore, as we will see in the following paragraph, the initial polarization at the $\Gamma$ point is $\sim 30\%$. This expectation, together with the predicted $\mathrm{cL}-\mathrm{v}\Gamma:\mathrm{LA}$ transition rate ($\mathrm{I}^{\mathrm{LA}}_{\sigma^+}/\mathrm{I}^{\mathrm{LA}}_{\sigma^-} = 3$) should result in a value of $\rho$ higher than the 1.3% measured. In this case, the observed low value of $\rho$ can be attributed to the proximity of the electron-hole pair in the QW heterostructure, which leads to a strong spin relaxation caused by exchange interaction of confined exciton states and which is expected to play an important role at low temperatures and in intrinsic QWs [13, 122].

The temperature dependence of the degree of circular polarization for the direct-gap (blue circles) and the indirect-gap (red squares and green triangles) is reported in Figure 4.6. The $\mathrm{cL}-\mathrm{v}\Gamma:\mathrm{NP}$ and the $\mathrm{cL}-\mathrm{v}\Gamma:\mathrm{LA}$ transitions point out a temperature-dependent depolarization mechanism.

In particular, the spectra are no longer circularly polarized when the temperature approaches 90 K. This depolarization has to be ascribed to the spin-flipping caused by the increasing presence of phonons due to the lattice heating, as predicted by the Elliot-Yafet spin relaxation mechanism [97]. Also this experimental finding is in line with what was observed on (001)-oriented Ge/$\mathrm{Si_{1-x}Ge_x}$ MQWs [13], where the temperature-dependent polarization of the indirect-gap emission was explained in terms of the dependence of the circular polarization degree on the $\tau_\mathrm{L}$-over-$\tau_\mathrm{S}$ ratio [123]:

$$\rho = \frac{\rho_0}{1 + \tau_L/\tau_S}, \tag{4.1}$$

where $\rho_0$ is the initial polarization degree. Equation 4.1 shows that the value of $\rho$ depends on the spin relaxation time. As the latter decreases the former rapidly goes to zero.

We now focus our attention on the temperature dependence of $\rho$ related to the direct-gap transition. The blue circles of Figure 4.6 demonstrate that $\rho$ decreases as the temperature increases, and that, as a consequence of the thermal activation of the spin relaxation, it drops to zero as the lattice temperature reaches T=180 K. This is in line with reports for Ge/$\mathrm{Si_{1-x}Ge_x}$ MQWs heterostructures grown on the more conventional (001)-oriented Si substrate [85]. Surprisingly, by further increasing the temperature above T=180 K, the PL polarization changes sign, being counter-polarized with respect to the excitation and reaching a maximum ($\rho \sim -5.5\%$) at 240 K. Remarkably, these measurements represent a clear experimental proof of non-vanishing polarization at room temperature, where a $\rho$ value of $-2.7\%$ is found.

This finding can be better appreciated in Figure 4.7. Indeed, PRPL spectra obtained from the investigated sample at T=300 K (Figure 4.7(a)), clearly emphasizes that the direct-gap PL emission stems from the superposition of two cross-polarized contributions, as we deduced also from low temperature measurements. The counter-polarized PL peak maximum reveals that in this case the emission is dominated by recombination involving LH states. Notably, the low energy tail is co-polarized with respect to the excitation, thus

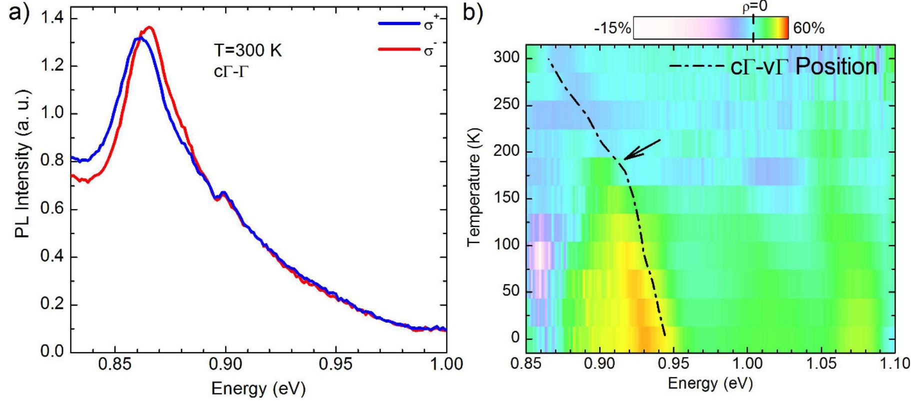


Figure 4.7: (a): Room temperature polarization-resolved direct-gap PL spectra. (b) Colour-coded map showing the behavior of $\rho$ as a function of temperature. Energy position of the $c\Gamma - v\Gamma$ PL feature is labeled by the black dash-dotted line.

evidencing the non-trivial contribution of the recombination on HH states.

This experimental evidence elucidates that the direct-gap transition arises from two different recombination channel, which alternatively dominate the PL signal depending on the temperature regime, as evidenced by the color-coded map in Figure 4.7(b). In particular, in the 4-150 K range, the dominance of the $c\Gamma1 - HH1$ recombination channel provides a photon emission co-circular with respect to the excitation ($\rho > 0$) while the dominance of the $c\Gamma1 - LH1$ channel in the 180-300 K temperature is proved by the fact that the main PL feature is counter-polarized ($\rho < 0$). At T=180 K, we can notice an abrupt redshift of the $c\Gamma - v\Gamma$ maximum position, as underlined by the S-like shape of the black dot-dashed line in Figure 4.7(b). This behavior suggests that a change in the dominant recombination channel is occurring in the direct-gap emission. Hence, at T=180 K, the $c\Gamma1 - HH1$ and the $c\Gamma1 - LH1$ recombination channels provide equal contributions to the PL signal, leading to a non-circularly polarized photon emission ($\rho \sim 0$)

These results were never observed in Ge-based system grown along the (001)-oriented crystallographic direction. The non-zero circular polarization degree measured up to room temperature proves that, actually, a partial removal of the L valley degeneracy possibly limits the inter-valley scattering

and thus it might represent an efficient tool to enhance the spin lifetime of the photoexcited carriers. In the following section this suggestion will be demonstrated by means of polarization-resolved TRPL measurements, which provide direct access to the spin relaxation time of the photoexcited carriers.

## 4.3 Spin Relaxation Time

This section is devoted to the direct measurement of the spin relaxation time by means of polarization-resolved TRPL measurements. A detailed scheme of the experimental set-up is shown in Appendix A.2.2. As explained above, it has been theoretically predicted that a system grown on the (111) crystallographic orientation should possess an intrinsic $\tau_S$ longer than a (001)-oriented one. The aim here is to provide an experimental demonstration of this prediction, and to deepen and clarify experimental evidences discussed in the previous sections. For this reason, the spin lifetime of the (111)-oriented $Ge/Si_{1-x}Ge_x$ MQWs sample, named 9056-E9, has been compared with the spin lifetime of a $Ge/Si_{1-x}Ge_x$ MQWs sample grown on (001)-oriented Si substrate with the same structure, named 7864-6 (see Table 2.1). It is worth noticing that, since $\tau_S$ strongly depends on various phenomena, like the electron-hole exchange interaction [101, 102], we have chosen two samples with a similar QW thickness (i. e. $\sim 10$ nm) and measured them under the same experimental conditions (temperature and excitation power density).

Polarization-resolved TRPL decay curves obtained from the 9056-E9 and from the (001)-oriented samples at T=4 K are shown in the upper panels of Figure 4.8 (a) and (b), respectively.

The decay curves related to the circular polarization degrees of the samples grown along (111) (pink circles) and (001) (green circles) crystallographic directions, together with their corresponding exponential fits (black lines) are reported in the lower panels of Figure 4.8 (a) and (b), respectively. It is worth noticing that, right after excitation, the $\rho$ value of the (001)-oriented sample is higher ($\sim 10\%$) with respect to that of the (111)-oriented one ($\sim 8\%$). We remind that carriers photexcited via optical method possess an excess energy with respect to the valley bottom. Since we are considering non-

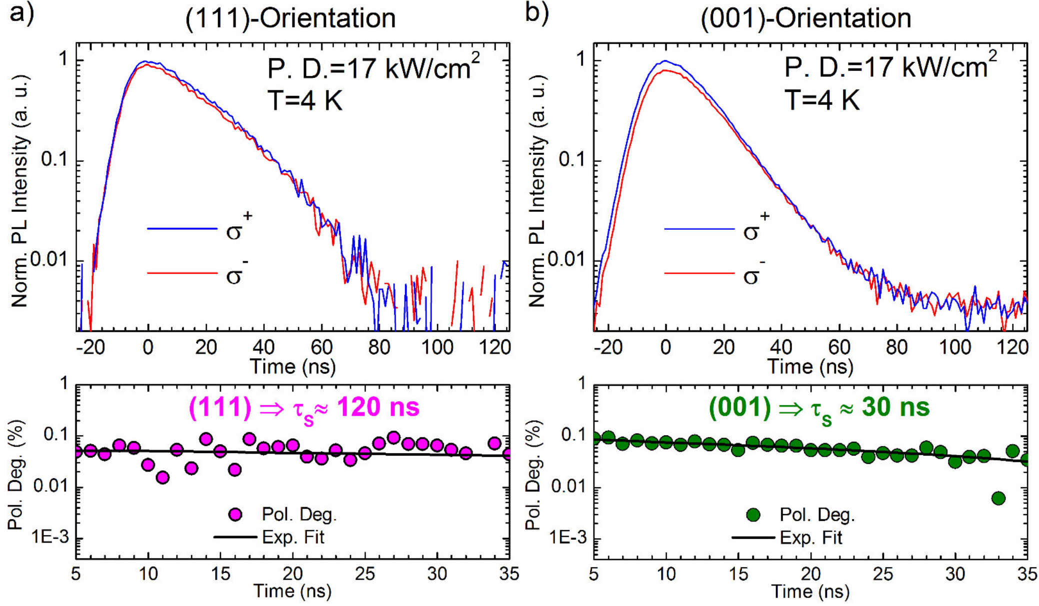


Figure 4.8: Upper panels: low temperature polarization-resolved TRPL decay of the (111)-oriented (a) and (001)-oriented (b) Ge-based heterostructures. Lower panels: corresponding degrees of circular polarization (pink and green circles) with their relative decreasing exponential fits (black lines).

thermal electrons, the higher the excess energy, the lower the degree of circular polarization [21, 22]. The smaller $\rho$ for the (111)-oriented sample is thus due to this energy relaxation process, as demonstrated by the smaller emission energy compared to that characteristic of the QWs grown along the (001)-oriented surface (see Figure 2.7 and 4.3). The partial removal of the L-valley degeneracy in (111)-oriented heterostructure, limiting the intervalley scattering, is thus expected to lead to a longer electron spin lifetime. Our measurements reveal that the $\tau_S$ value extrapolated from the (111)-oriented heterostructure is of about 120 ns while is about 30 ns for the (001) crystallographic orientation. Even if the error bars (not reported) exceed 15 ns, this observation clearly points out that the spin relaxation time measured on the (111)-oriented sample is almost an order of magnitude longer than the one measured on the (001)-oriented sample[4]. This experimental result proves

[4]Such a big spin lifetime difference can not be ascribed to the small difference in well thickness. Indeed, in Section 3.2 we revealed $\tau_S$ between 5 ns and 20 ns on (001)-oriented heterostructures with $L_Z$ ranging from 3.8 nm to 22.6 nm (see Figure 3.2).

that a partial removal of the L-valley degeneracy can be sufficient to enhance the spin relaxation time, as suggested by theoretical work of Li *et al.* in Ref. [22]. It is worth emphasizing that our evidence stems from experiments at T=4 K, where the intervalley scattering should be inhibited also in the case of completely degenerate L states. Thus, in this temperature regime, it would seem impossible to observe the theoretically predicted increase in $\tau_S$. In this case a typical scenario is that, due to the 1.165 eV excitation, non thermal electrons are photoexcited with an excess energy, so that they have to relax hundreds of meV before reaching the L-valley bottom. The energy loss due to this thermalization process is mediated by electron-phonon interaction, possibly opening up intravalley scattering as an effective a spin relaxation channel also at low temperatures.

# Conclusions

In the last decade, the integration of Ge within the complementary metal-oxide semiconductor (CMOS) technology stimulated detailed investigations of its structural and electrical properties. Notably, the multivalley nature of the Ge band structure has been pointed out to be a key factor to gather access to its optical processes. In this thesis, we exploited the quasi-direct behaviour of Ge to study the spin physics of bulk and low dimensional heterostructures.

In particular, polarization-resolved PL measurements of the direct-gap emission of a bulk Ge wafer revealed that it is possible to control the polarization of the emitted light by tailoring the pump condition at T=4 K. It has been shown that, exploiting the pivotal role played by scattering towards the satellite X-valleys during the energy relaxation process [38], it is possible to tune the density of photoexcited carriers occupying the two subspin states at the Γ-valley. This finally allows us to switch the chirality of the emitted photons without the use of any external magnetic fields or optical delay modulators. These findings possibly provide new routes for the realization of novel SOE devices, although the cryogenic temperature regime employed in this proof of concept experiments does not allows an immediate development of a spin-based light emitting device.

In this thesis, we have also carried out an experimental study of Ge QWs embedded in Ge-rich SiGe barriers. These heteroepitaxial systems have been widely investigated in recent years, since they demonstrate a type-I band alignment, thus offering the opportunity to achieve efficient radiative transitions [19]. In this work we reported a comprehensive study of the spin dynamics of the photoexcited carriers in Ge/$Si_{1-x}Ge_x$ MQws grown along two surfaces orientations; We employed different experimental parameters,

such as QW thickness, lattice temperature and excitation energy.

In particular, we showed that it is possible to obtain high degree of circular polarization ($\rho = 23\%$) for the indirect-gap emission by matching the direct-gap resonance. We investigated the spin relaxation time as a function of the well thickness and of the lattice temperature on (001)-oriented systems by means of polarization- and time-resolved PL technique. Measurements at T = 7 K revealed spin lifetime between 5 ns and 20 ns. Considering the different experimental conditions, these values are in good agreement with those provided by independent experiments [27]. In addition, the reduction of spin lifetime with increasing temperature allowed us to probe the effect of electron-phonon scattering interactions, theoretically predicted to dominate the spin relaxation when T > 30 K [22]. This thesis furthermore provides an estimation of the Landé $g$-factor of conduction band electrons achieved by means of quantum beat spectroscopy. This experimental technique, never applied to date to group-IV semiconductors, was used to unveil the coherent dynamics of L-valleys CB electrons, and to address the $g$-factor dependence on the well thickness. Our findings are in agreement with $\mathrm{k \cdot p}$ calculations [28] and electron spin resonance data of very similar samples [27].

Finally, it is worth noticing that literature works suggested the possibility to remove the L-valley degeneracy in Ge and achieve long spin lifetimes by inhibiting the intervalley scattering [22, 21]. Inspired by these predictions, we carried out an all-optical investigation of the spin properties of $Ge/Si_{1-x}Ge_x$ QWs epitaxially grown on a (111)-oriented Si substrate. This allowed us to achieve non-zero polarization of the direct-gap emission at room temperature. By measuring the spin relaxation time via polarization- and time-resolved PL, we revealed that, thanks to (111) surface orientation, it was possible to achieve a $\tau_S$ of about 120 ns. This is almost an order of magnitude longer than the $\tau_S$ obtained on a similar heterostructure grown along the (001) direction.

In conclusion, this work is devoted to an all-optical study of the spin properties of Ge-based systems. Original results obtained in this thesis, both on bulk Ge and on $Ge/Si_{1-x}Ge_x$ MQWs heterostructures, can represent a step forward in the comprehension of the relaxation and dynamics of spin polarized electrons in group IV materials.

# Appendix A

# Methods

This chapter is devoted to the description of the experimental set-ups used in this thesis to perform PL measurements. At first, we will describe the experimental set-up used for CWPL, then we will show details about those used for TRPL.

## A.1 Continuous Wave PL

A schematic drawing of the experimental set-up used in this thesis to perform continuous wave (CW) polarization-resolved photoluminescence (PRPL) is reported in Figure A.1. A continuous wave (CW) $\mathrm{Nd-YVO_4}$ laser (CNI Lasers) emits linearly polarized light at 1.165 eV (i. e. 1064 nm). The power ranges from a few mW to $\sim 500$ mW. The exciting beam, filtered through two 1064 nm band-pass (BP) filters and a 850 nm long-pass (LP) filter, is directed towards a half waveplate ($\lambda/2$) and on a quarter waveplate ($\lambda/4$) allowing the light incident on the sample to be right-handed ($\sigma^+$) circularly polarized. PRPL is carried out in backscattering geometry: the direction of luminescence detection is the same along which we excite the sample and perpendicular to the sample surface. The reflecting mirror for the laser beam is a circular, 3 mm diameter, silver mirror, mounted on a 5 cm diameter gimball support. In this way, most of the PL signal can reach the detection system. The laser light is focused on the sample surface by means of an

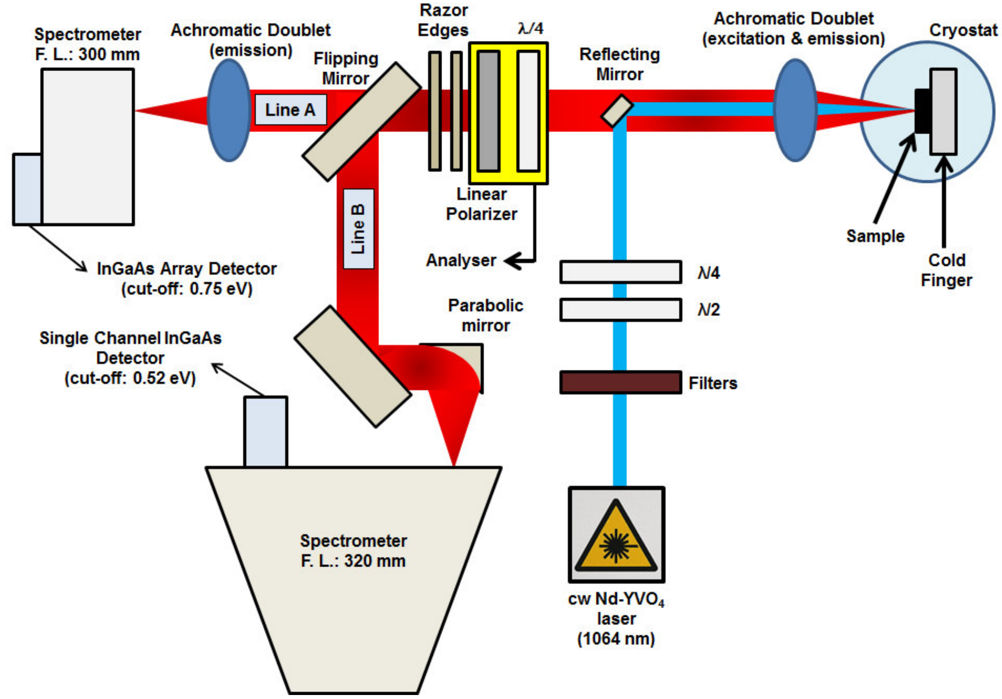


Figure A.1: Sketch of the experimental set-up used for polarization-resolved PL measurements described in Chapter 1.

achromatic doublet with 100 mm focal length. The focused spot diameter was measured to be $\sim 45\ \mu$m.

The sample is mounted on the cold finger of a cryostat cooled by a closed cycle helium refrigerator (Oxford Optistat AC-V12). Vacuum is obtained by means of a set of pumps (HiCube Classic, produced by Pfeiffer Vacuum).

The PL signal emitted from the sample is collimated by an achromatic doublet in front of the cryostat in a 2.5 cm diameter beam and sent to the analyser, consisting of a rotating $\lambda/4$ waveplate followed by a linear polarizer. The rotating holder on which the quarter waveplate is synchronized with the detection system. This allows us to achieve a complete overview about the PL polarization. Two 1064 nm razor edge (RE) filters eliminate the scattered laser light.

The PL signal then reaches a mirror that can be removed (flipping mirror), so that one can choose the spectrometer (A or B) and, thus, the detector. We will separately describe the two optical paths.

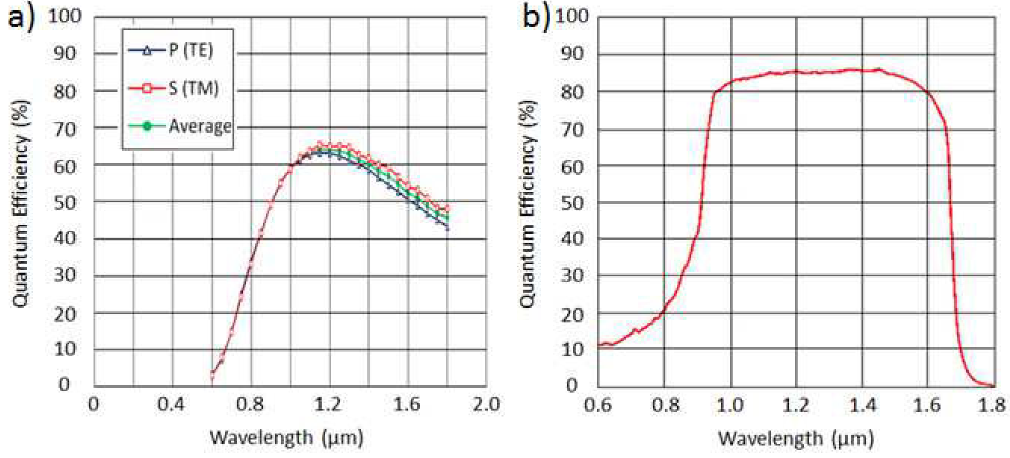


Figure A.2: (a): Quantum efficiency of the 100 lines/mm holographic diffraction grating, blazed at 1.2 $\mu$m. P and S stem from transverse-magnetic (TM) and transverse-electric (TE) polarizations [124]. (b): Quantum efficiency of the Andor iDus InGaAs 1.7 $\mu$m detector as a function of wavelength [125].

### A.1.1 Line A

An achromatic doublet (150 mm focal length) focuses the signal on the entrance slit of a spectrometer with a focal length of 300 mm. The spectrometer (JASCO, TRS-300) is equipped with a 100 lines/mm holographic diffraction grating (Shimadzu company), having a blaze at 1.2 $\mu$m. The spectral response of this grating is shown in Figure A.2 (a).

The dispersed light is measured by a thermoelectrically cooled InGaAs array multichannel detector (DU492A-1.7, produced by Andor Technology) consisting of 512 pixels and with a cut-off energy at 0.75 eV. The spectral response of the InGaAs array detector is shown in Figure A.2 (b). This detector, was used to perform direct-gap PRPL measurements of bulk Ge and of the (111)-oriented Ge/$Si_{1-x}Ge_x$ MQWs sample, reported in Chapters 1 and 4, respectively.

### A.1.2 Line B

A gold-coated parabolic mirror (100 mm focal length) focuses the signal on the entrance slit of a spectrometer with a focal length of 320 mm. The

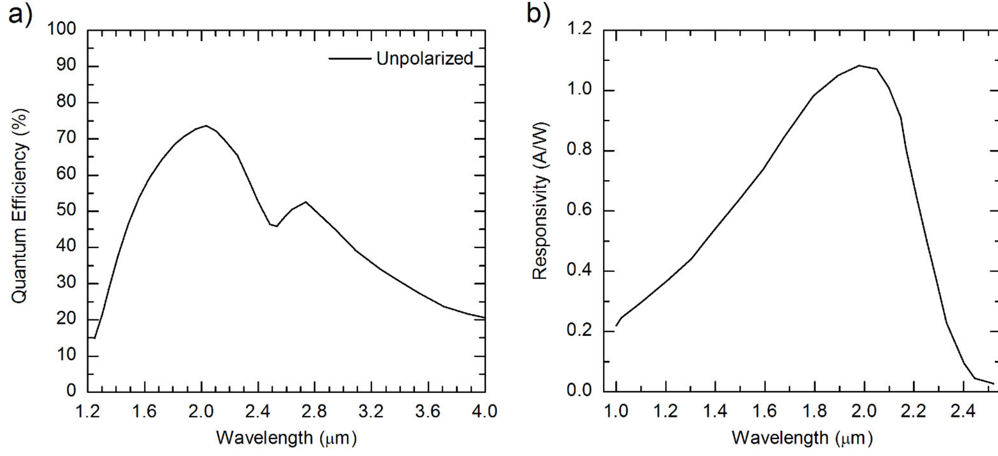


Figure A.3: (a): Quantum efficiency of the 150 lines/mm holographic diffraction grating. Blaze is at 2 $\mu$m. (b): Quantum efficiency of DSSIGA2.2 LN InGaAs 2.2 $\mu$m detector as a function of wavelength [126].

Table A.1: Characteristics of holographic diffraction gratings mounted on the turret of the HORIBA iHR 320 spectrometer.

| Groove Density (l/mm) | Blaze (nm) | Blaze Angle (deg) |
|---|---|---|
| 150 | 2000 | $8°38'$ |
| 600 | 1000 | $17°27'$ |
| 600 | 2000 | $36°52'$ |

monochromator (HORIBA iHR 320) is equipped with 3 holographic diffraction gratings, mounted on a turret (see Table A.1). In this work only that with a 150 lines/mm groove density, blaze at 2 $\mu$m, was used. Its spectral response is shown in Figure A.3(a).

The dispersed light is then measured by a liquid nitrogen cooled InGaAs single channel detector (DSSIGA2.2 LN, produced by HORIBA Jobin Yvon) with a cut-off energy at about 0.52 eV. Its spectral response is shown in Figure A.3. Finally, the output detector signal is filtered by means of a SR510 Stanford lock-in amplifier. This light-chopped technique allows us to increase the signal-to-noise ratio. This detector was used to reveal the indirect-gap emission of $Ge/Si_{1-x}Ge_x$ MQWs samples in Chapters 2 and 4.

## A.2 Time Resolved PL

### A.2.1 Bench A

A schematic drawing of the experimental set-up used to carry out polarization- and time-resolved PL with a resolution in the ps time scale is reported in Figure A.4. An APE optical parameter oscillator (OPO) pumped by a Tsunami 1 ps Ti:Sa laser, produced by Spectra Physics, was used as a tunable excitation source between about 1000 nm and 1400 nm. The temporal width and the repetition rate of the laser were 1.5-2 ps and 80 MHz, respectively. In this work the excitation wavelength was tuned from 1000 nm to 1280 nm. The exciting beam, filtered through a 1300 nm short-pass (SP) filter, is directed towards a linear polarizer and a $\lambda/4$ waveplate allowing the light incident on the sample to be circularly polarized. Time- and polarization-resolved PL was carried out in backscattering geometry. A quartz systems is used to compensate the polarization loss on the sample surface caused by the reflecting prism. The laser light is focused on the sample surface by means of two achromatic doublets in series, so that the total focal length is close to 21 mm. Under these conditions the focused spot diameter is calculated to be $\sim 7\ \mu$m.

The sample is mounted on the cold finger of a cryostat cooled by a closed helium refrigerator (CTI-Cryogenics).

The PL signal emitted from the sample is collimated by the achromatic doublet in front of the cryostat and sent to the analyser, consisting of a rotating $\lambda/4$ waveplate followed by a linear polarizer. The combination of LP, SP and BP filters is used to eliminate the scattered laser light and allows us to measure the indirect-gap emission of the sample under investigation.

An achromatic doublet (75 mm focal length) focuses the emitted PL signal on the entrance of an optic fiber, chosen to match the spectral window of the PL (for the list of utilized optic fibers see Table A.2).

The signal is then measured by a superconducting nanowire single-photon system (SNSPD), produced by Single Quantum [127], equipped with 4 detectors, cooled at 2.6 K using a helium compressor (HC4E Sumimoto cryo-

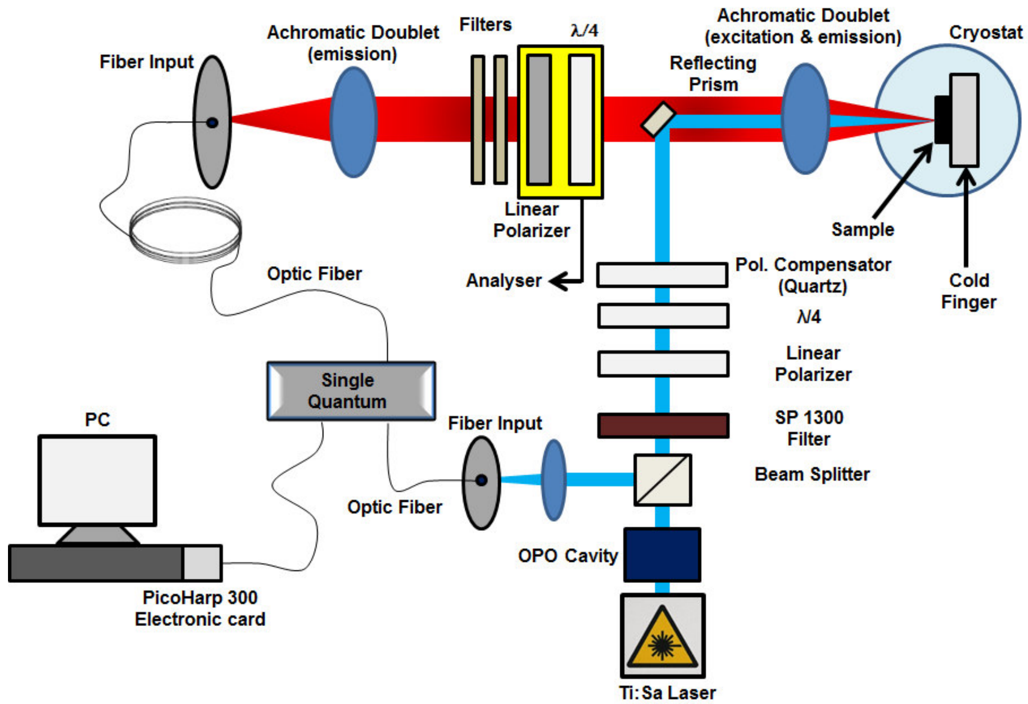


Figure A.4: Sketch of the experimental set-up used for polarization- and time-resolved PL measurements with nanosecond resolution.

Table A.2: Optic Fibers used to transmit the PL signal, produced by Thorlabs.

| Name | Operating wavelength (nm) | Mode Field Diameter ($\mu$m) |
|---|---|---|
| P3-2000-FC2 | 1700-2300 | 13 $\mu$m @ 1996 nm |
| SMF28E | 1260-1625 | 10.4 $\mu$m @ 1550 nm |

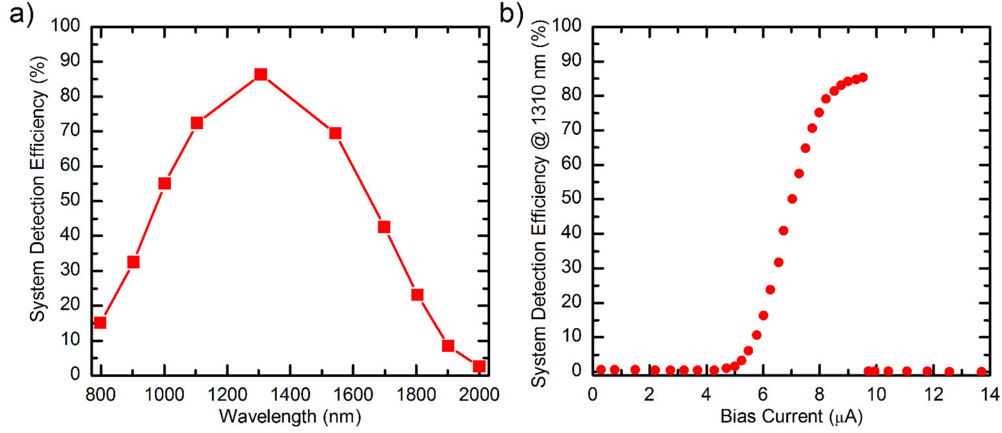


Figure A.5: (a): Superconducting nanowire single-photon detector spectral response. (b): Typical efficiency of the superconducting nanowire single-photon detector at 1310 nm as a function of the applied bias current. [127]

genics). The quantum efficiency of the detector is shown in Figure A.5(a). This kind of devices has rapidly emerged since it offers high efficiency, low dark counts and excellent time-resolution [128]. The typical dark count efficiency of these devices is shown in Figure A.5(b). A beam splitter set after the OPO cavity is used to send the signal of the laser to the PicoHarp 300 Electronic card. In this way the laser pulse is correlated with the PL signal. The time resolution was about 50 ps. The signal is then analysed by a $\sim$ 65000 channels PicoQuant electronic card (PicoHarp 300) driven by a PC. The experimental set-up described in this section was employed to carry out measurements reported in Chapters 2 and 3.

### A.2.2 Bench B

A schematic drawing of the experimental set-up used to carry out polarization- and time-resolved PL with a resolution in the ns time scale is reported in Figure A.6. The excitation source is a 1.165 eV (1064 nm) DTL-324QT Nd: YAG Q-switch pulsed laser with a repetition rate of 10 kHz, produced by Laser-export, with an average power density of 6.8 kW/cm$^2$ and a peak

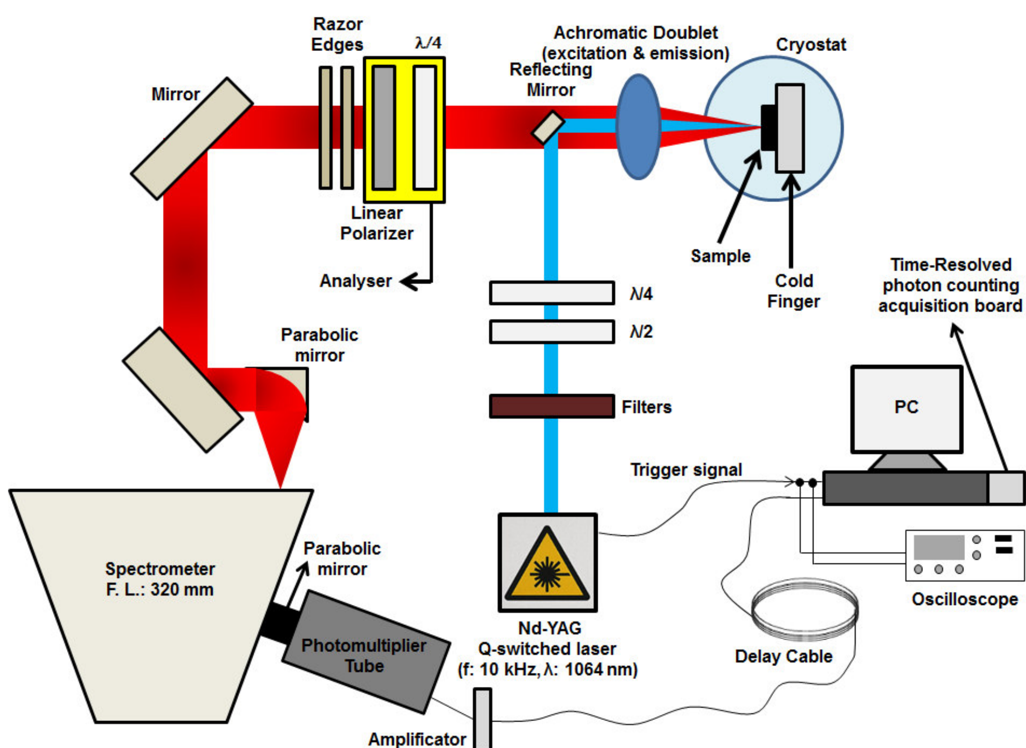


Figure A.6: Sketch of the experimental set-up used for the polarization- and time-resolved PL measurements with nanosecond time resolution.

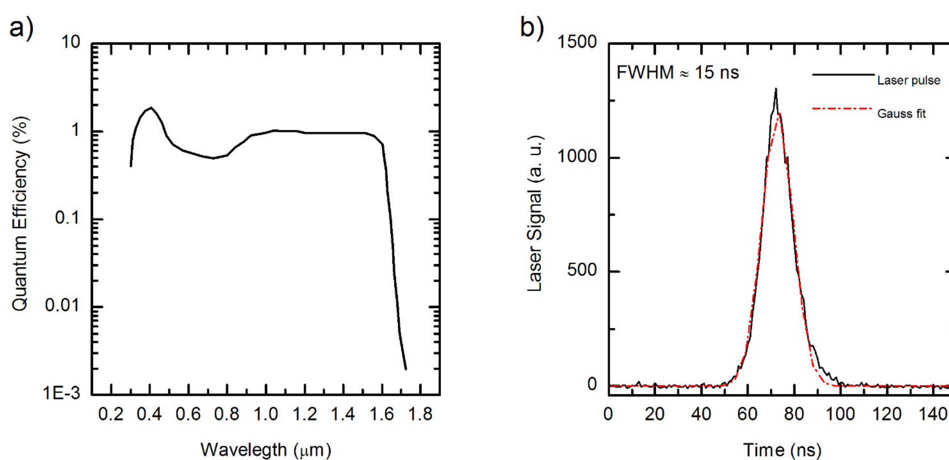


Figure A.7: (a): Photomultiplier spectral response [129]. (b): Laser pulse temporal width (black line) and Gaussian fit (red dashed line). The FWHM obtained from the fit is indicated.

power density[1] of $4.9 \cdot 10^4$ kW/cm$^2$. The temporal width of the laser is about 15 ns (Figure A.7). Excitation and emission lines are identical to those described in Appendix A.1 and A.1.2, respectively.

Emission is collected by a monochromator equipped with a 150 l/mm holographic grating (see Table A.1) whose position, in this case, is kept fix. This allows us to measure the decay curve at a selected emission energy. Two silver-coated parabolic mirrors (100 mm focal length) focus the PL signal on the photocathode of a liquid nitrogen cooled Hamamatsu R5509-73 photomultiplier tube (PMT) with a cut-off energy at about 0.77 eV, whose spectral response is shown in Figure A.7. The cut-off is defined by the material of the PMT window (borosilicate glass), and by the photocathode, consisting of InP/InGaAs. Finally the signal is recorded by a FAST ComTec P7888-1(E) multi-stop acquisition board, working in single photon counting mode. The signal is displayed by means of an oscilloscope, and a trigger coming from the laser provides the start acquisition. The experimental set-up described in this section was employed to carry out measurements reported in chapter 4.

[1]The peak power density was calculate using the following formula:

$$P_{Pulse} = P/A \cdot 1/F \cdot 1/\Delta t,$$

where P is the average laser power, A is the spot dimension of the laser beam focused on the surface of the sample, F is the laser repetition rate and Δt is the laser temporal width.

# Appendix B

# Stokes Analysis

In this chapter we will provide details about full-Stokes analysis, which was exploited to determine the polarization state of the direct-gap PL of bulk Ge (Chapter 1).

Polarization of the emitted luminescence analysis shown in Chapter 1 was evaluated by means of full Stokes analysis [13]. To introduce the Stokes parameters we consider a monochromatic optical beam propagating along the $z$ direction and having the following components at $z = 0$:

$$\begin{aligned} E_x(t) &= E_{0x} \cdot \cos(\omega t + \delta x) \\ E_y(t) &= E_{0y} \cdot \cos(\omega t + \delta y), \end{aligned} \tag{B.1}$$

where $t$ represents the time, $\omega$ the angular frequency, while $E_{0x}$ and $E_{0y}$ are the amplitudes. The Stokes polarization parameters $S_i$, with $i = 0, 1, 2, 3$, are measurable observables that completely characterize the polarization state of an optical field. If now we write the wave equations in the complex form, we get:

$$\begin{aligned} E_x(t) &= E_x \cdot \exp(i\omega t) \\ E_y(t) &= E_y \cdot \exp(i\omega t), \end{aligned} \tag{B.2}$$

where

$$E_x = E_{0x} \cdot \exp(i\delta x)$$
$$E_y = E_{0y} \cdot \exp(i\delta y), \tag{B.3}$$

are the complex amplitudes. It can be shown that Stokes parameters can be defined as [130]:

$$\begin{aligned} S_0 &= E_x E_x^* + E_y E_y^* \\ S_1 &= E_x E_x^* - E_y E_y^* \\ S_2 &= E_x E_y^* + E_y E_x^* \\ S_3 &= i(E_x E_y^* - E_y E_x^*), \end{aligned} \tag{B.4}$$

where the asterisk indicates the complex conjugate, $i = \sqrt{-1}$ and

$$S_0^2 = S_1^2 + S_2^2 + S_3^2 \tag{B.5}$$

which holds for completely polarized light. $S_0$ represents the total intensity of the optical field, while $S_1$, $S_2$ and $S_3$ determine the degree of linear (horizontal or vertical) polarization, linear (+45° or −45°) polarization and circular (right or left) polarization, respectively.

Stokes parameters can be also combined into a vector, called Stokes vector, defined as:

$$\vec{S} = \begin{pmatrix} S_0 \\ S_1 \\ S_2 \\ S_3 \end{pmatrix} = \begin{pmatrix} E_{0x}^2 + E_{0y}^2 \\ E_{0x}^2 - E_{0y}^2 \\ 2E_{0x}E_{0y}\cos\delta \\ 2E_{0x}E_{0y}\sin\delta \end{pmatrix} \tag{B.6}$$

Starting from Equation B.6 it is possible to obtain all states of light polarization and, in particular:

- Linear horizontal polarization:

$$\begin{aligned} S_0 &= S_1 = E_{0x}^2 \\ S_2 &= S_3 = 0 \end{aligned} \tag{B.7}$$

- Linear vertical polarization:

$$\begin{aligned} S_0 &= -S_1 = E_{0y}^2 \\ S_2 &= S_3 = 0 \end{aligned} \tag{B.8}$$

- Right circular polarization:

$$\begin{aligned} S_0 &= S_3 = 2E_{0x}^2 = 2E_{0y}^2 \\ S_1 &= S_2 = 0 \end{aligned} \tag{B.9}$$

- Left circular polarization:

$$\begin{aligned} S_0 &= -S_3 = 2E_{0x}^2 = 2E_{0y}^2 \\ S_1 &= S_2 = 0 \end{aligned} \tag{B.10}$$

Let us now consider the case of partially polarized light, which can be considered as a superposition of unpolarized and completely polarized light. In this case, the Stokes parameters satisfy the following relation [131]:

$$S_0^2 > S_1^2 + S_2^2 + S_3^2 \tag{B.11}$$

and the polarization degree ($\rho$) can be defined as:

$$\rho = \frac{I_{Polarized}}{I_{Total}} = \frac{\sqrt{S_1^2 + S_2^2 + S_3^2}}{S_0}, \tag{B.12}$$

where $0 \leq P \leq 1$, while $I_{Total}$ and $I_{Polarized}$ are the total intensity and the intensity of the polarized component, respectively. It is worth noticing that, when the polarization type is circular, Equation B.12 coincides with Equation 1.7, that we introduced in Section 1.3 to define the PL circular polarization

degree. The Stokes vector can be now written as:

$$\vec{S} = \begin{pmatrix} S_0 \\ S_1 \\ S_2 \\ S_3 \end{pmatrix} = (1-\rho)\begin{pmatrix} S_0 \\ 0 \\ 0 \\ 0 \end{pmatrix} + \rho \begin{pmatrix} S_0 \\ S_1 \\ S_2 \\ S_3 \end{pmatrix} \tag{B.13}$$

We can therefore consider the normalized Stokes vector:

$$\vec{S} = \begin{pmatrix} S_0' \\ S_1' \\ S_2' \\ S_3' \end{pmatrix} \equiv \begin{pmatrix} S_0 \\ S_1 \\ S_2 \\ S_3 \end{pmatrix} = \begin{pmatrix} 1 \\ S_1/\rho S_0 \\ S_2/\rho S_0 \\ S_3/\rho S_0 \end{pmatrix} \tag{B.14}$$

as a representation of the polarized component of light. The normalized Stokes vector defines a point on a surface of a sphere of unit radius: the Poincaré sphere, where (x, y, z)=($S_1$, $S_2$, $S_3$).

The Poincaré sphere (Figure B.1 (a)) is a convenient graphical method to visualize light polarization:

- Right-handed circular polarization ($|R\rangle$) is localized on the north pole of the sphere;
- Left-handed circular polarization ($|L\rangle$) is localized on the south pole of the sphere;
- Linear polarization state ($\frac{1}{\sqrt{2}}(|R \pm L\rangle)$) is localized on the equator sphere;
- Elliptically polarized states are represented everywhere else on the sphere surface.

In this thesis, the Stokes polarization parameters were measured by an optical retarder followed by a linear polarizer (Figure B.1 (b)). The retarder ($\lambda/4$ waveplate) rotates at an angular frequency $\omega$, whereas the polarizer is kept fixed (see Appendix A.1.1). The PL intensity is then probed by means of a multiple channel detector at each angle of the rotating optical element.

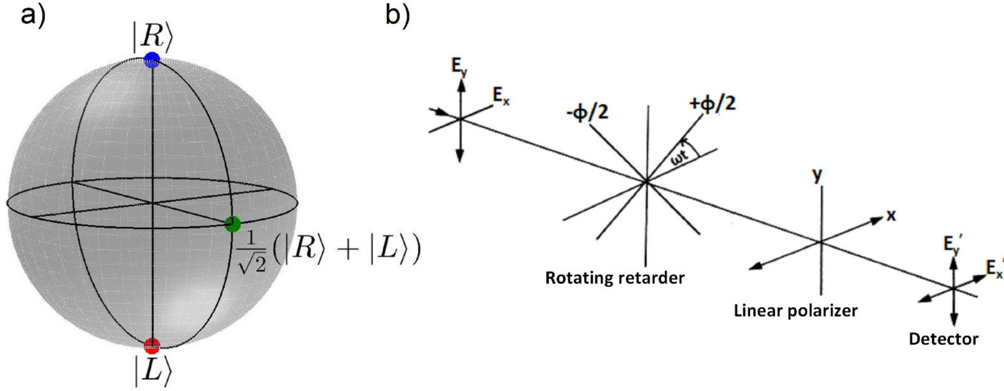


Figure B.1: (a): Poincaré sphere: blue(red) dot on the north(south) pole represents right(left)-handed circularly polarized light emission, while green dot on equator line represents linearly polarized light emission. (b): Stokes parameters measurements by means of a rotating retarder followed by a linear polarizer [131].

A Fourier analysis of the peak amplitude modulation (I($\omega$t)) allows us to obtain Stokes parameters via the determination of the Fourier coefficients [130, 131]. In particular, the Stokes parameters were found by a least square fit of I($\omega$t) with a function containing the sum of trigonometric functions. The function is defined by:

$$F_{Fit}(\theta) = \frac{1}{2}[A - B\sin(\pi\theta/90) + \cos(\pi\theta/45) + D\sin(\pi\theta/45)]. \tag{B.15}$$

The Stokes parameters are then calculated from the values of $\mathrm{F_{Fit}}$ as follows:

$$\begin{aligned} S_0 &= A - C \\ S_1 &= 2C \\ S_2 &= 2D \\ S_3 &= B \end{aligned} \tag{B.16}$$

Moreover, since in our case the emitted PL is always partially polarized, we employed the normalized Stokes parameters described above (Equation B.14) to plot our data through the polarized component of the Poincaré sphere.

The modulation intensity as a function of the quarter waveplate retarder

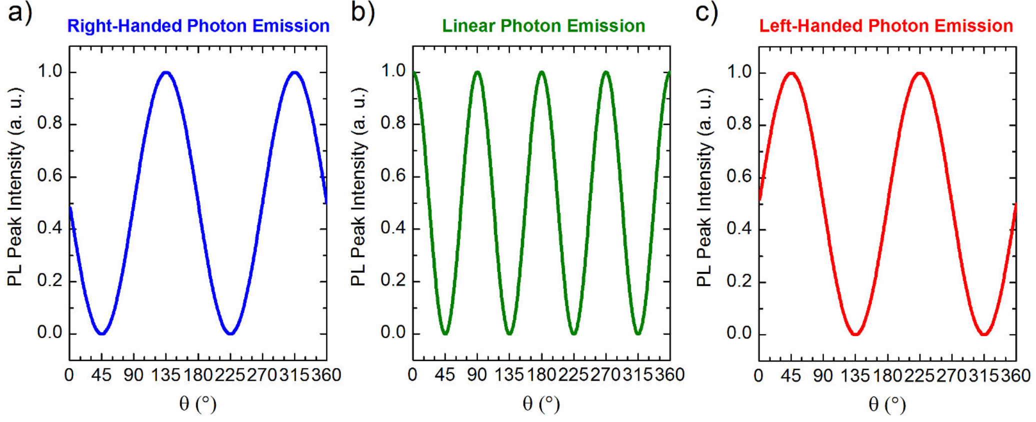


Figure B.2: PL peak intensity modulation as a function of the $\lambda/4$ retarder angle ($\theta$). A phase profile of $3\pi/4$ stems from right-handed ($\sigma^+$) circularly polarized light (a) and (c), while a phase profile of $\pi/4$ indicates that helicity of emitted photons is linear (b).

angle thus allows us to determine the polarization type of the PL. In particular, the polarization type is defined by the $\theta$ position of the maximum intensity ($I_{Max}$) of the PL peak: a sinusoidal behaviour is the feature of circular polarization (Figure B.2). The phase of the sinusoidal profile ($\pi/4$ or $3\pi/4$) is directly related to the circularly polarized light helicity: we have that for $I_{Max}$ at $\theta = 135°$, $315°$, the emitted photons helicity is right-handed circularly polarized (Figure B.2 (a)), while for $I_{Max}$ at $\theta = 45°$, $225°$, the emission is left-handed circularly polarized (Figure B.2 (c)). On the other hand, $I_{Max}$ at $\theta = 0°$, $90°$, $180°$, $270°$, corresponds to linearly polarized light emission (Figure B.2 (b)). It is worth noticing that, in the case of $\sigma^-$ laser excitation, $I_{Max}$ at $\theta = 45°$, $225°$ means co-polarized emission, while for $I_{Max}$ at $\theta = 135°$, $315°$ the photon helicity is counter-polarized.

# Appendix C

# Spin Lifetime Dependence on Temperature

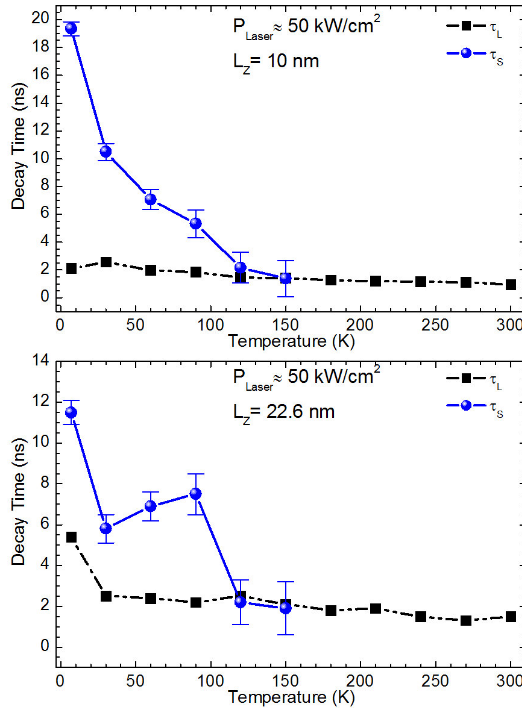


Figure C.1: Upper panel: 7864-6 sample ($L_Z$=10 nm), lower panel: 7909-11 sample ($L_Z$=22.6 nm). $L_Z$ is the well thickness. Blue dots: temperature dependence of the spin relaxation time ($\tau_S$). Black squares: temperature dependence of the electron lifetime ($\tau_L$).

# Bibliography

[1] S. A. Wolf, D. D. Awschalom, R. A. Buhrman, J. M. Daughton, S. von Molnár, M. L. Roukes, A. Y. Chtchelkanova, and D. M. Treger. Spintronics: A spin-based electronics vision for the future. *Science*, 294:1488, 2001.

[2] R. Soref. The past, present and future of silicon photonics. *IEEE J. Sel. Top. Quant.*, 12:1678, 2006.

[3] M. Oestreich, J. Hubner, D. Hagele, M. Bender, N. Gerhardt, M. Hofmann, W. W. Ruhle, T Kalt, H. Hartmann, P. Klar, W. Heimbrodt, and W. Stolz. Spintronics: Spin electronics and optoelectronics in semiconductors. *Advances in Solid State Physics*, 41:17, 2001.

[4] R. Jansen. Silicon spintronics. *Nat. Mater.*, 11:400, 2012.

[5] J. J. L. Morton, D. R. McCamey, M. A. Eriksson, and S. A. Lyon. Embracing the quantum limit in silicon computing. *Nature*, 479:345, 2011.

[6] S. Dushenko, M. Koike, Y. Ando, T. Shinjo, M. Myronov, and M. Shiraishi. Experimental demonstration of room-temperature spin transport in n-type germanium epilayers. *Phys. Rev. Lett.*, 114:196602, 2015.

[7] Y. P. Zutić, J. Fabian, and S. Das Sarma. Spintronics: Fundamentals ans applications. *Rev. Mod. Phys.*, 76:323, 2004.

[8] E. Yablonovitch, H. W. Jiang, H. Kosaka, H. D. Robinson, D. S. Rao, and T. Szkopek. Optoelectronic quantum telecommunication based on spins in semiconductors. *Proceedings of. the IEEE*, 91:761, 2003.

[9] D. Liang and J. E. Bowers. Recent progress in lasers on silicon. *Nature Photon.*, 4:511, 2010.

[10] G. Lampel. Nuclear dynamic polarization by optical electronic saturation and optical pumping in semiconductors. *Phys. Rev. Lett.*, 20:491, 1968.

[11] E. J. Loren, B. A. Ruzicka, L. K. Werake, H. Zhao, H. M. van Driel, and A. L. Smirl. Optical injection and detection of ballistic pure spin currents in ge. *Appl. Phys. Lett.*, 95:092107, 2009.

[12] C. Guite and V. Venkataraman. Measurement of electron spin lifetime and optical orientation efficiency in germanium using electrical detection of radio frequency modulated spin polarization. *Phys. Rev. Lett.*, 107:166603, 2011.

[13] F. Pezzoli, F. Bottegoni, D. Trivedi, F. Ciccacci, A. Giorgion, P. Li, S. Cecchi, E. Grilli, Y. Song, M. Guzzi, H. Dery, and G. Isella. Optical spin injection and spin lifetime in ge heterostructures. *Phys. Rev. Lett.*, 108:156603, 2012.

[14] Y. Zhou, L.-T. Chang, F. Xiu, M. Wang, M. Oehme, I. A. Fischer, J. Schulze, R. K. Kawakami, and K. L. Wang. Electrical spin injection and transport in germanium. *Phys. Rev. B*, 84:125323, 2011.

[15] C. D. Stanciu, F. Hansteen, A. V. Kimel, A. Kirilyuk, A. Tsukamoto, A. Itoh, and T. Rasing. All-optical magnetic recording with circularly polarized light. *Phys. Rev. Lett.*, 99:047601, 2007.

[16] K. Nishizawa, N.and Nishibayashi and H. Munekata. All-optical magnetic recording with circularly polarized light. *Appl. Phys. Lett.*, 104:111102, 2014.

[17] Y.J. Zhang, T. Oka, J. T. Ye, and Y. Iwasa. Electrically switchable chiral light-emitting transistor. *Science*, 344:725, 2014.

[18] Y.-H. Kuo, Y. K. Lee, Y. Ge, F. Ren, J. E. Roth, T. I. Kamins, D. A. B. Miller, and J. S. Harris. Strong quantum confined stark effect in germanium quantum-well structures on silicon. *Nature*, 54:1334, 2005.

[19] M. Bonfanti, E. Grilli, M. Guzzi, M. Virgilio, G. Grosso, D. Chrastina, G. Isella, H. von känel, and A. Neels. Optical transitions in ge/sige multiple quantum wells with ge-rich barriers. *Phys. Rev. B*, 78:041407(R), 2008.

[20] C. Lange, N. S. Köster, S. Chatterjee, H. Sigg, D. Chratina, H. Isella, G. von Känel, M. Schäfer, M. Kira, and S. W. Koch. Ultrafast nonlinear optical response of photoexcited ge/sige quantum wells: Evidence for a femtosecond transient population inversion. *Phys. Rev. B*, 79:201306(R), 2009.

[21] J.-M. Tang, B. T. Collins, and M. E. Flatté. Electron spin-phonon interaction symmetries and tunable spin relaxation in silicon and germanium. *Phys. Rev. B*, 85:045202, 2012.

[22] P. Li, Y. Song, and H. Dery. Intrinsic spin lifetime of conduction electrons in germanium. *Phis. Rev. B*, 86:085202, 2012.

[23] M. Oestreich, S. Hallstein, and W. W. Rühle. Spin quantum beats in semiconductors. *IEEE J. of Sel. Topics in Quantum Electronics*, 2:747, 1996.

[24] M. Hannack, R. M. Oestreich, A. P. Heberle, and W. W. Rühle. Electron g factor in quantum wells determined by spin quantum beats. *Sol. State Comm.*, 93:313, 1995.

[25] P. Le Jeune, D. Robart, X. Marie, T. Amand, M. Brousseau, J. Barrau, V. Kalevich, and D. Rodichev. Anisotropy of the electron land é g factor in quantum wells. *Semicon. Sci. Technol.*, 12:380, 1997.

[26] A. P. Heberle, W. W. Rühle, and K. Ploog. Quantum beats of electron larmor precession in gaas quantum wells. *Phys. Rev. Lett.*, 72:3887, 1994.

[27] A. Giorgioni, S. Paleari, S. Cecchi, E. Vitiello, E. Grilli, G. Isella, W. Jantsch, M. Fanciulli, and F. Pezzoli. Strong confinement-induced engineering of the g factor and lifetime of conduction electron spins in ge quantum wells. *Nat. Comm.*, 7:13886, 2016.

[28] F. A. Baron, A. A. Kiselev, H. D. Robinson, K. W. Kim, K. L. Wang, and E. Yablonovitch. Manipulating the l-valley electron g factor in si-ge heterostructures. *Phys. Rev. B*, 68:195306, 2003.

[29] J. Liu, X. Sun, R. Camacho-Aguilera, L. C. Kimerling, and J. Michel. Ge-on-si laser operating at room temperature. *Opt. Lett.*, 35:679, 2010.

[30] N. W. Ashcroft and N. D. Mermin. *Solid state physics.* Harcourt College Publishers, 1976.

[31] C. Kittel. *Introduction to solid state physics, 7th edition.* John Wiley and sons, 1996.

[32] L. Pavesi and M. Guzzi. Photoluminescence of $Al_xGa_{1-x}As$ alloys. *J. Appl. Phys.*, 75:4779, 1994.

[33] J. I. Pankove. *Optical processes in semiconductors.* Nick Holonyak, Jr., 1971.

[34] G. Mak and H. M. van Driel. Femtosecond transmission spectroscopy at the direct band edge of germanium. *Phys. Rev. B*, 49:16817(R), 1994.

[35] X. Q. Zhou, H. M. van Driel, and G. Mak. Femtosecond kinetics of photoexcited carriers in germanium. *Phys. Rev. B*, 50:5226, 1994.

[36] K. Kolata, N. S. Köster, A. Chernikov, M. J. Drexler, E. Gatti, S. Cecchi, D. Chrastina, G. Isella, M. Guzzi, and S. Chatterjee. Dephasing in ge/sige quantum wells measured by means of coherent oscillations. *Phys. Rev. B*, 86:201303(R), 2012.

[37] Y. Yu and M. Cardona. *Fundamentals of Semiconductors: Physics and Materials Poperties.* Springer-Verlag, 2010.

[38] F. Pezzoli, L. Qing, A. Giorgioni, G. Isella, E. Grilli, M. Guzzi, and H. Dery. Spin and energy relaxation in germanium studied by spin-polarized direct-gap photoluminescence. *Phys. Rev. B*, 88:045204, 2013.

[39] A. Giorgioni, E. Vitiello, E. Grilli, M. Guzzi, and F. Pezzoli. Valley-dependent spin polarization and long-lived electron spins in germanium. *Appl. Phys. Lett.*, 105:152404, 2014.

[40] R. R. Lieten, K. Bustillo, T. Smets, E. Simoen, G. W. Ager III, E. E. Haller, and J.-P. Locquet. Photoluminescence of bulk germanium. *Phys. Rev. B*, 86:035204, 2012.

[41] Y. Yin, D. Yan, and H. Pollak. Temperature dependence of the fundamental direct transitions of bulk ge and two ge/sige multiple-quantum-well structures. *Phys. Rev. B*, 52:8951, 1995.

[42] Y. P. Varshni. Temperature dependence of the energy gap in semiconductors. *Physica*, 34:149, 1967.

[43] E. Hecht. *Optics*. Addison-Wesley, 2002.

[44] R. R. Parson. Band-to-band optical pumping in solids and polarized photoluminescence. *Phys. Rev. Lett.*, 23:1152, 1969.

[45] M. Oestreich, M. Bender, J. Hübner, D. Hägele, W. W. Rühle, T. Hartmann, P. J. Klar, W. Heimbrodt, M. Lampalzer, K. Volz, and W. Stolz. Spin injection, spin transport and spin coherence. *Semicond. Sci. Technol.*, 17:285, 2002.

[46] M. Fox. *Optical properties of solids*. Oxford University Press, 2010.

[47] E. J. Loren, J. Rioux, C. Lange, J. E. Sipe, H. M. van Driel, and L. Smirl. Hole spin relaxation and intervalley electron scattering in germanium. *Phis. Rev. B*, 84:214307, 2011.

[48] M. I. D'yakonov and V. I. Perel. *Optical Orientation, Modern Problems in Condensated Matter Science, Vol. 8.* F. Meier and B. P. Zakharchenya, 1984.

[49] J. Fabian and Das Sarma S. Spin relaxation of conduction electrons. *J. of Vacuum Science and Technology B*, 17:1708, 1999.

[50] J. Fabian, A. Matos-Abiague, C. Ertler, P. Stano, and I. Zutic. Semiconductor spintronics. *Acta Physica Slovaca*, 57:565, 2007.

[51] Y. P. Zutić, J. Fabian, and S. Das Sarma. Spin injection through the depletion layer: A theory of spin polarized p-n junctions and solar cells. *Phys. Rev. B*, 64:121201, 2001.

[52] M. I. D'yakonov and V. I. Perel. Feasibility of optical orientation of equilibrium electrons in semiconductors. *JETP Lett.*, 13:144, 1971.

[53] J. Rioux and J. E. Sipe. Optical injection and control in germanium: Thirty-band $k \cdot p$ theory. *Phis. Rev. B*, 81:155215, 2010.

[54] F. Pezzoli, A. Giorgioni, G. Isella, S. De Cesari, E. Grilli, and M. Guzzi. Spin-resolved study of direct band-gap recombination in bulk ge. *Proc. of SPIE*, 9167:91670H–1, 2014.

[55] C. Haas. Infrared absorption in heavily doped n-type germanium. *Phis. Rev.*, 125:1965, 1962.

[56] J. Wagner and L. Viña. Radiative recombination in heavily doped p-type germanium. *Phis. Rev. B*, 30:7030, 1984.

[57] S. C. Jain and D. J. Roulston. A simple expression for band gap narrowing (bgn) in heavily doped si, ge, gaas and $Ge_xSi_{1-x}$ strained layers. *Sol. State. Electronics*, 34:453, 1991.

[58] W. J. Elder, R. M. Ward, and J. Zhang. Double-group formation of $k \cdot p$ theory for cubic crystals. *Phis. Rev. B*, 83:165210, 2011.

[59] E. Vitiello, M. Virgilio, A. Giorgioni, J. Frigerio, E. Gatti, S. De Cesari, E. Bonera, E. Grilli, G. Isella, and F. Pezzoli. Spin-dependent direct gap emission in tensile-strained ge films on si substrates. *Phis. Rev. B*, 92:201203(R), 2015.

[60] W. Klingestein and H. Schweizer. Direct-gap recombination in germanium at high excitation level and low temperature. *Sol. State. Electronics*, 21:1371, 1978.

[61] A. R. Denton and N. W. Ashcroft. Vegard's law. *Phys. Rev.A*, 43:3161, 1991.

[62] J. Weber and M. I. Alonso. Near-band-gap photoluminescence of sige alloys. *Phys. Rev. B*, 40:5683, 1989.

[63] E. P. O'Reilly. Valence band engineering in strained-layer structures. *Semicond. Sci. Technol.*, 4:121, 1989.

[64] J. Liu, X. Sun, D. Pan, X. Wang, L. C. Kimerling, T. L. Koch, and J. Michel. Tensile-strained, n-type ge as a gain medium for monolithic laser integration on si. *Optics Express*, 15:11272, 2007.

[65] J. E. Matthews and A. E. Blakeslee. Defects in epitaxial multilayers. *J. Christal Growth*, 27:118, 1974.

[66] J. H. van der Merwe. Structure of epitaxial crystal interfaces. *Surf. Science*, 31:198, 1972.

[67] E. P. Kvam. Rapid variation in epilayer threading dislocation density near $x = 0.4$ in $Ge_xSi_{1-x}$ on (100) si. *Phil. Mag. Lett.*, 62:167, 1990.

[68] L. D. Landau and E. M. Lifshits. *Theory of elasticity, Vol. 7.* Oxford University Press, 3rd edition, 1986.

[69] J. Hirth and J. Lothe. *Theory of dislocations,.* Mc Graw-Hill, New York, 1982.

[70] F. Shäffler. High-mobility si and ge structures. *Semicond. Sci. Technol.*, 12:1515, 1997.

[71] K. F. LeGoues, B. S. Meyerson, and J. F. Morar. Anomalous strain relaxation in sige thin films and superlattices. *Phys. Rev. Lett.*, 66:2903, 1991.

[72] E. A. Fitzgerald, Y.-H. Xie, M. L. Green, D. Brasen, A. R. Kortan, J. Michel, Y.-J. Mii, and B. E. Weir. Totally relaxaed relaxation $Ge_xSi_{1-x}$ layers with low threading dislocation densities grown on si substrates. *Appl. Phys.Lett.*, 59:811, 1991.

[73] J. Christen, D. Bimberg, A. Steckenborn, and G. Weimann. Localization induced electron-hole transition rate enhancement in gaas quantunm wells. *Appl. Phys.Lett.*, 44:84, 1984.

[74] C. Rosenblad, H. R. Deller, A. Dommann, T. Meyer, P. Schroeter, and H. von Känel. Silicon epitaxy by low-energy plasma enhanced chemical vapor deposition. *J. Vac. Sci. Technol.*, 16:2785, 1998.

[75] H. Rosenblad, C.and von känel, M. Kummer, A. Dommann, and E. Müller. A plasma process for ultrafast deposition of sige graded buffer layers. *Appl. Phys. Lett.*, 76:427, 1999.

[76] G. Isella, D. Chrastina, B. Rössner, T. Hackbarth, H.-J. Herzog, U. König, and H. von känel. Low-energy plasma-enhanced chemical vapor deposition for strained si and ge heterostructures and devices. *Sol. State Electronics*, 48:1317, 2004.

[77] Y.-H. Kuo, Y. Ge, S. Ren, E. Roth, T. I. Kamins, D. A. B. Miller, and J. S. Harris. Quantum-confined stark effect in ge/sige quantum wells on si for optical modulators. *IEEE Journal of Selected Topics in Quantum Electronics*, 12:1503, 2006.

[78] V. Härle, H. Bolay, E. Lux, P. Michler, A. Moritz, T. Forner, A. Hangleiter, and F. Scholz. Indirect-band-gap transition in strained gainas/inp quantum-well structures. *J. Appl. Phys.*, 75:5067, 1994.

[79] S. Fukatsu, H. Akiyama, Y. Shiraki, and K. Sakaki. Quantitative analysis of light emission from sige quantum wells. *J. Christ. Growth*, 157:1, 1995.

[80] A. Giorgioni, E. Gatti, E. Grilli, A. Chernikov, D. Chatterjee, D. Chrastina, G. Isella, and M. Guzzi. Photoluminescence decay of

direct and indirect transitions in ge/sige multiple quantum wells. *J. Appl. Phys.*, 111:013501, 2012.

[81] D. J. Olego, T. Marshall, D. Cammack, H. Schahzad, and J. Petruzzello. Electronic raman scatteirng from acceptors and correlation with transport properties in li-doped znse layers. *Appl. Phys. Lett.*, 58:2654, 1998.

[82] F. Pezzoli, A. Balocchi, E. Vitiello, T. Amand, and X. Marie. Optical orientation of electron-spins and valence-band spectroscopy in germanium. *Phys. Rev.B*, 91:201201(R), 2015.

[83] J. Wagner and M. Cardona. Electronic raman scattering in heavily doped p-type germanium. *Phys. Rev.B*, 32:8071, 1985.

[84] K. Tanaka, H. Ohtake, and T. Suemoto. Resonant inter-valence-band raman scattering of photoexcited holes in germanium. *Phys. Rev.B*, 50:10694, 1994.

[85] A. Giorgioni, F. Pezzoli, E. Gatti, S. Cecchi, C. lnoki, C. K. Deneke, E. Grilli, G. Isella, and M. Guzzi. Optical tailoring of carrier spin polarization in ge/sige multiple quantum wells. *Appl. Phys. Lett.*, 102:012408, 2013.

[86] F. Pezzoli, A. Giorgioni, K. Gallacher, F. Isa, P. Biagioni, R. W. Millar, E. Gatti, E. Grilli, E. Bondera, G. Isella, D. J. Paul, and L. Miglio. Disentangling nonradiative recombination processes in ge micro-crystals on si substrates. *Appl. Phys. Lett.*, 108:262103, 2016.

[87] G. Mauckner, K. Thonke, T. Baier, T. Walter, and R. Sauer. Temperature-dependent lifetime distribution of the photoluminescence s-bandin porous silicon. *J. Appl. Phys.*, 75:4167, 1994.

[88] S. Lebib, H. J. von Bardeleben, J. Cernegora, J. L. Fave, and J. Roussel. Time-resolved photoluminescence study of the red emission in nanoporous sige alloys. *J. of Luminescence*, 80:153, 1999.

[89] L. Pavesi and M. Ceschini. Stretched-exponential decay of the luminescence in porous silicon. *Phys. Rev. B*, 48:17625, 1993.

[90] M. Grydlik, F. Hackl, H. Groiss, M. Glaser, A. Halilovic, T. Fromherz, W. Jantsch, F. Shäffler, and M. Brehm. Lasing from glassy ge quantum dots in crystalline si. *ACS Photonics*, 3:298, 2016.

[91] J. Feldmann, G. Peter, P. Göbel, E. O. Dawson, K. Moore, C. Foxon, and R. J. Elliot. Linewidth dependence of radiative exciton lifetimes in quantum wells. *Phys. Rev. Lett.*, 59:2337, 1987.

[92] J. Tignon, O. Heller, P. Roussignol, Bastard G., C. Piermarrochi, R. Planel, and V. Thierry-Mieg. Carrier dynamics in shallow gaas/algaas quantum wells. *Phys. Rev. Lett.*, 2:126, 1998.

[93] Y. Takahashi, S. Owa, S. S. Kano, K. Muraki, Y. Fukatsu, Y. Shiraki, and R. Ito. Two-dimensional exciton dynamics in ingaas /gaas quantum wells. *Appl. Phys. Lett.*, 60:213, 1992.

[94] T. Amand, X. Marie, B. Dareys, Barrau J., M. Brousseau, D. J. Dunstan, J. Y. Emery, and L. Goldstein. Well-width dependence of the excitonic lifetime in strianed iii-v quantum wells. *J. Appl. Phys.*, 72:2077, 1992.

[95] M. Grundmann and D. Bimberg. Anisotropy effects on excitonic properties in realistic quantum wells. *Phys. Rev. B*, 38:13486(R), 1988.

[96] M. Engel, R. K. Bauer, D. Bimberg, D. Gruetzmacher, and H. Juergensen. Interface roughness and charge carrier recombination lifetimes in gainas/inp quantum wells grown by lp-movpe. *J. Christ. Growth*, 93:359, 1988.

[97] Y. Yafet. *Solid State Physics, Vol. 14*. F. Seitz and B. Turnbull, 1963.

[98] R. J. Elliot. Theory of the effect of spin-orbit coupling on magnetic resonance in some semiconductors. *Phys. Rev.*, 96:266, 1954.

[99] A. Polimeni, A. Patané, M. Grassi Alessi, M. Capizzi, F. Martelli, A. Bosacchi, and S. Franchi. Stokes shift in quantum wells: Trapping versus thermalization. *Phys. Rev. B*, 54:16389, 1996.

[100] J. Lohrenz, T. Paschen, and M. Betz. Resonant spin amplification in intrinsic bulk germanium: Evidence for electron spin lifetimes exceeding 50 ns. *Phys. Rev. B*, 89:121201(R), 2014.

[101] C. Hu, H. Ye, G. Wang, H. Tian, W. Wang, W. Wang, B. Liu, and X. Marie. Room temperature spin diffusion in (110) gaas/algaas quantum wells. *Nanoscale Res. Lett.*, 6:149, 2011.

[102] Y. Ohno, R. Terauchi, T. Adachi, F. Matsukura, and H. Ohno. Spin relaxation in gaas(110) quantum wells. *Phys. Rev. Lett.*, 20:4196, 1999.

[103] G. W. Ludwig and H. H. Woodbury. *Electron spin resonance in semiconductors.* Volume 13 of Solid State Physics, Academic Press, 1962.

[104] L. M. Roth. g factor and donor spin-lattice relaxation for electrons in germanium and silicon. *Phys. Rev.*, 118:1534, 1959.

[105] G. Feher, D. K. Wilson, and E. A. Gere. Electron spin resonance experiments on shallow donors in germanium. *Phys. Rev. Lett.*, 3:25, 1959.

[106] C. Hautmann, B. Surrer, and M. Betz. Ultrafast optical orientation and coherent larmor precession of electron and hole spins in bulk germanium. *Phys. Rev. B*, 83:161203(R), 2011.

[107] H. S. Lan, S.-T. Chan, T.-H. Cheng, C.-Y. Chen, S.-R. Jan, and C. W. Liu. Biaxial tensile strain effects on photoluminescence of different orientated ge wafers. *Appl. Phys. Lett.*, 98:101106, 2011.

[108] Y.-J. Yang, W. S. Ho, C.-F. Huang, S. T. Chang, and C. W. Liu. Electron mobility enhancement in strained-germanium n-channel metal-oxide-semiconductor field-effect transistors. *Appl. Phys. Lett.*, 91:102103, 2007.

[109] A. Zhylik, A. Benediktovich, A. Ulyanenkov, H. Guerault, M. Myronov, A. Dobbie, D. R. Leadley, and T. Ulyanenkova. High-resolution x-ray diffraction investigation of relaxation and dislocations in sige layers grown on (001), (011), (111) si substrates. *J. Appl. Phys.*, 109:123714, 2011.

[110] J. Parson, E. H. C. Parker, D. R. Leadley, T. J. Grasby, and A. D. Capewell. Misfit strain relaxation and dislocation formation in supercritical strained silicon on virtual substrates. *Appl. Phys. Lett.*, 91:063127, 2007.

[111] J. W. Harper, P. G. Hobdy and R. A. Stradling. Electrons and optic phonons in solids - the effects of longitudinal optical lattice vibrations on the electronic excitation of solids. *Rep. Prog. Phys.*, 36:1, 1973.

[112] L. L. Lee, D. A. Antoniadis, and E. A. Fitzgerald. Challenges in epitaxial growth of sige buffers on si (111), (110) and (112). *Thin Solid Films*, 508:136, 2006.

[113] V. Destefanis, J. M. Hartmann, A. Abbadie, A. M. Papon, and T. Billon. Growth and structural properties of sige virtual substrates on si (100), (110) and (111). *J. Christ. Growth*, 311:1070, 2009.

[114] V. Huy Nguyen, A. Dobbie, M. Myronov, D. J. Norris, T. Walther, and D. R. Leadley. Epitaxial growth of relaxed germanium layers by reduced pressure chemical vapour deposition on (110) and (111) silicon substrates. *Thin Solid Films*, 520:3222, 2012.

[115] E. Gatti, F. Isa, D. Chrastina, E. Müller Gubler, F. Pezzoli, E. Grilli, and G. Isella. Ge/sige quantum wells on si(111): Growth, structural, and optical properties. *J. Appl. Phys.*, 116:043518, 2014.

[116] D. J. Paul. 8 band $k \cdot p$ modeling of the quantum confined stark effect in ge quantum wells on si substrates. *Phys. Rev. B*, 77:155323, 2008.

[117] http://www.nextnano.de.

[118] E. Gatti, E. Grilli, M. Guzzi, D. Chrastina, G. Isella, and H. von känel. Room temperature photoluminescence of ge multiple quantum wells with ge-rich barriers. *Appl. Phys. Lett.*, 98:031106, 2011.

[119] M. Virgilio and G. Grosso. Optical spin orientation in strained ge/sige quantum wells: A tight-binding approach. *Phys. Rev. B*, 80:205309, 2009.

[120] T. Uenoyama and L. J. Sham. Hole relaxation and luminescence polarization in doped and undoped quantum wells. *Phys. Rev. Lett.*, 64:3070, 1990.

[121] P. Li and H. Dery. Theory of spin-dependent phonon-assisted optical transitions in silicon. *Phys. Rev. Lett.*, 105:037204, 2010.

[122] M. Z. Maialle, E. A. de Andrada e Silva, and L. J. Sham. Exciton spin dynamics in quantum wells. *Phys. Rev. B.*, 47:15776, 1993.

[123] R. R. Parsons. Band-to-band optical pumping in solids and polarized photoluminescence. *Phys. Rev. Lett.*, 23:1152, 1969.

[124] http://www.shimadzu.com.

[125] http://www.andor.com.

[126] http://www.horiba.com.

[127] http://www.singlequantum.com.

[128] C. M. Natarajan, M. G. Tanner, and R. H. Hadfield. Superconducting nanowire-photon detectors: physics and applications. *Supercond. Sci. Technol.*, 25:063001, 2012.

[129] http://www.hamamatsu.com.

[130] E. Collett. *Field Guide to Polarization.* SPIE Press, 2005.

[131] D. H. Goldstein. *Polarized Light, third edition.* Taylor and Francis, 2010.

# Acknowledgements

I am very grateful to all the people who shared with me these years and that helped me in writing this work.

In particular, I want to spend a special mention for Fabio Pezzoli, who took care of me step by step. From the very beginning he helped and encouraged me with patience, competence and friendship, trying to convey me his passion for science. I want also to thank Prof. Emanuele Grilli, who provided me an invaluable help both in experimental and physics problems and who has been a great example of hard-working and professionalism.

I am also grateful to Anna Giorgioni and Elisa Vitiello, friends more than colleagues, who shared with me joyful and distress times of this adventure. Thank also to the other people of the research group: Prof. Mario Guzzi, Emiliano Bonera, Michael Barget, Francesco Basso Basset and Eleonora Gatti. Each of them, in his own way, has been important for me.

I thank the dean of the PhD course in Science and Nanotechnology of Materials, Prof. Gian Paolo Brivio, and Mrs. Maria Cristina Fassina whose help in paperwork was very precious.

I want to aknowledge all the people of the Optoélectronique Quantique group at the INSA of Toulouse (France), who hosted me for five months during my PhD and, among them, a special thank is for Dr. Andrea Balocchi who supervised and helped me everyday.

I am sincerely grateful to the research group at L-NESS laboratories in Como. The sample growth was carried out by Prof. Giovanni Isella and Dr. Fabio Isa, while Dr. Daniel Chrastina performed the XRD characterization.

Least but not last, let me spend a special thank for all my family and, in particular, for my parents. They supported and helped me since I was a

child and they have always believed in me: Each of my goals is also their merit.

Finally, this work is dedicated to Nicomedia who encouraged me all times I needed it. Romanticism has never been my strong point, but I think she deserves it for everything she did and she does for me every day.

Thank you.